Master's thesis

NTNU
Norwegian University of Science and Technology
Faculty of Natural Sciences
Department of Physics

Håvard Falch

# Paramagnetic Meissner Effect and Non-Equilibrium Vortices in Superconductor/Normal-Metal Structures

Master's thesis in Applied Physics and Mathematics
Supervisor: Jabir Ali Ouassou and Jacob Linder
June 2023

NTNU
Norwegian University of
Science and Technology

Håvard Falch

# Paramagnetic Meissner Effect and Non-Equilibrium Vortices in Superconductor/Normal-Metal Structures

Master's thesis in Applied Physics and Mathematics
Supervisor: Jabir Ali Ouassou and Jacob Linder
June 2023

Norwegian University of Science and Technology
Faculty of Natural Sciences
Department of Physics

NTNU
Norwegian University of
Science and Technology

**Abstract**

The proximity effect between a superconductor and a normal metal leads to some of the superconductivity leaking into the normal metal. In the presence of a magnetic field or applied currents, this means that superconducting vortices can arise in the normal metal region. We consider superconductor-normal metal structures and specifically how the superconducting vortices in the normal-metal region are altered by driving the system out of equilibrium by injecting quasiparticles, controlled by an external voltage. Using the quasiclassical formalism we derive the Usadel equation and solve it for three different geometries, either analytically or numerically. For all three geometries, we find that the screening currents in the vortices in the normal metal can be reversed, which is a sign of a voltage-induced paramagnetic Meissner effect. In addition, we can control this paramagnetic Meissner effect by varying the external voltage. This suggests a way in which the electromagnetic response of the proximitzed normal metal can be tuned by driving it out of equilibrium.

**Sammendrag**

Proksimitetseffekten mellom en superleder og et normalt metall fører til at noe av superledningen lekker inn i normalmetallet. Dette betyr at superledende virvler kan oppstå i normalmetallområdet. Vi studerer superleder-normalmetallstrukturer og spesifikt hvordan de superledende virvlene i normalmetallområdet påvirkes av å drive systemet ut av likevekt ved å injisere kvasipartikler, kontrollert av en ekstern spenning. Ved å bruke den kvasiklassiske formalismen utleder vi Usadel-ligningen og løser den for tre forskjellige geometrier, enten analytisk eller numerisk. For alle tre geometriene finner vi at skjermingsstrømmene i virvlene i normalmetallet kan reverseres, som et tegn på en spenningsindusert paramagnetisk Meissner-effekt. I tillegg kan vi kontrollere denne paramagnetiske Meissner-effekten ved å variere den eksterne spenningen. Dermed ser vi at den elektromagnetiske responsen til det proksimerte normalmetallet kan bli kontrollert ved å drive det ut av likevekt.

# Preface

This master's thesis was written during the spring of 2023 under the supervision of doctor Jabir Ali Ouassou and professor Jacob Linder, amounting to 30 ECTS credits, and concludes five years of study of Applied Physics and Mathematics at NTNU. It builds upon the work done in the specialization project carried out in the autumn semester of 2022 which amounted to 15 ECTS credits. Thus, quite a bit of the project is included for completeness. Chapter 1 is adapted from the specialization project with parts of Sec. 1.1 and the entirety of Sec. 1.2 taken directly from it. Chapter 2, which contains the results from the specialization project, is taken from it unchanged. Chapter 3 contains the main work done this semester.

I would like to thank Jabir Ali Ouassou for lending me so much of his time and valuable expertise, and for guiding me through various problems encountered during the semester. I would also like to thank Jacob Linder for providing his excellent insight and thoughtful guidance throughout the semester. In addition, I must thank my fellow master students at QuSpin who have created a great environment for working and for useful discussions throughout the semester. Finally, I would like to thank my family for always supporting me.

Håvard Falch
Trondheim, Norway
June 2023

# Contents

# Chapter 1

# Motivation and background

## 1.1 Introduction

### 1.1.1 Superconductivity

Superconductivity is a phenomenon exhibited by many materials when the temperature is reduced below a critical temperature $T_c$, and is characterized by two distinct features. The first is the absence of any electrical resistivity and the second, known as the Meissner effect, is the expulsion of magnetic fields from the superconductor. The first discovery of superconductivity was made by H. K. Onnes in 1911 who cooled down pure mercury to 4.2 K [1]. He then measured a sudden drop from a finite resistance to one that could not be measured. The next big discovery for superconductivity was made in 1933 by W. Meissner and R. Ochsenfeld when they discovered that magnetic flux was totally expelled from superconductors [2]. However, at this point, there was still no satisfactory theoretical description of superconductivity. The first steps towards a full theoretical description were made by F. and H. London in 1935, when they discovered the London equation and thus described the relationship between magnetic fields, supercurrents and the Meissner effect [3]. A full phenomenological description was given by V. L. Ginzburg and L. D. Landau in 1950 using a wavefunction $\Psi$ to describe superconductivity as a second-order phase transition [4]. Also in 1950, E. Maxwell [5] and C. A. Reynolds et al. [6] discovered independently that $T_c$ is lower for heavier isotopes of the same element, which is known as the isotope effect. The relation between superconductors and magnetic fields was expanded upon in 1957 when A. A. Abrikosov released his findings about how type-II superconductors enter the mixed state for an intermediate critical field $H_{c1}$ containing vortices with non-superconducting cores [7].

In addition to the isotope effect, it had been known that metals that were good conductors at high temperatures had a lower critical temperature than metals that were inferior conductors. The fact that this resistivity is attributed to electron-phonon scattering, in addition to the isotope effect, pointed towards phonons, i.e., lattice vibrations, being a crucial ingredient for superconductivity. Finally, a microscopic description was given by J. Bardeen, L. N. Cooper and J. R. Schrieffer in 1957. They described the superconducting state as a charged superfluid condensate of bosonic electron pairs, known as Cooper pairs, with opposite spin which feel an effective attraction due to interactions mediated by phonons [8]. This was the condensate described by Ginzburg and Landau with

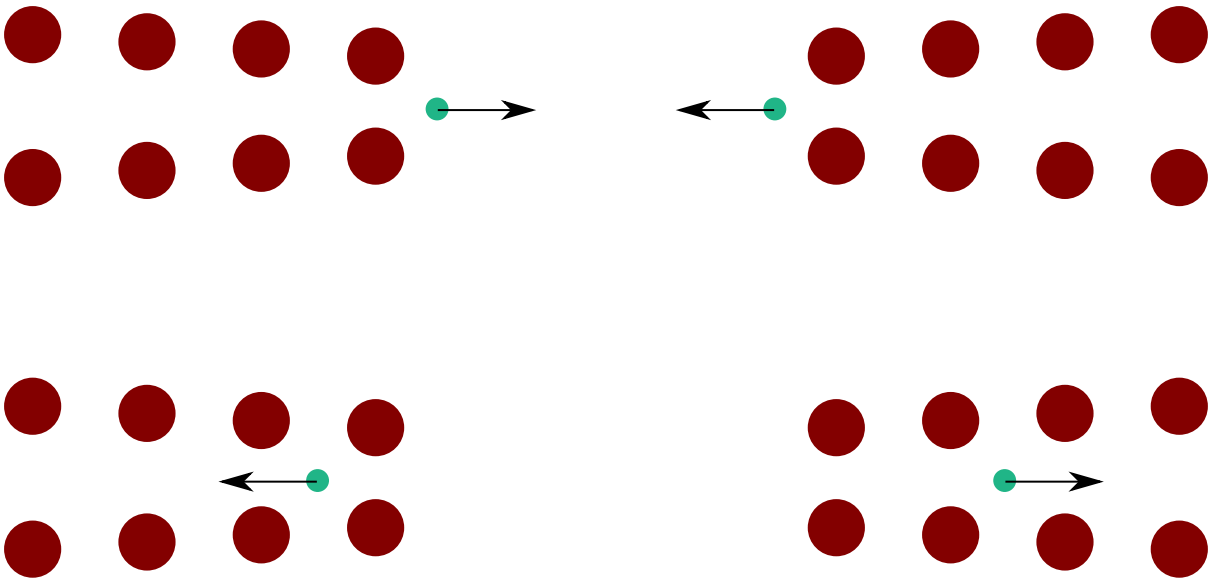

Figure 1.1: Cartoon drawing of BCS superconductivity. Two electrons, in green, move through a lattice of ions, in red. They each create a distortion in the lattice as the ions are attracted to the electrons. This allows the other electron to move through the distortion and as the region has a net positive charge, the electrons lower their energy, leading to a bound state, protecting them from scattering.

the wavefunction $\Psi$. While the BCS theory gave a good description of all superconductors known in the 1950s, it does not give a good description of high-temperature superconductors which were first discovered by J. G. Bednorz and K. A. Müller in 1986 [9]. The description of the non-superconducting state out of which high-temperature superconductivity emerges remains an important open research problem in condensed matter physics.

While a full understanding of BCS superconductivity requires treating the many-body quantum mechanical problem, one can still get an intuitive understanding of what is happening. A cartoon figure of the mechanism is shown in Fig. 1.1. Metals consist of lattices of positively charged ions through which electrons move. As the electrons are significantly lighter than the ions, they move much faster. Thus when an electron moves through the lattice, the attraction between the electron and the ions leads to a small distortion in the lattice. As the ions are heavy, they use a relatively long time to relax back to their equilibrium positions. Before they have time to relax, another electron can pass through the distortion caused by the first electron. Because of the attraction between the ions and the electron, this leads to the electron having a lower energy when moving in the distortion caused by the first electron. This means that there is an energy barrier that needs to be surpassed to scatter the electron out of the distortion. The same also happens for the first electron moving through the distortions caused by the second electron. Thus the electrons enter a bound state, lowering their energy, and one needs a finite energy to destroy this bound state and scatter the electrons. While this energy might be small, it is significant at low temperatures. At higher temperatures, the thermal energy and vibrations are too large and we get no such bound state. This explains why BCS superconductivity is observed only at low temperatures.

### 1.1.2 Magnetic fields and superconductivity

One of the most interesting effects arising when placing a superconductor in a magnetic field is the creation of vortices. Vortices typically arise for the so-called type-II superconductors when the field is larger than the lower critical field $H_{c1}$. This was first described by A. A. Abrikosov in 1957 [7]. He found that when the field is at least of size $H_{c1}$, it is energetically favourable to start forming vortices where a quantized amount of magnetic field penetrates through the superconductor in each vortex. Supercurrents circulate around these vortices, screening the rest of the material from the magnetic field. The vortices distribute themselves as far away from each other as possible which usually results in a triangular lattice, but according to Abrikosov, this would change to a square lattice when the field is increased closer to the critical field $H_{c2}$, i.e. the field at which superconductivity vanishes completely. In 1964 W. H. Kleiner et al. [10] found a solution to the Ginzburg-Landau equations where they showed that the triangular lattice also has a lower free energy than the square lattice close to $H_{c2}$. Thus they showed that the triangular lattice can be stable for all fields between $H_{c1}$ and $H_{c2}$. The first experimental evidence was given by D. Cribier et al. [11], who used neutron diffraction in niobium to show superconducting vortices that were distributed in a periodic triangular pattern. This was later shown to also be the case in vanadium by W. Fite and A. G. Redfield [12].

The properties of vortices in superconductors is still a vibrant field of research. In 2000, L.F. Chiboutaru et al. [13] showed that vortices respect the discrete symmetries of the sample. They found that for a square sample, four vortices appear at a time, and moreover that antivortices and giant vortices are generated to conserve the four-fold symmetry. If one introduces impurities to the sample, one can break the discrete symmetries. I.V. Grigorieva et al. [14] showed experimentally that defects in a material can lead to the vortex pattern not respecting the discrete symmetries. The impurities could instead lead to pinning of vortices, and lead to several vortices merging and forming giant vortices.

As a superconducting vortex with quantized flux is a phenomenon related to superconductivity, one would not expect such effects in a normal metal. However, when a normal metal is placed in contact with a superconductor, some of the superconductivity leaks from the superconductor to the normal metal. This effect is known as the proximity effect and induces superconducting properties in the normal metal. The first discovery of proximity effects was by R. Holm and W. Meissner [15] in 1932 when they found that a thin normal metal with superconductors on both sides had zero electrical resistance when a current was passed through. The microscopic description of how proximity effects appear was given by A. F. Andreev [16] in 1964 when he described a process now known as Andreev reflections. In this process, an electron moving in the normal metal towards the superconductor-normal metal interface can tunnel through the barrier and a hole with opposite spin will be reflected in the normal metal. This leads to an effective charge transfer of $2e$, i.e. a Cooper pair is generated or annihilated, and causes anomalous correlations between the electrons and holes in the normal metal, giving rise to the proximity-induced superconductivity.

In addition, proximity-induced superconductivity implies that the normal metal will acquire some of the properties of the superconductor. For instance, the normal metal can screen a magnetic field penetrating it. This screening was studied by A. D. Zaikin in 1982 [17]. He studied theoretically superconductor-normal metal proximity sandwiches.

In the clean limit, he found that the current density does not depend on the location within the normal metal and that the relation between the current density **j** and the magnetic vector potential **A** is non-local. This can lead to a sign flip of the magnetic field penetrating the normal metal, with an extra screening such that the field at the superconductor-normal metal interface is half the strength of the applied field and in the opposite direction. In the dirty limit, he found that the relation is local and thus he found no such flipping, and that screening of the magnetic field happens only close to the superconductor interface. W. Belzig et al. [18] studied a similar screening but instead of a planar geometry, they used a cylindrical one. Specifically, they considered a superconducting cylinder surrounded by a normal metal and found that in this geometry, the magnetic field could oscillate inside the normal metal part. When compared to the planar limit, they found that the cylindrical geometry increased the magnetic susceptibility. In the limit of a thick normal metal, the magnetic field at the superconductor-normal metal interface was equal in size and oppositely directed compared to the external magnetic field in the cylindrical geometry, as opposed to half that value for the planar geometry as shown by Zaikin.

Applying a magnetic field to a normal metal with proximity-induced superconductivity can also have other interesting effects. W. Belzig et al. [19] studied normal metals in proximity to a superconductor. Using full nonlinear magnetic response, they showed that the magnetization can have hysteric behaviour both in the clean and dirty limit, matching the experimental results from A. C. Mota et al. [20] and T. Bergmann et al. [21]. F. S. Bergeret and J. C. Cuevas [22] investigated the critical current in a diffusive SNS junction. They showed that as the width of the normal metal increases while in a perpendicular magnetic field, the magnetic field dependence of the critical current changes from a monotonic decay when the width is smaller than the magnetic length, to the Fraunhofer pattern in wide junctions. This behaviour was due to the formation of a linear array of vortices in the normal region as the junction became wider.

The induced vortices in a normal metal are interesting to study on their own because of the properties they have. D. Roditchev et al. [23] studied vortices in Josephson junctions, so-called Josephson vortices. By direct observations of the Jospheson vortices using scanning tunnelling microscopy, they found that the Josephson vortices have a real core, where the superconductivity is suppressed and the normal state is recovered. Direct observations of individual vortices can be done in several ways including scanning tunnelling electron microscopy [24], where one measures the density of states by placing a conducting tip close to the sample and measuring the current, as well as magneto-optical imaging [25], where one makes use of the fact that a magnetic field rotates photons. In addition to observing the vortex cores, D. Roditchev et al. [23] described a way to create vortices without the use of magnetic fields. Instead, having two superconductors along a material with currents going the opposite way leads to vortices very similar to the magnetic ones. This type of non-magnetic vortex was further studied by M. Amundsen et al. [26] when they investigated the vortex formation in a normal metal square surrounded by a superconductor with a current flowing. Depending on the applied current, normal vortices, giant vortices and antivortices could form to respect the discrete symmetries of the square.

The Meissner effect is one of the most important effects in superconducting materials. For example, this allows superconductors to levitate above magnets and can be used for

magnetically levitating trains [27]. Recently, the paramagnetic Meissner effect, where materials attract magnetic flux instead of expelling, it has been of considerable interest. Studies of a paramagnetic superconducting state lead all the way back to 1973 when A. G. Aronov [28] showed that by irradiating a superconductor one can force it out of equilibrium. Driven far enough from equilibrium this would lead to a paramagnetic state. However, this was shown to be an unstable state by A. G. Aronov and B. Z. Spivak [29]. More recently, the focus has been on heterostructures where non-superconducting materials acquire induced superconducting properties due to the proximity effect from a superconductor. The main focus has been on triplet components of the superconducting state that are odd in frequency. Such states were first predicted in superfluids by V. L. Berezinskii in 1974 [30], and are formed in many superconducting systems, such as hybrid structures and multiband superconductors [31]. In 2001 F. S. Bergeret et al. [32] found that for a superconductor-ferromagnet bilayer with a homogeneous exchange field, one can get either a paramagnetic or diamagnetic screening currents caused by the internal magnetic field, depending on the product of the exchange field and the momentum relaxation time. However, they did not consider the effects of an external field. J. Linder et al. [33, 34] showed that one could get purely odd-frequency triplet components in a normal metal with a spin-active interface connecting it to a superconductor for an interface resistance above a critical value dependent on the interface spin polarization. Building on this, T. Yokoyama et al. [35] showed that in a normal metal-superconductor junction with a spin-active interface, one can get an anomalous Meissner effect which leads to spatial and temperature-dependent oscillations of the magnetic field in the normal metal, including a sign change. They showed that this is due to the generation of odd-frequency pairing at the interface. Another way to control the paramagnetic response is to use two ferromagnetic layers between the superconductor and normal metal. M. Alidoust et al. [36] found that due to the odd-frequency triplet superconducting components, this setup leads to a paramagnetic Meissner effect, and depending on the angle between the magnetizations in the two ferromagnets, one can tune the size of the paramagnetic response. The first experimental evidence of a paramagnetic Meissner effect came in 2015 when A. Di Bernardo et al. [37] measured experimentally the magnetic field in Au in a Au/Ho/Nb trilayer, where the antiferromagnetic Ho layer, which breaks time-reversal symmetry, can generate odd-frequency components from the conventional even frequency superconductivity in Nb. They showed that this leads to a paramagnetic Meissner effect in Au, experimentally verifying the effect arising from odd-frequency superconductivity. While most of the research has been focused on the net Meissner effect of a material, A. A. Golubov [38] studied the effect in superconducting vortices. They found that when applying an external magnetic field, the proximity-induced screening currents around a vortex in the ferromagnet can change sign depending on the suppression at the interface between a superconductor and a ferromagnet. However, one does not need magnetic effects generating odd-frequency triplet components to get a paramagnetic Meissner effect. J. A. Ouassou et al. [39] showed analytically that for a normal metal placed on top of a thin film, one can generate a paramagnetic Meissner response by injecting quasiparticles controlled by an external voltage. These quasiparticles change the distribution function in the material. As one can create peaks in the density of states larger than the density of states at the Fermi level at subgap energies in proximitized normal metals, one can tune the Meissner response to be either paramagnetic or diamagnetic depending on the voltage.

This thesis will focus on the paramagnetic Meissner effect in superconducting vortices in a normal metal with induced superconductivity from the proximity effect. However, differing from most other studies of the paramagnetic Meissner effect, we will not have any magnetic components in the system. Instead, we drive the system out of equilibrium to look for a paramagnetic Meissner response. Using the same method of driving the system out of equilibrium by injecting quasiparticles as J. A. Ouassou et al. [39], we study how the screening of the magnetic field in superconducting vortices is affected by injecting these quasiparticles. However, whereas J. A. Ouassou et al. considered the clean limit using the Eilenberger equation and derived an analytical expression in an ideal case, we will consider the dirty limit and thus use the Usadel equation and study geometries where we solve the Usadel equation either analytically or numerically.

### 1.1.3 Structure of the master's thesis

This thesis is divided into four chapters and builds upon work done in the project thesis [40] written in the fall semester. Chapter 1 gives the motivation and theory for what we are going to study. This chapter is based on the project thesis, where the introduction is an expanded version, Sec. 1.2 is taken directly from it, while the remaining sections are shortened versions of what was written in the project thesis. Sec. 1.2 discusses some general concepts which are useful for this thesis. Then in Sec. 1.3 we derive the Hamiltonian for a quite general superconducting system, and in Sec. 1.4 we derive the equations of motion for the Green's function in this system, culminating in the Usadel equation. To finish up the chapter, we consider the limit of weak proximity effect to simplify the Usadel equation and derive an expression for the supercurrent in Sec. 1.5. In Chapter 2, which contains the results of the project thesis and is taken directly from it, we consider a cylindrical geometry to study the paramagnetic Meissner effect in a highly symmetric system. This allows us in Sec 2.1 to solve the linearized Usadel equation analytically both without an applied magnetic field and for one case with an applied magnetic field. Then we use these expressions in Sec. 2.2 to find the screening currents in the presence of a magnetic field and consider the effect of taking the system out of equilibrium. Chapter 3 presents the main new work done in this master thesis. Here we solve the Usadel equation numerically for two different square geometries and look for a reversal of the vortices indicating a paramagnetic Meissner effect. Before we can begin with the numerical solution, we describe some general numerical techniques we use in Sec 3.1. Then in Sec. 3.2 we discuss a system with a square normal metal surrounded by a superconductor on four sides and explain some useful theory for this system. This is then used to solve the Usadel equation for the system both with and without a magnetic field in Sec. 3.3. In Sec. 3.4 we consider a system of a thin film of normal metal placed on top of a type-II superconductor with an applied magnetic field, leading to induced vortices in the normal metal and discuss some useful theory for this system. In Sec. 3.5 we solve the Usadel equation in the thin film of normal metal, both for an isolated vortex and for 7 vortices laid out in a hexagonal arrangement. Finally, in Chapter 4 we conclude the thesis with a summary and outlook.

## 1.2 Preamble

### 1.2.1 Mathematical conventions

The notation and mathematical conventions will usually follow what is standard in physics. We will use natural units such that Planck's reduced constant $\hbar$, the speed of light $c$, the vacuum permittivity $\epsilon_0$, the vacuum permeability $\mu_0$ and Boltzmann's constant $k_b$ are all set to 1. Scalars will be written in italics $a$. The complex conjugate of a variable $a = b+ic$ will be written as $a^* = b-ic$, the transpose of a matrix as $\mathbf{A}^T$ and the Hermitian conjugate as $\mathbf{A}^\dagger$. Vectors and $2 \times 2$ matrices will, in general, be written in bold font $\mathbf{A}$ and it is clear from context and earlier definitions which it is. A $4 \times 4$ matrix will be written in bold with a hat $\hat{\mathbf{A}}$ while an $8 \times 8$ matrix will be written in bold with a check $\check{\mathbf{A}}$. Generally, $\mathbf{r}$ will denote a spatial variable, $\mathbf{p}$ a momentum, $t$ a time, $\epsilon$ an energy and $\sigma$ a spin unless otherwise specified. Partial derivatives will be written in compact notation as $\partial_x f(x,t) = \partial f(x,t)/\partial x$. Integrals will run over the entire system unless otherwise specified. We write the commutator as

$$[\mathbf{A}, \mathbf{B}]_- = \mathbf{AB} - \mathbf{BA}, \tag{1.2.1}$$

while the anticommutator is written as

$$[\mathbf{A}, \mathbf{B}]_+ = \mathbf{AB} + \mathbf{BA}. \tag{1.2.2}$$

When working with spins we use the Pauli matrices which are defined as:

$$\sigma^0 = \begin{bmatrix} 1 & 0 \\ 0 & 1 \end{bmatrix}, \quad \sigma^1 = \begin{bmatrix} 0 & 1 \\ 1 & 0 \end{bmatrix}, \quad \sigma^2 = \begin{bmatrix} 0 & -i \\ i & 0 \end{bmatrix}, \quad \sigma^3 = \begin{bmatrix} 1 & 0 \\ 0 & -1 \end{bmatrix}. \tag{1.2.3}$$

The Pauli matrices can be collected in a vector called the Pauli vector:

$$\boldsymbol{\sigma} = \sigma^1 \mathbf{e}_x + \sigma^2 \mathbf{e}_y + \sigma^3 \mathbf{e}_z. \tag{1.2.4}$$

Note that while the Pauli matrices $\sigma^i$ are $2 \times 2$ matrices they will not be written in bold to make a clear distinction from the Pauli vector $\boldsymbol{\sigma}$. When we work with electrons and holes and include their spins we need matrices that describe both the electrons and holes, Nambu space, and that describe the spins, spin space. The matrices in Nambu space will be labelled $\tau$ instead of $\sigma$, but are otherwise the same as the spin matrices $\sigma$. This leads us to Nambu-spin space and tensor products of the Pauli matrices which are $4 \times 4$ matrices:

$$\hat{\boldsymbol{\rho}}_1 = \tau^1 \otimes \sigma^1 \quad \hat{\boldsymbol{\rho}}_2 = \tau^1 \otimes \sigma^2 \quad \hat{\boldsymbol{\rho}}_3 = \tau^3 \otimes \sigma^0. \tag{1.2.5}$$

We will also be adding and multiplying matrices of different dimensions. This will be resolved by promoting the smaller matrix $\mathbf{A}$ to the corresponding dimension of the larger matrix by a tensor product with the identity $\mathbb{1} \otimes \mathbf{A}$, where the identity will not be explicitly written out. For a scalar $P$ multiplied with a $2 \times 2$ matrix $\mathbf{Q}$ living in spin space and added to a $4 \times 4$ matrix $\hat{\mathbf{R}}$ this will look like:

$$P\mathbf{Q}+\hat{\mathbf{R}} = \begin{bmatrix} P & 0 & 0 & 0 \\ 0 & P & 0 & 0 \\ 0 & 0 & P & 0 \\ 0 & 0 & 0 & P \end{bmatrix} \begin{bmatrix} Q_{1,1} & Q_{1,2} & 0 & 0 \\ Q_{2,1} & Q_{2,2} & 0 & 0 \\ 0 & 0 & Q_{1,1} & Q_{1,2} \\ 0 & 0 & Q_{2,1} & Q_{2,2} \end{bmatrix} + \begin{bmatrix} R_{1,1} & R_{1,2} & R_{1,3} & R_{1,4} \\ R_{2,1} & R_{2,2} & R_{2,3} & R_{2,4} \\ R_{3,1} & R_{3,2} & R_{3,3} & R_{3,4} \\ R_{4,1} & R_{4,2} & R_{4,3} & R_{4,4} \end{bmatrix}. \tag{1.2.6}$$

### 1.2.2 Quantum mechanics

In quantum mechanics a state is represented by a vector $|\varphi\rangle$, called a ket, in Hilbert space and this has a unique corresponding vector living in the dual Hilbert space $\langle\varphi|$, called a bra, the Hermitian conjugate of $|\varphi\rangle$. A physical observable $A$ is represented as a Hermitian operator acting on $|\varphi\rangle$. If the system is in state $|\varphi\rangle$ at time $t$ and we measure the observable $A$ at time $t'$ the expectation value is $\langle A\rangle = \langle\varphi|e^{iH(t'-t)}Ae^{-iH(t'-t)}|\varphi\rangle$ where $e^{-iHt}$ is the time evolution operator and $H$ is the Hamiltonian.

The states can be represented in position space as the wave function $\varphi(\mathbf{r},t) = \langle\mathbf{r}|\varphi\rangle$. The particularly simple part of working in position space is that for an operator represented as $\mathbf{A}$ in classical mechanics, the transformation $\mathbf{p} \to -i\nabla$ generates the corresponding operator in the position space representation of quantum mechanics.

To describe many-particle systems it is convenient to work in the number representation of quantum mechanics, also known as second quantization. Here there exists a vacuum state $|0\rangle$ and one can add and subtract particles from states by applying creation and annihilation operators, $c^\dagger_{\mathbf{p},\sigma}$ and $c_{\mathbf{p},\sigma}$. For example the operator $c^\dagger_{\mathbf{p},\sigma}$ creates an electron with momentum $\mathbf{p}$ and spin $\sigma$. The state

$$|\mathbf{p}\sigma\rangle = c^\dagger_{\mathbf{p},\sigma}|0\rangle\,, \tag{1.2.7}$$

is the one-particle state containing an electron characterized by momentum $\mathbf{p}$ and spin $\sigma$. The operator $c_{\mathbf{p},\sigma}$ is the annihilation operator which removes an electron characterized by momentum $\mathbf{p}$ and spin $\sigma$. When acting with $c_{\mathbf{p},\sigma}$ on the state defined in (1.2.7) we get back the vacuum state,

$$c_{\mathbf{p},\sigma}|\mathbf{p}\sigma\rangle = |0\rangle\,. \tag{1.2.8}$$

The vacuum state is defined such that acting on it with any annihilation operator will give 0,

$$c_{\mathbf{p},\sigma}|0\rangle = 0. \tag{1.2.9}$$

We can also define the number operator

$$n_{\mathbf{p},\sigma} = c^\dagger_{\mathbf{p},\sigma}c_{\mathbf{p},\sigma}, \tag{1.2.10}$$

which counts the number of particles in a state with momentum $\mathbf{p}$ and spin $\sigma$. As electrons are fermions they obey the Pauli principle and this is incorporated in this description by $(c^\dagger_{\mathbf{p},\sigma})^2 = 0$, i.e., two particles cannot be in the same state. This also means that $(c_{\mathbf{p},\sigma})^2 = 0$ by Hermitian conjugation.

A many-particle state is built up from superpositions of states on the form

$$(c^\dagger_{\nu_1})^{n_1}(c^\dagger_{\nu_2})^{n_2}\ldots|0\rangle\,, \tag{1.2.11}$$

where $\nu_i$ is the quantum numbers for a particle with momentum $\mathbf{p}$ and spin $\sigma$ and $n_i$ is the occupation number of the state labeled by $\nu_i$. Another consequence of electrons being fermions is that states are antisymmetric under particle exchange. For a state occupied by two particles characterized by $\mathbf{p},\sigma$ and $\mathbf{p}',\sigma'$ we have

$$c^\dagger_{\mathbf{p},\sigma}c^\dagger_{\mathbf{p}',\sigma'}|0\rangle = |\mathbf{p}\sigma,\mathbf{p}',\sigma'\rangle = -|\mathbf{p}'\sigma',\mathbf{p},\sigma\rangle = -c^\dagger_{\mathbf{p}',\sigma'}c^\dagger_{\mathbf{p},\sigma}|0\rangle\,. \tag{1.2.12}$$

The above relations could also have been derived from demanding that the creation and annihilation operators satisfy certain anticommutation relations. For quantum numbers $\nu_1$ and $\nu_2$ the anticommutation relations are

$$[c_{\nu_1}, c^\dagger_{\nu_2}]_+ = \delta_{\nu_1,\nu_2}, \quad [c_{\nu_1}, c_{\nu_2}]_+ = [c^\dagger_{\nu_1}, c^\dagger_{\nu_2}]_+ = 0. \tag{1.2.13}$$

Instead of the momentum-spin eigenvector basis, we can use the position-spin eigenvector basis. This transformation gives the creation and annihilation operators $\psi^\dagger_\sigma(\mathbf{r}, t)$ and $\psi_\sigma(\mathbf{r}, t)$, which create and annihilate an electron with spin $\sigma$ at position $\mathbf{r}$ and time $t$ and are traditionally called field operators. At an equal time $t$, the field operators satisfy the same anticommutation relations as the spin-momentum operators,

$$\begin{aligned} [\psi_\sigma(\mathbf{r}, t), \psi^\dagger_{\sigma'}(\mathbf{r}', t)]_+ &= \delta_{\sigma\sigma'}\delta(\mathbf{r} - \mathbf{r}') \\ [\psi_\sigma(\mathbf{r}, t), \psi_{\sigma'}(\mathbf{r}', t)]_+ &= [\psi^\dagger_\sigma(\mathbf{r}, t), \psi^\dagger_{\sigma'}(\mathbf{r}', t)]_+ = 0. \end{aligned} \tag{1.2.14}$$

The representation of a single-particle operator in terms of field operators is

$$A = \sum_{\sigma\sigma'} \int d^3\mathbf{r}\, \psi^\dagger_\sigma(\mathbf{r}, t) A(\mathbf{r}) \psi_{\sigma'}(\mathbf{r}, t), \tag{1.2.15}$$

where $A(\mathbf{r})$ is the operator in the position representation of ordinary quantum mechanics. If $A$ does not affect the spin of the particle we in addition have $\sigma = \sigma'$. The Hamiltonian can be split into two parts, one part called the non-interacting Hamiltonian containing only single-particle operators and one part called the interacting Hamiltonian containing the multi-particle operators. For the non-interacting Hamiltonian $\mathcal{H}_0$ we get

$$\mathcal{H}_0 = \int \mathrm{d}^3\mathbf{r} \sum_\sigma \psi^\dagger_\sigma(\mathbf{r}, t) H_0 \psi_\sigma(\mathbf{r}, t), \tag{1.2.16}$$

where $H_0$ is the non-interacting Hamiltonian in first quantization. For the interacting part of the Hamiltonian, we need terms that couple at least two electrons. If the interactions can be described by a potential that is independent of both spin and momentum, $V(\mathbf{r}, \mathbf{r}')$ then we have two possibilities that conserve angular momentum:

**Direct interaction:** If the two particles interact through $V(\mathbf{r}, \mathbf{r}')$ and stay in the same spin states the interaction is called direct. This gives us a Hamiltonian containing the product of two number operators $n_\sigma(\mathbf{r}, t)$ and $n_{\sigma'}(\mathbf{r}', t)$:

$$\mathcal{H}_\mathrm{d} = \frac{1}{2} \int \mathrm{d}^3\mathbf{r} \int \mathrm{d}^3\mathbf{r}'\, V(\mathbf{r}, \mathbf{r}') \sum_{\sigma\sigma'} \psi^\dagger_\sigma(\mathbf{r}, t) \psi_\sigma(\mathbf{r}, t) \psi^\dagger_{\sigma'}(\mathbf{r}', t) \psi_{\sigma'}(\mathbf{r}', t). \tag{1.2.17}$$

**Spin-exchange interaction:** If the two particles interacting through $V(\mathbf{r}, \mathbf{r}')$ end up swapping spin states it is called a spin-exchange interaction. This gives a slightly different expression for the spin-exchange Hamiltonian:

$$\mathcal{H}_\mathrm{e} = -\frac{1}{2} \int \mathrm{d}^3\mathbf{r} \int \mathrm{d}^3\mathbf{r}'\, V(\mathbf{r}, \mathbf{r}') \sum_{\sigma\sigma'} \psi^\dagger_\sigma(\mathbf{r}, t) \psi_{\sigma'}(\mathbf{r}, t) \psi^\dagger_\sigma(\mathbf{r}', t) \psi_{\sigma'}(\mathbf{r}', t). \tag{1.2.18}$$

To get information about the spin state of a particle we define the spin field operator, which is just the second quantized version of the Pauli vector

$$\boldsymbol{\sigma}(\mathbf{r},t) = \sum_{\sigma\sigma'} \psi^\dagger_\sigma(\mathbf{r},t)\boldsymbol{\sigma}_{\sigma\sigma'}\psi_{\sigma'}(\mathbf{r},t). \tag{1.2.19}$$

Taking the expectation value of the spin field operator

$$\mathbf{s}(\mathbf{r},t) = \langle \boldsymbol{\sigma}(\mathbf{r},t) \rangle \,, \tag{1.2.20}$$

gives us the expected value of the electron spin density.

### 1.2.3 Green's functions

To describe the electrons of a material it is useful to know the correlation between electrons at different points in space and time. The Green's functions are defined as expectation values of electron and hole correlations and contain information about the electronic properties of the material. Here we will use the formalism developed by L. V. Keldysh [41]. A comprehensive review was given by J. Rammer and H. Smith [42]. The Green's functions are then defined as

$$G^R_{\sigma\sigma'}(\mathbf{r},t;\mathbf{r}',t') = -i \left\langle [\psi_\sigma(\mathbf{r},t), \psi^\dagger_{\sigma'}(\mathbf{r}',t')]_+ \right\rangle \Theta(t-t'), \tag{1.2.21}$$

$$G^A_{\sigma\sigma'}(\mathbf{r},t;\mathbf{r}',t') = i \left\langle [\psi_\sigma(\mathbf{r},t), \psi^\dagger_{\sigma'}(\mathbf{r}',t')]_+ \right\rangle \Theta(t'-t), \tag{1.2.22}$$

$$G^K_{\sigma\sigma'}(\mathbf{r},t;\mathbf{r}',t') = -i \left\langle [\psi_\sigma(\mathbf{r},t), \psi^\dagger_{\sigma'}(\mathbf{r}',t')]_- \right\rangle, \tag{1.2.23}$$

where $\langle A(t) \rangle$ denotes the grand canonical average of $A(t)$,

$$\langle A(t) \rangle = \sum_{i,j} \langle i| \, A(t) W_j \, |j\rangle \, \langle j|i\rangle \,, \tag{1.2.24}$$

where $|i\rangle$ and $|j\rangle$ are different states of the system and $W_j$ is the probability of finding the system in state $|j\rangle$. In equilibrium $W_j$ is [43]

$$W_j = \frac{e^{-\beta E_j}}{\sum_i \langle i| \, e^{-\beta E_i} \, |i\rangle}, \tag{1.2.25}$$

where $E_j$ is the energy of state $|j\rangle$ measured with respect to the Fermi level and $\beta = 1/T$ is the inverse temperature. We see that the retarded Green's function $G^R$ vanishes unless $t > t'$. This means that electron creation has to happen first and annihilation afterwards. For the advanced Green's function $G^A$ it is the opposite, it vanishes if $t < t'$. So for $G^A$ the electron is annihilated first and then later it is created. Based on this we may conclude that the retarded Green's function describes the flow of electrons, while the advanced Green's function describes the flow of holes. If we want to calculate the occupation number we have to look at the Green's function in the same point in space and time and with equal spin, i.e. $r = r'$, $t = t'$, and $\sigma = \sigma'$. In this case, the anticommutator

becomes 1 and because of this $G^R$ and $G^A$ are constant. However, for $G^K$ we can use the anticommutational relation to rewrite the commutator as

$$-i[\psi_\sigma(\mathbf{r},t),\psi_\sigma^\dagger(\mathbf{r},t)]_- = i(2n_\sigma(\mathbf{r},t)-1), \tag{1.2.26}$$

where $n_\sigma(\mathbf{r},t)=\psi_\sigma^\dagger(\mathbf{r},t)\psi_\sigma(\mathbf{r},t)$ is the number operator for particles with spin $\sigma$ at position $\mathbf{r}$ at time $t$. As this is related to the occupation of the states we see that $G^K$ contains information about the non-equilibrium properties of the system, however, this is not the case for $G^R$ and $G^A$. Thus we conclude that $G^K$ is the only Green's function that contains information about non-equilibrium properties of the system [42, 44].

We also define the anomalous Green's functions that describe correlations between electrons at different points in space and time:

$$F^R_{\sigma\sigma'}(\mathbf{r},t;\mathbf{r}',t') = -i\left\langle[\psi_\sigma(\mathbf{r},t),\psi_{\sigma'}(\mathbf{r}',t')]_+\right\rangle\Theta(t-t'), \tag{1.2.27}$$
$$F^A_{\sigma\sigma'}(\mathbf{r},t;\mathbf{r}',t') = i\left\langle[\psi_\sigma(\mathbf{r},t),\psi_{\sigma'}(\mathbf{r}',t')]_+\right\rangle\Theta(t'-t), \tag{1.2.28}$$
$$F^K_{\sigma\sigma'}(\mathbf{r},t;\mathbf{r}',t') = -i\left\langle[\psi_\sigma(\mathbf{r},t),\psi_{\sigma'}(\mathbf{r}',t')]_-\right\rangle. \tag{1.2.29}$$

For most systems, the anomalous Green's functions will vanish, but importantly for our study, they are non-zero in superconducting materials. This is due to the formation of the condensate of Cooper pairs where we have two electrons paired. To get the related correlations for holes one takes the Hermitian conjugate of the anomalous Green's functions.

Since the indices $\sigma$ and $\sigma'$ can be either $\uparrow$ or $\downarrow$, the Green's function can be viewed as components of $2\times 2$ matrices in spin space: $\mathbf{G}^R$, $\mathbf{G}^A$, $\mathbf{G}^K$, $\mathbf{F}^R$, $\mathbf{F}^A$ and $\mathbf{F}^K$. These matrices are then used to construct $4\times 4$ matrices in Nambu-spin space:

$$\hat{\mathbf{G}}^R = \begin{bmatrix}\mathbf{G}^R & \mathbf{F}^R\\ (\mathbf{F}^R)^* & (\mathbf{G}^R)^*\end{bmatrix}, \tag{1.2.30}$$

$$\hat{\mathbf{G}}^A = \begin{bmatrix}\mathbf{G}^A & \mathbf{F}^A\\ (\mathbf{F}^A)^* & (\mathbf{G}^A)^*\end{bmatrix}, \tag{1.2.31}$$

$$\hat{\mathbf{G}}^K = \begin{bmatrix}\mathbf{G}^K & \mathbf{F}^K\\ -(\mathbf{F}^K)^* & -(\mathbf{G}^K)^*\end{bmatrix}. \tag{1.2.32}$$

These three matrices can now be collected in a single $8\times 8$ matrix in what is known as Keldysh space [42]:

$$\check{\mathbf{G}} = \begin{bmatrix}\hat{\mathbf{G}}^R & \hat{\mathbf{G}}^K\\ 0 & \hat{\mathbf{G}}^A\end{bmatrix}. \tag{1.2.33}$$

Collecting all the Green's functions into one Green's function in Keldysh space will later allow us to collect all the equations of motions for the different Green's functions in one compact equation for the Green's function in Keldysh space.

### 1.2.4 Quasiclassical approximation

The Green's function depends on its coordinates in two different ways. The first way is on the relative coordinate $|\mathbf{r}-\mathbf{r}'|$. As we assume that only particles close to the Fermi surface contribute to physical processes, the Green's function oscillates on a scale of the Fermi wavelength $\lambda_{\mathrm{F}}$. The second way is on the system which is under study. The characteristic length scales in typical systems of interest, such as the superconducting coherence length, are usually much larger than the Fermi wavelength $\lambda_F$. Thus we can often integrate out the dependence on the relative coordinate to get a quasiclassical Green's function $\check{\mathbf{g}}$. When we Fourier transform the relative coordinate the fast oscillations lead to a sharp peak around the Fermi surface, $|\mathbf{p}| = p_{\mathrm{F}}$, which we can then integrate out and only have a dependence on the direction of transport $\hat{\mathbf{p}}_{\mathrm{F}}$. This can not be done in problems where phase-coherence of the single-electron wave function controls the effect such as weak localization and persistent current. A review of the topic was given by W. Belzig et al. [44].

To find this quasiclassical Green's function $\check{\mathbf{g}}$ we start by switching to relative and center of mass coordinates:

$$\begin{aligned} \mathbf{r}_c &= \frac{\mathbf{r}+\mathbf{r}'}{2}, \qquad & \mathbf{s} &= \mathbf{r}-\mathbf{r}', \\ t_c &= \frac{t+t'}{2}, \qquad & u &= t-t'. \end{aligned} \tag{1.2.34}$$

We now Fourier transform the relative coordinates $\mathbf{s}$ and $u$:

$$\check{\mathbf{G}}(\mathbf{r}_c, \mathbf{p}, t_c, \epsilon) = \int \mathrm{d}u \exp(i\epsilon u) \int \mathrm{d}^3\mathbf{s} \exp(-i\mathbf{p}\cdot\mathbf{s}) \check{\mathbf{G}}(\mathbf{r}_c, \mathbf{s}, t_c, u). \tag{1.2.35}$$

When the Green's function depends on the center of mass coordinate $\mathbf{r}_c$ and time $t_c$ in addition to the momentum $\mathbf{p}$ and energy $\epsilon$ we say that we are in the mixed representation. At low temperatures all states with $|\mathbf{p}| \ll p_f$ are fully occupied, while states with $|\mathbf{p}| \gg p_f$ are all empty. Conservation of momentum thus implies that only states with momentum close to $p_f$ contribute to physical processes. This means that the Fourier transform leads to a sharp peak in $\mathbf{p}$ at $|\mathbf{p}| = p_F$, where $p_{\mathrm{F}} = \sqrt{2m\mu}$ and $\mu$ is the chemical potential. We approximate this peak as a delta function to get

$$\check{\mathbf{G}}(\mathbf{r}_c, \mathbf{p}, t_c, \epsilon) \approx -i\pi\delta(|\mathbf{p}| - p_{\mathrm{F}}) \check{\mathbf{g}}(\mathbf{r}_c, \hat{\mathbf{p}}_{\mathrm{F}}, t_c, \epsilon), \tag{1.2.36}$$

where $-i\pi$ is a normalization constant. To fix the value of the momentum to the Fermi momentum $p_{\mathrm{F}}$ we introduce the variable $\xi_{\mathbf{p}} = \mathbf{p}^2 - \mu$ and integrate over this variable

$$\check{\mathbf{g}}(\mathbf{r}_c, \hat{\mathbf{p}}_{\mathrm{F}}, t_c, \epsilon) = \frac{i}{\pi} \int \mathrm{d}\xi_{\mathbf{p}}\, \check{\mathbf{G}}(\mathbf{r}_c, \mathbf{p}, t_c, \epsilon). \tag{1.2.37}$$

Here we have obtained the quasiclassical Green's function $\check{\mathbf{g}}$. We can express it in terms of $\check{\mathbf{G}}(\mathbf{r}, t; \mathbf{r}', t')$ by putting together all steps performed above:

$$\begin{aligned} \check{\mathbf{g}}(\mathbf{r}_c, \hat{\mathbf{p}}_{\mathrm{F}}, t_c, \epsilon) =& \frac{i}{\pi} \int \mathrm{d}\xi_{\mathbf{p}} \int \mathrm{d}u \exp(i\epsilon u) \\ & \times \int \mathrm{d}^3\mathbf{s} \exp(-i\mathbf{p}\cdot\mathbf{s}) \check{\mathbf{G}}(\mathbf{r}_c + \mathbf{s}/2, t_c + u/2; \mathbf{r}_c - \mathbf{s}/2, t_c - u/2). \end{aligned} \tag{1.2.38}$$

Thus the quasiclassical Green's function is a function of the center of mass coordinate $\mathbf{r}_c$ and time $t_c$, transport direction at the Fermi surface $\hat{\mathbf{p}}_\mathrm{F}$ and energy $\epsilon$. The prefactor $i$ is important when we do complex conjugation since it leads to a sign change. As the quasiclassical Green's function can be written as

$$\check{\mathbf{g}} = \begin{bmatrix} \hat{\mathbf{g}}^R & \hat{\mathbf{g}}^K \\ 0 & \hat{\mathbf{g}}^A \end{bmatrix}, \tag{1.2.39}$$

the sign structure of Eqs. (1.2.30), (1.2.31) and (1.2.32) is changed and now becomes:

$$\hat{\mathbf{g}}^R = \begin{bmatrix} \mathbf{g}^R & \mathbf{f}^R \\ -(\mathbf{f}^R)^* & -(\mathbf{g}^R)^* \end{bmatrix}, \tag{1.2.40}$$

$$\hat{\mathbf{g}}^A = \begin{bmatrix} \mathbf{g}^A & \mathbf{f}^A \\ -(\mathbf{f}^A)^* & -(\mathbf{g}^A)^* \end{bmatrix}, \tag{1.2.41}$$

$$\hat{\mathbf{g}}^K = \begin{bmatrix} \mathbf{g}^K & \mathbf{f}^K \\ (\mathbf{f}^K)^* & (\mathbf{g}^K)^* \end{bmatrix}. \tag{1.2.42}$$

### 1.2.5 Bullet and ring product

The bullet product $A \bullet B(\mathbf{r}_c, \mathbf{p}, t_c, \epsilon)$ of two functions $A(\mathbf{r}, t, \mathbf{r}', t')$ and $B(\mathbf{r}, t, \mathbf{r}', t')$ is defined as the convolution over the middle spacetime variable and the Fourier transform of the relative coordinate:

$$\begin{aligned} A \bullet B(\mathbf{r}_c, \mathbf{p}, t_c, \epsilon) = \int \mathrm{d}^3(\mathbf{r} - \mathbf{r}')\, e^{-i\mathbf{p}\cdot(\mathbf{r}-\mathbf{r}')} \int \mathrm{d}(t - t')\, e^{i\epsilon(t-t')} \\ \times \int \mathrm{d}^3\mathbf{r}_1 \int \mathrm{d}t_1\, A(\mathbf{r}, t, \mathbf{r}_1, t_1) B(\mathbf{r}_1, t_1, \mathbf{r}', t'), \end{aligned} \tag{1.2.43}$$

where $\mathbf{r}_c = (\mathbf{r} + \mathbf{r}')/2$ and $t_c = (t + t')/2$. If one of the functions is a function of just 1 or 0 spacetime points the bullet product is the same as the Fourier transform of the relative coordinate with normal matrix multiplication of $A$ and $B$. It is shown in J. P. Morten's thesis [43] that Eq. (1.2.43) becomes:

$$\mathbf{A} \bullet \mathbf{B}(\mathbf{r}_c, \mathbf{p}, t_c, \epsilon) = \mathrm{e}^{\frac{i}{2}(\nabla^A_{\mathbf{r}_c}\nabla^B_{\mathbf{p}} - \nabla^A_{\mathbf{p}}\nabla^B_{\mathbf{r}_c})} \mathrm{e}^{\frac{i}{2}(\partial^A_{t_c}\partial^B_{\epsilon} - \partial^A_{\epsilon}\partial^B_{t_c})} \mathbf{A}(\mathbf{r}_c, \mathbf{p}, t_c, \epsilon)\mathbf{B}(\mathbf{r}_c, \mathbf{p}, t_c, \epsilon). \tag{1.2.44}$$

Here the exponential of the operators should be considered in terms of the Taylor expansion of the exponential $e^F = \sum_{n=0}^{\infty} \frac{1}{n!} F^n$. In addition, the superscript tells us which of the functions we are acting on:

$$(\nabla^A_{\mathbf{r}_c}\nabla^B_{\mathbf{p}})\mathbf{A}\mathbf{B} = (\nabla_{\mathbf{r}_c}\mathbf{A})(\nabla_{\mathbf{p}}\mathbf{B}). \tag{1.2.45}$$

If one writes out the exponentials one would see that this is an example of a Moyal product [45].

We can also separate out the space and momentum derivatives to define the ring product $\mathbf{A} \circ \mathbf{B}$ as

$$\mathbf{A} \circ \mathbf{B}(\mathbf{r}_c, \mathbf{p}, t_c, \epsilon) = \mathrm{e}^{\frac{i}{2}(\partial^A_{t_c}\partial^B_{\epsilon} - \partial^A_{\epsilon}\partial^B_{t_c})} \mathbf{A}(\mathbf{r}_c, \mathbf{p}, t_c, \epsilon)\mathbf{B}(\mathbf{r}_c, \mathbf{p}, t_c\epsilon). \tag{1.2.46}$$

If we are in the stationary case this reduces to normal matrix multiplication and the ring product is just the Fourier transform. We can now define the bullet product in terms of the ring product:

$$\mathbf{A} \bullet \mathbf{B}(\mathbf{r}_c, \mathbf{p}, t_c, \epsilon) = \mathrm{e}^{\frac{i}{2}(\nabla^A_{\mathbf{r}_c}\nabla^B_{\mathbf{p}} - \nabla^A_{\mathbf{p}}\nabla^B_{\mathbf{r}_c})}\mathbf{A} \circ \mathbf{B}(\mathbf{r}_c, \mathbf{p}, t_c, \epsilon). \tag{1.2.47}$$

Note that if we have no dependence on the space coordinate this reduces to the ring product. If we now expand the exponential we see that we get increasing power in the derivatives. As we ignore spatial variations on the scale of the Fermi wavelength, $\lambda_F$, we have that $\nabla_{\mathbf{r}} \sim L$ for $L \gg \lambda_p$, whereas $\nabla_p \sim \lambda_F$. Thus the expansion of the exponential is an expansion in $\lambda_F/L$, which is small as $L \gg \lambda_F$. This allows us to do an expansion known as the gradient approximation and keep only linear terms in the gradients [46]

$$\begin{aligned} \mathbf{A} \bullet \mathbf{B} &= (1 + \frac{i}{2}(\nabla^A_{\mathbf{r}_c}\nabla^B_{\mathbf{p}} - \nabla^A_{\mathbf{p}}\nabla^B_{\mathbf{r}_c}))\mathbf{A} \circ \mathbf{B} \\ &= \mathbf{A} \circ \mathbf{B} + \frac{i}{2}\{[(\nabla_{\mathbf{r}_c}\mathbf{A}) \circ (\nabla_{\mathbf{p}}\mathbf{B})] - [(\nabla_{\mathbf{p}}\mathbf{A}) \circ (\nabla_{\mathbf{r}_c}\mathbf{B})]\}. \end{aligned} \tag{1.2.48}$$

We also define bullet and ring commutators and anticommutators as

$$[\mathbf{A}, \mathbf{B}]^{\bullet}_{\pm} = \mathbf{A} \bullet \mathbf{B} \pm \mathbf{B} \bullet \mathbf{A}, \tag{1.2.49}$$

$$[\mathbf{A}, \mathbf{B}]^{\circ}_{\pm} = \mathbf{A} \circ \mathbf{B} \pm \mathbf{B} \circ \mathbf{A}. \tag{1.2.50}$$

In the gradient approximation, we can combine the bullet commutator and anticommutator with Eq. (1.2.48) to get:

$$[\mathbf{A}, \mathbf{B}]^{\bullet}_{\pm} = [\mathbf{A}, \mathbf{B}]^{\circ}_{\pm} + \frac{i}{2}\big([\nabla_{\mathbf{r}_c}\mathbf{A}, \nabla_{\mathbf{p}}\mathbf{B}]^{\circ}_{\mp} - [\nabla_{\mathbf{r}_c}\mathbf{B}, \nabla_{\mathbf{p}}\mathbf{A}]^{\circ}_{\mp}\big). \tag{1.2.51}$$

This is much simpler than the full bullet commutator and will help simplify the transport equations that we will derive in chapter 1.4.

### 1.2.6 Distribution function

The distribution function, $\hat{\mathbf{h}}$, is a matrix containing information about the energy distribution of the electrons and holes. One way to obtain $\hat{\mathbf{h}}$ is from the normalization condition $\check{\mathbf{g}} \circ \check{\mathbf{g}} = \mathbb{1}$ and it is defined via $\hat{\mathbf{g}}^K = \hat{\mathbf{g}}^R\hat{\mathbf{h}} - \hat{\mathbf{h}}\hat{\mathbf{g}}^A$. As $\hat{\mathbf{g}}^K$ is the only Green's function that contains information about non-equilibrium properties this means that $\hat{\mathbf{h}}$ also contains information about non-equilibrium properties. Thus, it is determined by a kinetic equation which one gets from the Keldysh component of the Usadel equation, which in a normal metal gives $\nabla^2\hat{\mathbf{h}} = 0$ when the normal metal is smaller than the inelastic scattering length [44, 46]. In the absence of spin-dependent transport it can be written as:

$$\hat{\mathbf{h}}(\epsilon) = \begin{bmatrix} h(\epsilon)\sigma^0 & 0 \\ 0 & -\tilde{h}(\epsilon)\sigma^0 \end{bmatrix}, \tag{1.2.52}$$

where $\tilde{h}(\epsilon) = h^*(-\epsilon)$. We can also express $h(\epsilon)$ as $h(\epsilon) = 1 - 2n(\epsilon)$, where $n(\epsilon)$ is the occupation number of the electron states with quasiparticle energy $\epsilon$, which in equilibrium

is just a Fermi-Dirac distribution. Inserting the Fermi-Dirac distribution for $n(\epsilon)$ we find that $h(\epsilon)$ in equilibrium at a temperature $T$ is

$$h(\epsilon) = \tanh\left(\frac{\epsilon}{2T}\right). \tag{1.2.53}$$

One should note that $\epsilon$ is measured with respect to the Fermi level, i.e., an energy $\epsilon = 0$ means that the quasiparticle has the same energy as the Fermi level. If we let $T \to 0$ the tanh function becomes a step function

$$h(\epsilon) = \theta(\epsilon) - \theta(-\epsilon), \tag{1.2.54}$$

where $\theta(\epsilon)$ is the Heaviside function.

To go out of equilibrium we can for example apply a voltage in such a way as to create a two-step distribution function. One way to do this is to have a wire connected to two reservoirs at voltages $\pm eV$, and connecting the system we wish to study to the middle of this wire. K. E. Nagaev [47] showed that this leads to a distribution function on the form:

$$h(\epsilon) = \left[\tanh\left(\frac{\epsilon + eV}{2T}\right) + \tanh\left(\frac{\epsilon - eV}{2T}\right)\right]/2, \tag{1.2.55}$$

and this was later confirmed experimentally by H. Pothier et al. [48]. Again taking the $T \to 0$ limit gives us a step function, but this time a two-step one with steps at $\pm eV$:

$$h(\epsilon) = \theta(\epsilon - eV) - \theta(-\epsilon - eV). \tag{1.2.56}$$

## 1.3 Hamiltonian

When we describe a quantum mechanical system we begin with a Hamiltonian that contains information about the properties of the system and how they contribute to the dynamics of the system. This Hamiltonian can be divided into contributions from the various properties, such as free electrons and superconductivity.

### 1.3.1 Non-interacting electrons

For particles that do not interact with each other moving in a background electromagnetic field with scalar potential $\varphi$ and vector potential $\mathbf{A}$, we know from classical mechanics that the Hamiltonian is [49]

$$H_0 = \frac{(\mathbf{p} - e\mathbf{A})^2}{2m} + e\varphi - \mu, \tag{1.3.1}$$

where we use the convention that $e < 0$ is the electron charge. The factor $-\mu$ means that we measure all energies relative to the Fermi energy. To get the first quantized Hamiltonian we do the replacement $\mathbf{p} \to -i\nabla$ and get

$$H_0 = -\frac{(\nabla - ie\mathbf{A})^2}{2m} + e\varphi - \mu. \tag{1.3.2}$$

We now introduce the gauge covariant derivative $\tilde{\nabla} = \nabla - ie\mathbf{A}$ and using Eq. (1.2.16) we find that the second quantized Hamiltonian is

$$\mathcal{H}_0 = \int \mathrm{d}^3\mathbf{r} \sum_\sigma \psi_\sigma^\dagger(\mathbf{r}, t) \left\{ -\frac{1}{2m}\tilde{\nabla}^2 + e\varphi(\mathbf{r}, t) - \mu \right\} \psi_\sigma(\mathbf{r}, t). \tag{1.3.3}$$

### 1.3.2 Superconductivity

When looking at superconductivity we consider electron-electron scattering by some attractive potential $V(\mathbf{r}, \mathbf{r}')$. If we consider direct interactions, the contributions to the Hamiltonian becomes

$$\mathcal{H}_\mathrm{d} = \frac{1}{2} \int \mathrm{d}^3\mathbf{r}\, \mathrm{d}^3\mathbf{r}'\, V(\mathbf{r}, \mathbf{r}') \sum_{\sigma\sigma'} \psi_\sigma^\dagger(\mathbf{r}, t)\psi_{\sigma'}^\dagger(\mathbf{r}', t)\psi_{\sigma'}(\mathbf{r}', t)\psi_\sigma(\mathbf{r}, t). \tag{1.3.4}$$

We now assume that this attraction is very short ranged so we can approximate it by [8, 50]

$$V(\mathbf{r}, \mathbf{r}') = \lambda(\mathbf{r})\delta(\mathbf{r} - \mathbf{r}'). \tag{1.3.5}$$

For the potential to be attractive, we need $\lambda(\mathbf{r}) < 0$. We also introduce the bosonic operators $b(\mathbf{r}, t) = \psi_\downarrow(\mathbf{r}, t)\psi_\uparrow(\mathbf{r}, t)$ and note that these operators describe pairs of electrons with opposite spins, which are known as Cooper pairs. This allows us to write the superconducting Hamiltonian as

$$\mathcal{H}_\mathrm{d} = \int \mathrm{d}^3\mathbf{r}\, \lambda(\mathbf{r}) b^\dagger(\mathbf{r}, t) b(\mathbf{r}, t). \tag{1.3.6}$$

As we have that $\lambda(\mathbf{r}) < 0$, we see that creating Cooper pairs lowers the energy of the superconductor. Thus, when we are at low temperatures, we expect that there will be formed many Cooper pairs since the thermal fluctuations are small. The collection of these pairs is what is referred to as the electronic condensate in a superconductor.

To simplify the superconducting Hamiltonian we do a mean-field approximation, introducing the mean field

$$b_\mu(\mathbf{r},t) = \langle b(\mathbf{r},t)\rangle\,, \tag{1.3.7}$$

and the fluctuation field

$$b_\delta(\mathbf{r},t) = b(\mathbf{r},t) - \langle b(\mathbf{r},t)\rangle\,. \tag{1.3.8}$$

In the mean-field approximation, we assume small fluctuations, i.e., $|b_\delta(\mathbf{r},t)| \ll |b_\mu(\mathbf{r},t)|$, thus we can ignore terms proportional to $b_\delta^2$. We also ignore the term containing $b_\mu^\dagger(\mathbf{r},t)b_\mu(\mathbf{r},t)$ as it is a constant and just leads to a shift in energy. Defining the superconducting order parameter $\tilde{\Delta}(\mathbf{r},t) = \lambda(\mathbf{r})b_\mu(\mathbf{r},t)$ allows us to write the Hamiltonian as

$$\mathcal{H}_\Delta = \int \mathrm{d}^3\mathbf{r}\,(\tilde{\Delta}\psi_\uparrow^\dagger(\mathbf{r},t)\psi_\downarrow^\dagger(\mathbf{r},t) + \tilde{\Delta}^*\psi_\downarrow(\mathbf{r},t)\psi_\uparrow(\mathbf{r},t)). \tag{1.3.9}$$

We now write $\tilde{\Delta}(\mathbf{r},t) = \Delta(\mathbf{r},t)e^{iv(\mathbf{r},t)}$ for two real functions $\Delta(\mathbf{r},t)$ and $v(\mathbf{r},t)$ which are called the superconducting gap and the superconducting phase. This allows us to do a gauge transformation to remove the superconducting phase [51]

$$\begin{aligned}
\psi_\sigma(\mathbf{r},t) &\to e^{iv(\mathbf{r},t)/2}\psi_\sigma(\mathbf{r},t),\\
\mathbf{A}(\mathbf{r},t) &\to \mathbf{A}(\mathbf{r},t) + \nabla v(\mathbf{r},t)/2e,\\
\varphi(\mathbf{r},t) &\to \varphi(\mathbf{r},t) - \partial_t v/2e,
\end{aligned} \tag{1.3.10}$$

and end up with the Hamiltonian [1]

$$\mathcal{H}_\Delta = \int \mathrm{d}^3\mathbf{r}\,\Delta(\mathbf{r},t)\left[\psi_\uparrow^\dagger(\mathbf{r},t)\psi_\downarrow^\dagger(\mathbf{r},t) + \psi_\downarrow(\mathbf{r},t)\psi_\uparrow(\mathbf{r},t)\right]. \tag{1.3.11}$$

### 1.3.3 Impurity scattering

A real material is unlikely to have no impurities and we thus introduce impurities to our model of the system. In impure superconductors, there can be both magnetic and non-magnetic impurities. The non-magnetic impurities contribute with an effective background potential $V_{\mathrm{imp}}(\mathbf{r})$ and using Eq. (1.2.16) we have the following contribution to the Hamiltonian [42, 43]

$$\mathcal{H}_{\mathrm{imp}} = \int \mathrm{d}^3\mathbf{r}\,V_{\mathrm{imp}}(\mathbf{r})\sum_\sigma \psi_\sigma^\dagger(\mathbf{r},t)\psi_\sigma(\mathbf{r},t). \tag{1.3.12}$$

Magnetic impurities have a spin field $\mathbf{s}(\mathbf{r},t)$ which couples to the spin field of an electron $\boldsymbol{\sigma}(\mathbf{r},t)$ through a scattering potential $V_{\mathrm{sf}}(\mathbf{r})$ via spin-flip scattering. The corresponding contribution to the Hamiltonian is

[1] This will be used for the derivation of the Usadel equation in chapter 1.4. When solving the linearized Usadel equation we will consider a solution with a phase, but that will be done in a proximitized normal metal and thus we use $\Delta = 0$ and the derived Usadel equation still holds for that case.

$$\mathcal{H}_{\rm sf} = \int \mathrm{d}^3\mathbf{r}\, V_{\rm sf}(\mathbf{r})\boldsymbol{\sigma}(\mathbf{r},t)\cdot\mathbf{s}(\mathbf{r},t). \tag{1.3.13}$$

Writing out $\boldsymbol{\sigma}(\mathbf{r},t)$ in terms of the field operators $\psi_\sigma(\mathbf{r},t)$ gives

$$\mathcal{H}_{\rm sf} = \int \mathrm{d}^3\mathbf{r}\, V_{\rm sf}(\mathbf{r}) \sum_{\sigma\sigma'} \psi^\dagger_\sigma(\mathbf{r},t)[\boldsymbol{\sigma}\cdot\mathbf{s}(\mathbf{r},t)]_{\sigma\sigma'}\psi_{\sigma'}(\mathbf{r},t). \tag{1.3.14}$$

### 1.3.4 Total Hamiltonian

For the entire system containing electromagnetic fields, superconductivity and impurity scattering the total Hamiltonian becomes the sum of Eqs. (1.3.3), (1.3.11), (1.3.12) and (1.3.14)

$$\mathcal{H} = \mathcal{H}_0 + \mathcal{H}_\Delta + \mathcal{H}_{\rm imp} + \mathcal{H}_{\rm sf}. \tag{1.3.15}$$

## 1.4 Equations of motion

The time evolution of the field operators $\psi(\mathbf{r},t)$ and $\psi^\dagger(\mathbf{r},t)$ are governed by the Heisenberg equation:

$$i\partial_t\psi_\sigma(\mathbf{r},t) = [\psi_\sigma(\mathbf{r},t),\mathcal{H}]_-, \quad i\partial_t\psi^\dagger_\sigma(\mathbf{r},t) = [\psi^\dagger_\sigma(\mathbf{r},t),\mathcal{H}]_-. \tag{1.4.1}$$

Using the Hamiltonian defined in (1.3.15) one can calculate the time evolution for this system as shown in the project thesis [40]. To simplify the resulting equations we define

$$B(\mathbf{r},t) = e\varphi(\mathbf{r},t) - \mu + V_{\text{imp}}(\mathbf{r},t), \tag{1.4.2}$$

$$C_{\sigma,\sigma'}(\mathbf{r},t) = -\frac{1}{2m}\delta_{\sigma\sigma'}\tilde{\nabla}^2 + V_{\text{sf}}[\boldsymbol{\sigma}\cdot\mathbf{s}(\mathbf{r},t)]_{\sigma,\sigma'}, \tag{1.4.3}$$

$$D_{\sigma\sigma'}(\mathbf{r},t) = \Delta(\mathbf{r},t)i\sigma^2_{\sigma\sigma'}. \tag{1.4.4}$$

This allows us to write the time evolution of the field operators as

$$i\partial_t\psi_\sigma(\mathbf{r},t) = B(\mathbf{r},t)\psi_\sigma(\mathbf{r},t) + \sum_{\sigma'} C_{\sigma\sigma'}(\mathbf{r},t)\psi_{\sigma'}(\mathbf{r},t) + \sum_{\sigma'} D_{\sigma\sigma'}(\mathbf{r},t)\psi^\dagger_{\sigma'}(\mathbf{r},t), \tag{1.4.5}$$

$$i\partial_t\psi^\dagger_\sigma(\mathbf{r},t) = \psi^\dagger_\sigma(\mathbf{r},t)B(\mathbf{r},t) + \sum_{\sigma'} \psi^\dagger_{\sigma'}(\mathbf{r},t)C^\dagger_{\sigma\sigma'}(\mathbf{r},t) - \sum_{\sigma'} \psi_{\sigma'}(\mathbf{r},t)D_{\sigma\sigma'}(\mathbf{r},t). \tag{1.4.6}$$

Here one should note that $\mathbf{C}^\dagger$ contains differential operators which act on $\psi^\dagger$ from the right. In addition, $\mathbf{D}$ is real and antisymmetric so $\mathbf{D}^\dagger = \mathbf{D}^T = -\mathbf{D}$ which means that the hermitian conjugate of (1.4.5) reproduces (1.4.6).

These equations for the time evolution of the field operators can be used to calculate the time evolution of the Green's functions. If we consider the retarded Green's function defined in (1.2.21) we need to take the derivative with respect to both $t$ and $t'$. Due to the Heaviside function, we will also get a term with a delta function in time and the resulting anticommutator gives a delta function in spin and space. Using that $\mathbf{C}$ and $\mathbf{D}$ can be written as matrices we get the time evolution of the retarded Green's function:

$$i\partial_t\mathbf{G}^R = (B+\mathbf{C})\mathbf{G}^R - \mathbf{D}\mathbf{F}^{R^*} + \delta(\mathbf{r}-\mathbf{r}')\delta(t-t'), \tag{1.4.7}$$

$$-i\partial_{t'}\mathbf{G}^R = \mathbf{G}^R(B'+\mathbf{C}'^\dagger) - \mathbf{F}^R\mathbf{D}' + \delta(\mathbf{r}-\mathbf{r}')\delta(t-t'). \tag{1.4.8}$$

The equations for $\mathbf{G}^{R^*}$, which are needed to formulate the equations for $\hat{\mathbf{G}}^R$, are found by simple complex conjugation.

For the anomalous Green's function, we get the same equation except that we interchange $\mathbf{G}^R$ and $\mathbf{F}^R$ and remove the delta functions due to the absence of a Heaviside function in the definition of $\mathbf{F}^R$. This gives time evolution as

$$i\partial_t\mathbf{F}^R = (B+\mathbf{C})\mathbf{F}^R - \mathbf{D}\mathbf{G}^{R^*}, \tag{1.4.9}$$

$$i\partial_{t'}\mathbf{F}^R = \mathbf{F}^R(B'+\mathbf{C}'^T) - \mathbf{G}^R\mathbf{D}'. \tag{1.4.10}$$

In Nambu-spin space we can collect Eqs. (1.4.7) and (1.4.9), and Eqs. (1.4.8) and (1.4.10), along with their complex conjugates in two $4\times4$ matrix equations:

$$i\hat{\boldsymbol{\rho}}_3\partial_t\hat{\mathbf{G}}^R = \hat{\mathbf{H}}\hat{\mathbf{G}}^R + \delta(\mathbf{r}-\mathbf{r}')\delta(t-t'), \tag{1.4.11}$$

$$-i\partial_{t'}\hat{\mathbf{G}}^R\hat{\boldsymbol{\rho}}_3 = \hat{\mathbf{G}}^R\underline{\hat{\mathbf{H}}}' + \delta(\mathbf{r}-\mathbf{r}')\delta(t-t'). \tag{1.4.12}$$

Here we have defined

$$\hat{\mathbf{H}} = \begin{bmatrix} B+\mathbf{C} & -\mathbf{D} \\ -\mathbf{D} & B+\mathbf{C}^* \end{bmatrix}, \tag{1.4.13}$$

and

$$\underline{\hat{\mathbf{H}}}' = \begin{bmatrix} B'+\mathbf{C}'^\dagger & -\mathbf{D}' \\ -\mathbf{D}' & B+\mathbf{C}'^T \end{bmatrix}. \tag{1.4.14}$$

Equations (1.4.11) and (1.4.12) are the Gor'kov equations [52] for the retarded Green's function. They are in principle exact, but solving them is in most cases a formidable task.

The same steps can be done for the advanced and Keldysh Green's function leading to equations on the same form with the retarded Green's function replaced by the advanced and Keldysh Green's functions. In the case of the Keldysh Green's function, they are defined without a Heaviside step function, so these equations will not have a delta function. Using Eq. (1.2.33) now gives

$$i\hat{\boldsymbol{\rho}}_3\partial_t\check{\mathbf{G}} = \hat{\mathbf{H}}\check{\mathbf{G}} + \delta(\mathbf{r}-\mathbf{r}')\delta(t-t'), \tag{1.4.15}$$

$$-i\partial_{t'}\check{\mathbf{G}}\hat{\boldsymbol{\rho}}_3 = \check{\mathbf{G}}\underline{\hat{\mathbf{H}}}' + \delta(\mathbf{r}-\mathbf{r}')\delta(t-t'). \tag{1.4.16}$$

These are the Gorkov equations for the Green's function in Keldysh space and these give a microscopic way to calculate the Green's function for a system described by the Hamiltonian in Eq. (1.3.15). However, in most cases they are very hard to solve as they depend on 8 coordinates $(\mathbf{r}, t, \mathbf{r}', t')$.

To get equations that are easier to solve, we first want to transform the Gorkov equations into a form that is more suitable for approximations. We begin by subtracting the two Gorkov equations (1.4.15) and (1.4.16)

$$i\hat{\boldsymbol{\rho}}_3\partial_t\check{\mathbf{G}} + i\partial_{t'}\check{\mathbf{G}}\hat{\boldsymbol{\rho}}_3 = \hat{\mathbf{H}}\check{\mathbf{G}} - \check{\mathbf{G}}\underline{\hat{\mathbf{H}}}'. \tag{1.4.17}$$

We now switch to the mixed representation

$$\begin{aligned} t_c &= \frac{t+t'}{2}, & \mathbf{r}_c &= \frac{\mathbf{r}+\mathbf{r}'}{2}, \\ u &= t-t, & \mathbf{s} &= \mathbf{r}-\mathbf{r}', \end{aligned} \tag{1.4.18}$$

and Fourier transform the relative coordinate. This means that the derivative transforms as

$$\begin{aligned} \partial_t &= \frac{1}{2}\partial_{t_c} - i\epsilon, & \nabla &= \frac{1}{2}\nabla_{\mathbf{r}_c} + i\mathbf{p}, \\ \partial_{t'} &= \frac{1}{2}\partial_{t_c} + i\epsilon, & \nabla' &= \frac{1}{2}\nabla_{\mathbf{r}_c} - i\mathbf{p}. \end{aligned} \tag{1.4.19}$$

Putting this back into equation (1.4.17) we can write the equation in terms of commutators and anticommutators

$$[\epsilon\hat{\boldsymbol{\rho}}_3, \check{\mathbf{G}}]_- + \frac{i}{2}[\hat{\boldsymbol{\rho}}_3, \partial_{t_c}\check{\mathbf{G}}]_+ = \hat{\mathbf{H}}\check{\mathbf{G}} - \check{\mathbf{G}}\underline{\hat{\mathbf{H}}}'. \tag{1.4.20}$$

As $\epsilon\hat{\boldsymbol{\rho}}_3$ is independent of time, position and momentum and linear in energy the left-hand side of this equation can be written as a bullet commutator

$$[\epsilon\hat{\boldsymbol{\rho}}_3, \check{\mathbf{G}}]_-^\bullet = [\epsilon\hat{\boldsymbol{\rho}}_3, \check{\mathbf{G}}]_- + \frac{i}{2}[\epsilon\hat{\boldsymbol{\rho}}_3, \partial_{t_c}\check{\mathbf{G}}]_+. \tag{1.4.21}$$

Now, consider the right-hand side of Eq. (1.4.20). Both $B$ and $\mathbf{D}$ depend only on a single spacetime coordinate. Thus for these contributions, the bullet product is the same as normal matrix multiplication. For $B$ we get

$$\{\hat{\mathbf{H}}\check{\mathbf{G}} - \check{\mathbf{G}}\underline{\hat{\mathbf{H}}}'\}_B = [e\varphi + V_{\text{imp}}, \check{\mathbf{G}}]_-^\bullet, \tag{1.4.22}$$

where $\mu$ has dropped out since it is a constant, while for $\mathbf{D}$ we get

$$\{\hat{\mathbf{H}}\check{\mathbf{G}} - \check{\mathbf{G}}\underline{\hat{\mathbf{H}}}'\}_D = [-\Delta i\hat{\boldsymbol{\rho}}_2, \check{\mathbf{G}}]_-^\bullet. \tag{1.4.23}$$

Due to the complex conjugate structure of $\mathbf{C}$ on the diagonal of $\hat{\mathbf{H}}$ and $\hat{\mathbf{H}}'$, we introduce

$$\hat{\mathbf{A}} = \begin{bmatrix} \mathbf{A}\sigma_0 & 0 \\ 0 & -\mathbf{A}\sigma_0 \end{bmatrix}, \tag{1.4.24}$$

and

$$\hat{\boldsymbol{\sigma}} = \begin{bmatrix} \boldsymbol{\sigma} & 0 \\ 0 & \boldsymbol{\sigma}^* \end{bmatrix}. \tag{1.4.25}$$

This allows us to write the $\mathbf{C}$ contributions as

$$\begin{aligned}\{\hat{\mathbf{H}}\check{\mathbf{G}} - \check{\mathbf{G}}\underline{\hat{\mathbf{H}}}'\}_C = &-\frac{i\mathbf{p}}{m}\cdot\{\nabla_{\mathbf{r}_c}\check{\mathbf{G}} - ie[\hat{\mathbf{A}}, \check{\mathbf{G}}]_-^\bullet\} + \frac{ie}{4m}\{[\nabla_{\mathbf{r}_c}\cdot\hat{\mathbf{A}}, \check{\mathbf{G}}]_+^\bullet \\ &+ [\hat{\mathbf{A}}, \nabla_{\mathbf{r}_c}\check{\mathbf{G}}]_+^\bullet - 2ie[\hat{\mathbf{A}}^2, \check{\mathbf{G}}]_-^\bullet\} + [V_{\text{sf}}\mathbf{s}\cdot\hat{\boldsymbol{\sigma}}, \check{\mathbf{G}}]_-^\bullet.\end{aligned} \tag{1.4.26}$$

As the differential operators in $\underline{\hat{\mathbf{H}}}'$ act towards the left, there are no $\nabla_{\mathbf{r}_c}^2$ terms as they cancel out. In addition, $\mathbf{p}$ commutes with $\nabla_{\mathbf{r}_c}$, so those two terms have been added together. Combining Eqs. (1.4.21), (1.4.22), (1.4.23) and (1.4.26) we get the exact transport equation for a system described by the Hamiltonian (1.3.15):

$$\begin{aligned}\frac{\mathbf{p}}{m}\cdot\{\nabla_{\mathbf{r}_c}\check{\mathbf{G}} - i[\hat{\mathbf{A}}, \check{\mathbf{G}}]_-^\bullet\} =&\, i[\epsilon\hat{\boldsymbol{\rho}}_3 + \Delta i\hat{\boldsymbol{\rho}}_2 - e\varphi - V_{\text{imp}} - V_{\text{sf}}\mathbf{s}\cdot\hat{\boldsymbol{\sigma}}, \check{\mathbf{G}}]_-^\bullet \\ &+ \frac{e}{4m}\{[\nabla_{\mathbf{r}_c}\hat{\mathbf{A}}, \check{\mathbf{G}}]_+^\bullet + [\hat{\mathbf{A}}, \nabla_{\mathbf{r}_c}\check{\mathbf{G}}]_+^\bullet\} - \frac{i}{2m}[\hat{\mathbf{A}}^2, \check{\mathbf{G}}]_-^\bullet.\end{aligned} \tag{1.4.27}$$

This equation is much more suitable for approximations than the Gorkov equations (1.4.15) and (1.4.16). We first do the quasiclassical approximation where we consider all energies to be small compared to the Fermi energy, which is equivalent to assuming that all characteristic length scales of the system are much larger than the Fermi wavelength, $\lambda_F$.

Assuming that these characteristic length scales are of size $L$, we can make an expansion in the small parameter $\eta = L/\lambda_F$. All three terms in the second line of Eq. (1.4.27) are proportional to $\eta^2$, while the rest of the terms in (1.4.27) are proportional to $\eta$. Thus, we ignore the three terms on the second line. In the bullet product, we expand the exponential containing the derivatives with respect to space and momentum. As $\nabla_{\mathbf{r}} \sim \frac{1}{L}$ and $\nabla_{\mathbf{p}} \sim \lambda_{\mathrm{F}}$ we see that this expansion is an expansion in $\eta$, and we thus only keep the zeroth order and replace all bullet commutators with ring commutators. Since the quasiclassical approximation only considers electrons close to the Fermi surface, we replace $\mathbf{p}/m$ by $\mathbf{v}_{\mathrm{F}}$ and $\check{\mathbf{G}}(\mathbf{r}, \mathbf{p}, \epsilon, t)$ by $\check{\mathbf{g}}(\mathbf{r}, \hat{\mathbf{p}}_{\mathrm{F}}, \epsilon, t)$. This gives us the quasiclassical transport equation:

$$\mathbf{v}_{\mathrm{F}} \cdot \tilde{\nabla}\check{\mathbf{g}} = i[\epsilon\hat{\boldsymbol{\rho}}_3 + \Delta i\hat{\boldsymbol{\rho}}_2 - e\varphi - V_{\mathrm{imp}} - V_{\mathrm{sf}}\,\mathbf{s}\cdot\hat{\boldsymbol{\sigma}}, \check{\mathbf{g}}]^{\circ}_{-}. \tag{1.4.28}$$

This equation is known as the Eilenberger equation [44, 53] and is a tremendous simplification when compared to the exact transport equation (1.4.27). We have removed three non-trivial terms and no longer have an infinite series of differentiations with respect to $\mathbf{r}$ and $\mathbf{p}$. In addition, $\check{\mathbf{g}}$ is independent of the magnitude of $\mathbf{p}$, so we also have one less degree of freedom. Finally, in the stationary limit $\partial_t\check{\mathbf{g}} = 0$, the right-hand side of Eq. (1.4.28) reduces to a regular commutator which further simplifies calculations.

To make further simplifications we consider a material with a relatively high density of non-magnetic impurities. This leads to the Eilenberger equation (1.4.28) being dominated by $V_{\mathrm{imp}}$ and the Green's function becomes nearly isotropic. Thus, we make a first-order expansion in spherical harmonics:

$$\check{\mathbf{g}}(\mathbf{r}, \hat{\mathbf{p}}_{\mathrm{F}}, \epsilon, t) = \check{\mathbf{g}}_{\mathrm{s}}(\mathbf{r}, \epsilon, t) + \hat{\mathbf{p}}_{\mathrm{F}} \cdot \check{\mathbf{g}}_{\mathrm{p}}(\mathbf{r}, \epsilon, t). \tag{1.4.29}$$

Here the $s$-wave component $\check{\mathbf{g}}_{\mathrm{s}}$ is the isotropic part while the $p$-wave component $\check{\mathbf{g}}_{\mathrm{p}}$ is the linearized anisotropy with respect to the transport direction $\hat{\mathbf{p}}_{\mathrm{F}}$. In this limit, we can also simplify the expressions for the impurity scattering potential $V_{\mathrm{imp}}$ and the spin-flip scattering $V_{\mathrm{sf}}\,\mathbf{s}\cdot\hat{\boldsymbol{\sigma}}$. To do this, one averages the Green's function over a large amount of random, either non-magnetic or magnetic, impurities. This average then leads to the impurity potentials being replaced by self energies. Introducing the momentum-relaxation time $\tau_0$ and the spin-relaxation time $\tau_s$ it is shown by J. P. Morten [43] and J. Rammer and H. Smith [42] that the self-energies replacing the impurity potentials are

$$V_{\mathrm{imp}} \to -\frac{i}{2\tau_0}\check{\mathbf{g}}_{\mathrm{s}}, \tag{1.4.30}$$

and

$$V_{\mathrm{sf}}\,\mathbf{s}\cdot\hat{\boldsymbol{\sigma}} \to -\frac{i}{2\tau_{\mathrm{s}}}\hat{\boldsymbol{\rho}}_3\check{\mathbf{g}}_{\mathrm{s}}\hat{\boldsymbol{\rho}}_3. \tag{1.4.31}$$

Putting these back into the Eilenberger equation, multiplying by $\hat{\mathbf{p}}_{\mathrm{F}}$, only including the impurity term on the right-hand side of the equation and using the normalization condition [54]

$$\check{\mathbf{g}}_{\mathrm{s}} \circ \check{\mathbf{g}}_{\mathrm{s}} = \mathbb{1}, \tag{1.4.32}$$

one can express the anisotropic part of the Green's function as

$$\check{\mathbf{g}}_{\mathrm{p}} = -\frac{v_{\mathrm{F}}}{2v_0}\check{\mathbf{g}}_{\mathrm{s}} \circ \tilde{\nabla}\check{\mathbf{g}}_{\mathrm{s}}. \tag{1.4.33}$$

Thus, the isotropic part of the Green's function captures all the essential physics of the problem and we only need to solve for it. We use this expression to eliminate $\check{\mathbf{g}}_\mathrm{p}$ from Eq. (1.4.29) and introduce $v_\mathrm{s} = 1/2\tau_\mathrm{s}$ and the diffusion coefficient $D = \frac{1}{3}\tau_0 v_\mathrm{F}^2$:

$$iD\tilde{\nabla} \cdot (\check{\mathbf{g}}_\mathrm{s} \circ \nabla \check{\mathbf{g}}_\mathrm{s}) = [\epsilon \hat{\boldsymbol{\rho}}_3 + \Delta i \hat{\boldsymbol{\rho}}_2 - e\varphi + i v_\mathrm{s} \hat{\boldsymbol{\rho}}_3 \check{\mathbf{g}}_\mathrm{s} \hat{\boldsymbol{\rho}}_3, \check{\mathbf{g}}_\mathrm{s}]_-^\circ. \tag{1.4.34}$$

This equation is known as the Usadel equation [55] and is much simpler to solve than the Eilenberger equation (1.4.28). While we have gone from a first-order differential equation to a second-order one, we have also removed the dependency on the direction of the momentum, such that we have two fewer degrees of freedom.

## 1.5 Weak proximity effect

While the Usadel equation describes dirty systems well, solving the full Usadel equation analytically is still a formidable task. One way to get an equation that is easier to solve analytically is to derive the so-called linearized Usadel equation [56]. This is a good description for a normal metal in contact with a superconductor with a resistive interface between the normal metal and superconductor. This resistivity leads to weak proximity-induced superconductivity in the normal metal and thus the solution is very close to the solution for a bulk normal metal. Then we can treat the addition of superconductivity in the normal metal as a weak perturbation. We will also assume that the system has been kept in a specific state for a sufficiently long time to be time-independent, that is a steady-state approximation. In this case, the ring products in Eq. (1.4.34) become normal matrix products as all higher-order terms contain a derivative with respect to the time which will be zero.

### 1.5.1 Linearized Usadel equation

In the time-independent case, the Usadel equation (1.4.34) for a superconducting metal with an externally applied magnetic field becomes

$$\tilde{\nabla} \cdot \check{\mathbf{I}} = i[\check{\boldsymbol{\Sigma}}, \check{\mathbf{g}}]_- = i \begin{bmatrix} [\hat{\boldsymbol{\Sigma}}, \hat{\mathbf{g}}^R]_- & [\hat{\boldsymbol{\Sigma}}, \hat{\mathbf{g}}^K]_- \\ 0 & [\hat{\boldsymbol{\Sigma}}, \hat{\mathbf{g}}^A]_- \end{bmatrix}, \tag{1.5.1}$$

where

$$\hat{\boldsymbol{\Sigma}} = \epsilon \hat{\boldsymbol{\rho}}_3 + \Delta i \hat{\boldsymbol{\rho}}_2, \tag{1.5.2}$$

and we have defined the matrix current

$$\check{\mathbf{I}} = -D\check{\mathbf{g}}\tilde{\nabla}\check{\mathbf{g}} = -D \begin{bmatrix} \hat{\mathbf{g}}^R\tilde{\nabla}\hat{\mathbf{g}}^R & \hat{\mathbf{g}}^R\tilde{\nabla}\hat{\mathbf{g}}^K - \hat{\mathbf{g}}^K\tilde{\nabla}\hat{\mathbf{g}}^A \\ 0 & \hat{\mathbf{g}}^A\tilde{\nabla}\hat{\mathbf{g}}^A \end{bmatrix}. \tag{1.5.3}$$

The subscript s has been dropped from the isotropic part of the Green's function, so when we write $\check{\mathbf{g}}$ from now on it is the isotropic part $\check{\mathbf{g}}_\mathrm{s}$ that is meant. One should also note that, apart from a factor 1/3, the matrix current is the same as the linearized anisotropy of the Green's function when comparing with Eq. (1.4.33). This is called the matrix current [57] since it contains information about all the currents in the system, i.e., electric, energy and spin currents. Later it will be used to calculate the supercurrent density.

It can be shown that both $\hat{\mathbf{g}}^A$ and $\hat{\mathbf{g}}^K$ can be expressed through $\hat{\mathbf{g}}^R$ [44, 43] as

$$\hat{\mathbf{g}}^A = -\hat{\boldsymbol{\rho}}_3\hat{\mathbf{g}}^R\hat{\boldsymbol{\rho}}_3, \tag{1.5.4}$$

and

$$\hat{\mathbf{g}}^K = \hat{\mathbf{g}}^R\hat{\mathbf{h}} - \hat{\mathbf{h}}\hat{\mathbf{g}}^A. \tag{1.5.5}$$

This means that it is sufficient to find an expression for $\hat{\mathbf{h}}$ as discussed in section 1.2.6 and to solve

$$-D\tilde{\nabla} \cdot (\hat{\mathbf{g}}^R\tilde{\nabla}\hat{\mathbf{g}}^R) = i[\hat{\boldsymbol{\Sigma}}, \hat{\mathbf{g}}^R]_-. \tag{1.5.6}$$

In a normal metal, where $\Delta = 0$, the simplest solution to the Usadel equation is

$$\hat{\mathbf{g}}^R = \hat{\boldsymbol{\rho}}_3, \tag{1.5.7}$$

as this commutes with $\hat{\boldsymbol{\Sigma}}$, the derivative is zero and it respects the normalization condition $\hat{\mathbf{g}}^R \circ \hat{\mathbf{g}}^R = \mathbb{1}$.

The idea behind the linearized Usadel equation is that for a normal metal in contact with a superconductor through a resistive barrier, the solution is almost the same as for a normal metal, just with a small perturbation. For a superconductor, the BCS solution is [56]

$$\hat{\mathbf{g}}^R_{\mathrm{BCS}} = \begin{bmatrix} g_{\mathrm{BCS}}\sigma^0 & f_{\mathrm{BCS}} i\sigma^2 \\ -\tilde{f}_{\mathrm{BCS}} i\sigma^2 & -g_{\mathrm{BCS}}\sigma^0 \end{bmatrix}. \tag{1.5.8}$$

Thus, when we view it as a weak perturbation, we only consider the $f$ terms. In the normal metal we already have $\hat{\boldsymbol{\rho}}_3$ on the diagonal and the contributions from perturbation of the diagonal elements are thus ignored. However, the off-diagonal elements are zero and thus we cannot ignore the perturbations from the $f$ terms. This gives the solution on the form

$$\hat{\boldsymbol{g}}^R = \hat{\boldsymbol{\rho}}_3 + \hat{\boldsymbol{f}}, \tag{1.5.9}$$

where

$$\hat{\boldsymbol{f}} = \mathrm{antidiag}(f, -f, -\tilde{f}, \tilde{f}) = \begin{bmatrix} 0 & f i\sigma^2 \\ -\tilde{f} i\sigma^2 & 0 \end{bmatrix}, \tag{1.5.10}$$

and $\tilde{f}(\epsilon, \mathbf{r}) = f^*(-\epsilon, \mathbf{r})$. This limit is called the weak proximity regime. When we linearize the Usadel equation, we assume that $f$ is small so we can neglect all terms of order $\mathcal{O}(f^2)$. When neglecting $\mathcal{O}(f^2)$ terms it is easy to show that this solution also satisfies the normalization condition $(\hat{\boldsymbol{g}}^R)^2 = \mathbb{1}$ as the cross terms cancel and the square of $\hat{\boldsymbol{\rho}}_3$ is $\mathbb{1}$.

To derive the linearized Usadel equation, we substitute (1.5.9) into (1.5.6) and set $\Delta = 0$ as we consider a normal metal. Using that the vector potential $\mathbf{A}$ and the gradient $\nabla$ commutes in the Coloumb gauge $\nabla \cdot \mathbf{A} = 0$ and neglecting terms of order $f^2$ gives

$$\begin{aligned} &-D \begin{bmatrix} 0 & (\nabla^2 f - 4ie(\mathbf{A}\cdot\nabla)f - 4e^2\mathbf{A}^2 f) i\sigma^2 \\ (\nabla^2 \tilde{f} + 4ie(\mathbf{A}\cdot\nabla)\tilde{f} - 4e^2\mathbf{A}^2\tilde{f}) i\sigma^2 & 0 \end{bmatrix} \\ &= 2i\epsilon \begin{bmatrix} 0 & f i\sigma^2 \\ \tilde{f} i\sigma^2 & 0 \end{bmatrix}. \end{aligned} \tag{1.5.11}$$

Since the left-hand side and right-hand side of the equation have the same matrix structure they are two scalar equations for $f$ and $\tilde{f}$. Using the Coulomb gauge again, they can be rewritten as

$$(\nabla - 2ie\mathbf{A})^2 f = -2i\frac{\epsilon}{D} f, \tag{1.5.12}$$

$$(\nabla + 2ie\mathbf{A})^2 \tilde{f} = -2i\frac{\epsilon}{D} \tilde{f}. \tag{1.5.13}$$

We see that we get Eq. (1.5.13) from Eq. (1.5.12) by taking the complex conjugate and flipping the sign of $\epsilon$, which is as expected based on the definition of $\tilde{f}$. Thus we only need to solve one of the equations. This is the linearized Usadel equation [58] and we see that it is much simpler than the Usadel equation (1.4.34). We have gone from a matrix

equation to a single scalar equation, we have removed all ring products so we no longer have an infinite number of differentiations with respect to time and energy and we have removed the commutators from the right-hand side. We are left with a partial differential equation where we have first and second-order derivatives with respect to all 3 spatial coordinates, but depending on the geometry and symmetries this can also be simplified even further.

### 1.5.2 Supercurrent density

The matrix current defined in Eq. (1.5.3) can be used to calculate the supercurrent density in a system [44]. A full derivation is given in the supplementary information of [59], which gives

$$\mathbf{J}_e = -\frac{1}{8} e N_f \int_0^{w_c} d\epsilon \, \mathrm{Re}\,\mathrm{Tr}(\hat{\boldsymbol{\rho}}_3 \hat{\mathbf{I}}^K), \tag{1.5.14}$$

where $N_f$ is the density of states at the Fermi surface, $w_c$ is the Debye frequency as this is the frequency at which the phonon-mediated attractions stop being attractive, Re means taking the real part of the expression and Tr is the trace. Let us now consider the matrix current when $\hat{\mathbf{g}}^K$ is defined by (1.5.5). From Eq. (1.5.3) we have

$$\begin{aligned}\hat{\mathbf{I}}^K = &- D\big\{\nabla\hat{\mathbf{h}} - \hat{\mathbf{g}}^R(\nabla\hat{\mathbf{h}})\hat{\mathbf{g}}^A + \hat{\mathbf{g}}^R(\nabla\hat{\mathbf{g}}^R)\hat{\mathbf{h}} - \hat{\mathbf{h}}\hat{\mathbf{g}}^A\nabla\hat{\mathbf{g}}^A \\ &- ie\mathbf{A}([\hat{\boldsymbol{\rho}}_3, \hat{\mathbf{h}}]_- + \hat{\mathbf{g}}^R[\hat{\boldsymbol{\rho}}_3, \hat{\mathbf{g}}^R]_-\hat{\mathbf{h}} - \hat{\mathbf{h}}\hat{\mathbf{g}}^A[\hat{\boldsymbol{\rho}}_3, \hat{\mathbf{g}}^A]_- - \hat{\mathbf{g}}^R[\hat{\boldsymbol{\rho}}_3, \hat{\mathbf{h}}]_-\hat{\mathbf{g}}^A)\big\}.\end{aligned} \tag{1.5.15}$$

Let us now consider a normal metal with weak proximity-induced superconductivity, where $\hat{\mathbf{g}}^R$ is given by Eq. (1.5.9). We also assume a spatially homogeneous distribution function $\nabla\hat{\mathbf{h}} = 0$, as we will later use the distribution functions defined in section 1.2.6. This homogeneity means that we assume that all resistive currents are zero. A resistive current is driven by a gradient in the voltage and implies a gradient in the distribution function. To simplify Eq. (1.5.15) we need an expression for $\hat{\mathbf{g}}^A$. To find this we put Eq. (1.5.9) into Eq. (1.5.4):

$$\hat{\mathbf{g}}^A = -\hat{\boldsymbol{\rho}}_3 + \hat{\mathbf{f}}(-\epsilon). \tag{1.5.16}$$

Putting (1.5.9) and (1.5.16) back into (1.5.15), using $\hat{\mathbf{h}}$ as defined in (1.2.52) and the assumption that $\nabla\hat{\mathbf{h}} = 0$, we can calculate the commutators in the matrix current. The diagonality of $\hat{\mathbf{h}}$ also means that $[\hat{\boldsymbol{\rho}}_3, \hat{\mathbf{h}}]_- = 0$, so those terms also drop out. This gives

$$\begin{aligned}\hat{\mathbf{I}}^K = &- D\left\{\left[\hat{\boldsymbol{\rho}}_3 + \hat{\mathbf{f}}(\epsilon)\right]\nabla\hat{\mathbf{f}}(\epsilon)\hat{\mathbf{h}} - \hat{\mathbf{h}}\left[-\hat{\boldsymbol{\rho}}_3 + \hat{\mathbf{f}}(-\epsilon)\right]\nabla\hat{\mathbf{f}}(-\epsilon)\right\} \\ &+ 2iDe\mathbf{A}\left\{\left[\hat{\boldsymbol{\rho}}_3 + \hat{\mathbf{f}}(\epsilon)\right]\hat{\boldsymbol{\rho}}_3\hat{\mathbf{f}}(\epsilon)\hat{\mathbf{h}} - \hat{\mathbf{h}}\left[-\hat{\boldsymbol{\rho}}_3 + \hat{\mathbf{f}}(-\epsilon)\right]\hat{\boldsymbol{\rho}}_3\hat{\mathbf{f}}(-\epsilon)\right\}.\end{aligned} \tag{1.5.17}$$

To calculate the supercurrent from Eq. (1.5.14), we now multiply Eq. (1.5.17) with $\hat{\boldsymbol{\rho}}_3$ and take the real part of the trace of the resulting matrix. First, we note that $\hat{\mathbf{f}}$ is anti-diagonal while $\hat{\boldsymbol{\rho}}_3$ and $\hat{\mathbf{h}}$ are diagonal, and a diagonal matrix multiplied with an anti-diagonal matrix is anti-diagonal and thus has no trace. This means that terms that contain only one $\hat{\mathbf{f}}$ will not contribute to the trace. We also use that $\hat{\mathbf{f}}^2$ is diagonal so it commutes with $\hat{\mathbf{h}}$ which is also diagonal, which allows us to move all the $\hat{\mathbf{h}}$ terms before the $\hat{\mathbf{f}}$ terms. This

gives

$$\begin{aligned}\operatorname{Re}\operatorname{Tr}(\hat{\boldsymbol{\rho}}_3\hat{\mathbf{I}}^K) = &- D\operatorname{Re}\operatorname{Tr}\Big\{\hat{\boldsymbol{\rho}}_3\hat{\mathbf{h}}\Big[\operatorname{diag}(f\nabla\tilde{f}, f\nabla\tilde{f}, \tilde{f}\nabla f, \tilde{f}\nabla f)(\epsilon)\\ &\qquad - \operatorname{diag}(f\nabla\tilde{f}, f\nabla\tilde{f}, \tilde{f}\nabla f, \tilde{f}\nabla f)(-\epsilon)\Big]\Big\}\\ &+ 2De\mathbf{A}\operatorname{Re}\operatorname{Tr}\Big\{i\hat{\boldsymbol{\rho}}_3\hat{\mathbf{h}}\Big[\operatorname{diag}(-f\tilde{f}, -f\tilde{f}, \tilde{f}f, \tilde{f}f)(\epsilon)\\ &\qquad - \operatorname{diag}(-f\tilde{f}, -f\tilde{f}, \tilde{f}f, \tilde{f}f)(-\epsilon)\Big]\Big\}.\end{aligned} \tag{1.5.18}$$

We now introduce this back into Eq. (1.5.14), perform the traces, write out $\tilde{h}(\epsilon) = h^*(-\epsilon)$ and $\tilde{f}(\epsilon) = f^*(-\epsilon)$ and make use of the fact that we can freely complex conjugate within Re:

$$\begin{aligned}\mathbf{J}_e = \frac{1}{4}eN_f\int_0^{w_c} d\epsilon\Big[&D\operatorname{Re}\big\{h(\epsilon)\left[f(\epsilon)\nabla f^*(-\epsilon) - f(-\epsilon)\nabla f^*(\epsilon)\right]\\ &\qquad + h(-\epsilon)\left[f(-\epsilon)\nabla f^*(\epsilon) - f(\epsilon)\nabla f^*(-\epsilon)\right]\big\}\\ &+ 2De\mathbf{A}\operatorname{Re}\big\{ih(\epsilon)\left[f(\epsilon)f^*(-\epsilon) - f(-\epsilon)f^*(\epsilon)\right]\\ &\qquad + ih(-\epsilon)\left[f(-\epsilon)f^*(\epsilon) - f(\epsilon)f^*(-\epsilon)\right]\big\}\Big].\end{aligned} \tag{1.5.19}$$

Here we see that the second $h$ and $f$ terms in the square brackets in each line are the same as the first ones, just with a sign change on $\epsilon$. This means that we can merge them together and integrate from $-w_c$ instead of 0. In addition, as we can freely complex conjugate inside Re we use that $f(\epsilon)f^*(-\epsilon) = -[f(-\epsilon)f^*(\epsilon)]^*$. This gives the supercurrent density

$$\begin{aligned}\mathbf{J}_e = \frac{1}{4}eN_fD\int_{-w_c}^{w_c} d\epsilon\Big[&\operatorname{Re}\big\{h(\epsilon)\left[f(\epsilon)\nabla f^*(-\epsilon) - f(-\epsilon)\nabla f^*(\epsilon)\right]\big\}\\ &+ 4e\mathbf{A}\operatorname{Re}\big\{ih(\epsilon)f(\epsilon)f^*(-\epsilon)\big\}\Big].\end{aligned} \tag{1.5.20}$$

If we now consider an anti-symmetric distribution function as the one defined in (1.2.56), we can use that the gradient terms are antisymmetric in $\epsilon$. For the last term, we see that by letting $\epsilon \to -\epsilon$ and taking the complex conjugate within Re, we get back the same expression. This means that we can simplify the integral to be from 0 to $w_c$ and multiply with a factor of 2. Finally, we get the supercurrent density as

$$\begin{aligned}\mathbf{J}_e = \frac{1}{2}eN_fD\int_0^{w_c} d\epsilon\Big[&\operatorname{Re}\big\{h(\epsilon)\left[f(\epsilon)\nabla f^*(-\epsilon) - f(-\epsilon)\nabla f^*(\epsilon)\right]\big\}\\ &+ 4e\mathbf{A}\operatorname{Re}\big\{ih(\epsilon)f(\epsilon)f^*(-\epsilon)\big\}\Big].\end{aligned} \tag{1.5.21}$$

# Chapter 2

# Analytical solution

As the linearized Usadel equation is a scalar partial differential equation it should be possible to solve analytically, at least for some geometries and applied magnetic fields. In this chapter, we will study one such geometry consisting of a cylindrical normal metal surrounded by a superconductor and solve the Usadel equation in the normal metal. We start by finding these analytical solutions in the normal metal in Sec. 2.1 and then in Sec. 2.2 we study the screening currents in the normal metal when driven out of equilibrium. The entirety of this chapter is taken directly from the specialization project [40].

## 2.1 Cylindrical geometry

### 2.1.1 Physical system

While the linearized Usadel equation (1.5.12) is a big simplification when compared to the Usadel equation (1.4.34), it is still hard to solve in general. To simplify, we will now consider a cylindrically symmetric geometry, where we assume that we have a cylindrical normal metal of radius $R$ surrounded by a superconductor. We further assume that the sample is thinner than the inelastic scattering length so that the distribution function $h(\epsilon)$ does not depend on the $z$-coordinate. For quasiclassical theory to be applicable, we assume that the system is much larger than the Fermi wavelength, and to be able to use the Usadel equation we assume that the system is much larger than the elastic scattering length. Finally, we assume that the superconductor is thicker than the magnetic penetration and coherence length in all directions, which leads to flux quantization in the superconductor. When applying a magnetic field we will assume that it is constant in the normal metal and zero inside the superconductor. This is due to the fact that we have weakly induced superconductivity in the normal metal, which means that the screening currents it sets up are weak. In contrast, the superconductor has strong screening currents so we assume perfect screening. This will give an effective one-dimensional problem where we can solve the linearized Usadel equation analytically for some applied external fields. Due to this symmetry, we expect a solution that is cylindrically symmetric around the middle of the cylinder where we choose $r = 0$. The setup is shown in Fig. 2.1.

Due to the cylindrical symmetry of the problem, we now perform a change of variables to cylindrical coordinates, such that $\mathbf{r} = (r, \phi, z)$. This will also change the form of the derivatives when compared to Cartesian coordinates. The gradient becomes [60]

$$\nabla = \partial_r \hat{\mathbf{r}} + \frac{1}{r}\partial_\phi \hat{\boldsymbol{\phi}} + \partial_z \hat{\mathbf{z}}. \tag{2.1.1}$$

We also need the expression for the Laplacian which is

$$\nabla^2 f = \frac{1}{r}\partial_r(r\partial_r f) + \frac{1}{r^2}\partial_\phi^2 f + \partial_z^2 f. \tag{2.1.2}$$

Now the linearized Usadel equation (1.5.12) can be written

$$\frac{1}{r}\partial_r(r\partial_r f) + \frac{1}{r^2}\partial_\phi^2 f + \partial_z^2 f - 4ie(A_r\partial_r f + \frac{A_\phi}{r}\partial_\phi f + A_z\partial_z f) - 4e^2\mathbf{A}^2 f = -2i\frac{\epsilon}{D}f. \tag{2.1.3}$$

We can also rewrite the expression for the supercurrent (1.5.20) as

$$\begin{aligned}\mathbf{J}_e = \frac{1}{4}eN_f D\int_{-w_c}^{w_c} d\epsilon \Big[ &\mathrm{Re}\Big\{h(\epsilon)\Big[f(\epsilon)\big\{\partial_r f^*(-\epsilon)\hat{\mathbf{r}} + \frac{1}{r}\partial_\phi f^*(-\epsilon)\hat{\boldsymbol{\phi}} + \partial_z f^*(-\epsilon)\hat{\mathbf{z}}\big\} \\ &- f(-\epsilon)\big\{\partial_r f^*(\epsilon)\hat{\mathbf{r}} + \frac{1}{r}\partial_\phi f^*(\epsilon)\hat{\boldsymbol{\phi}} + \partial_z f^*(\epsilon)\hat{\mathbf{z}}\big\}\Big]\Big\} \\ &+ 4e\mathbf{A}\mathrm{Re}\Big\{ih(\epsilon)f(\epsilon)f^*(-\epsilon)\Big\}\Big].\end{aligned} \tag{2.1.4}$$

Since the system we are looking at is very thin in the $z$-direction we assume that $f$ does not depend on $z$. In addition, the cylindrical symmetry of the system means that we

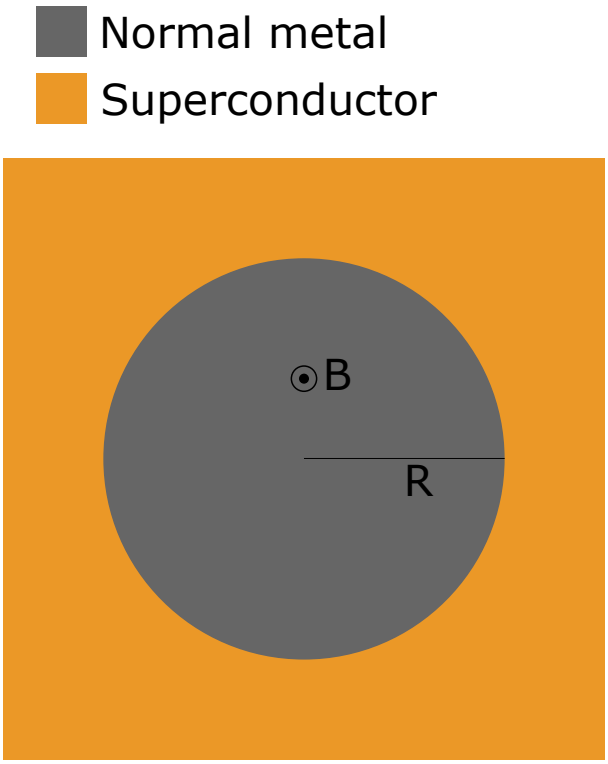


Figure 2.1: The geometry of the problem studied with a normal metal of radius $R$ surrounded by a superconducting material. The magnetic field points in the $z$-direction out of the plane. The superconductor is much larger than shown in this figure.

assume that $f$ has the form

$$f(\mathbf{r},\epsilon) = f(r,\epsilon)\exp(in\phi), \tag{2.1.5}$$

where $n$ is the winding number. The factor $\exp(in\phi)$ means that we have assumed a phase winding of $2\pi n$ in the superconducting order parameter when going around the cylinder once. When $n \neq 0$ this means that we have a system with a superconducting vortex[1]. To have $f(\mathbf{r},\epsilon)$ be well defined in the origin we also need that $f(r=0,\epsilon)=0$. This allows us to simplify Eqs. (2.1.3) and (2.1.4),

$$\begin{aligned}&\frac{1}{r}\partial_r\left[r\partial_r f(r,\epsilon)\right] - \frac{n^2}{r^2}f(r,\epsilon) - 4ie\left[A_r\partial_r f(r,\epsilon) + in\frac{A_\phi}{r}f(r,\epsilon)\right] - 4e^2\mathbf{A}^2 f(r,\epsilon)\\ &= -2i\frac{\epsilon}{D}f(r,\epsilon).\end{aligned} \tag{2.1.6}$$

Note that the factor $\exp(in\phi)$ is common to all terms in the equation and thus drops out after doing the $\phi$ derivatives. Equation (2.1.4) becomes:

$$\begin{aligned}\mathbf{J}_e = \frac{1}{4}eN_f D\int_{-w_c}^{w_c} d\epsilon\Big[&\mathrm{Re}\Big\{h(\epsilon)\big[f(r,\epsilon)\{\partial_r f^*(r,-\epsilon)\hat{\mathbf{r}} + \frac{-in}{r}f^*(r,-\epsilon)\hat{\boldsymbol{\phi}}\}\\ &- f(r,-\epsilon)\{\partial_r f^*(r,\epsilon)\hat{\mathbf{r}} + \frac{-in}{r}f^*(r,\epsilon)\hat{\boldsymbol{\phi}}\}\big]\Big\}\\ &+ 4e\mathbf{A}\mathrm{Re}\Big\{ih(\epsilon)f(r,\epsilon)f^*(r,-\epsilon)\Big\}\Big].\end{aligned} \tag{2.1.7}$$

Here every term $f$ is multiplied by its complex conjugate $f^*$ so the term $\exp(in\phi)$ also drops from this equation after doing the derivatives.

We can now specialize this to the equilibrium and non-equilibrium case at zero temperature $T=0$. If we only consider the integrand of Eq. (2.1.7) at $T=0$ we have

$$\begin{aligned}\mathrm{Re}\Big\{h(\epsilon)\big[&(4ie\mathbf{A} - 2\frac{in}{r})f(r,\epsilon)f^*(r,-\epsilon)\hat{\boldsymbol{\phi}}\\ &+ \{f(r,\epsilon)\partial_r f^*(r,-\epsilon) - f(r,-\epsilon)\partial_r f^*(r,\epsilon)\}\hat{\mathbf{r}}\big]\Big\}.\end{aligned} \tag{2.1.8}$$

If we now make the change $\epsilon \to -\epsilon$ we just get a sign change from the $f$ part and a sign change within the argument of $h$,

$$\begin{aligned}\mathrm{Re}\Big\{-h(-\epsilon)\big[&(2ie\mathbf{A} - \frac{in}{r})f(r,\epsilon)f^*(r,-\epsilon)\hat{\boldsymbol{\phi}}\\ &+ \{f(r,\epsilon)\partial_r f^*(r,-\epsilon) - f(r,-\epsilon)\partial_r f^*(r,\epsilon)\}\hat{\mathbf{r}}\big]\Big\}.\end{aligned} \tag{2.1.9}$$

Looking at the equilibrium case where $h$ is given by Eq. (1.2.53) it is also antisymmetric in $\epsilon$, so the integrand is symmetric in $\epsilon$ and we get for the supercurrent

[1]For $n<0$ we would get a winding in the opposite way of a normal vortex. This is what is known as an anti-vortex and has currents circulating in the opposite direction of a normal vortex [26].

$$\mathbf{J}_e = \frac{1}{2} eN_f D \int_0^{w_c} d\epsilon \left[ \mathrm{Re}\Big\{ (2ie\mathbf{A} - \frac{in}{r}) f(r,\epsilon) f^*(r,-\epsilon) \hat{\boldsymbol{\phi}} + \big[ f(r,\epsilon)\partial_r f^*(r,-\epsilon) - f(r,-\epsilon)\partial_r f^*(r,\epsilon) \big] \hat{\mathbf{r}} \Big\} \right]. \tag{2.1.10}$$

If we instead consider a voltage applied as described in section 1.2.6, such that $h$ is given by Eq. (1.2.55), the integrand is 0 for $|\epsilon| < eV$ and symmetric for $|\epsilon| > eV$ resulting in a supercurrent

$$\mathbf{J}_e = \frac{1}{2} eN_f D \int_{eV}^{w_c} d\epsilon \left[ \mathrm{Re}\Big\{ (2ie\mathbf{A} - \frac{in}{r}) f(r,\epsilon) f^*(r,-\epsilon) \hat{\boldsymbol{\phi}} + \big[ f(r,\epsilon)\partial_r f^*(r,-\epsilon) - f(r,-\epsilon)\partial_r f^*(r,\epsilon) \big] \hat{\mathbf{r}} \Big\} \right]. \tag{2.1.11}$$

Note that for the equilibrium case, $eV = 0$, this is equal to Eq. (2.1.10) so that we can in general use Eq. (2.1.11) to describe both the equilibrium and non-equilibrium case. This leads to a current density on the form

$$\mathbf{J}_e = \frac{1}{2} eN_f D \int_{eV}^{w_c} d\epsilon \left[ \mathrm{Re}\Big\{ 2(2ie\mathbf{A} - \frac{in}{r}) f(r,\epsilon) f^*(r,-\epsilon) \hat{\boldsymbol{\phi}} + \big[ f(r,\epsilon)\partial_r f^*(r,-\epsilon) - f(r,-\epsilon)\partial_r f^*(r,\epsilon) \big] \hat{\mathbf{r}} \Big\} \right]. \tag{2.1.12}$$

This is then the form of the supercurrent density when we are in the weak proximity regime in the normal metal cylinder, where we assume cylindrical symmetry and use the ansatz in Eq. (2.1.5). When we specify the form of $A$ and find an expression for $f$ from solving the linearized Usadel equation (2.1.6) we can just plug them into this equation and find the supercurrent density in the normal metal. The $\hat{\boldsymbol{\phi}}$ term is the azimuthal current which will give the screening currents inside the normal metal, and it will be finite when we consider a vortex. The $\hat{\mathbf{r}}$ term corresponds to a radial current. One would expect from the geometry we study that we should not have a radial current and we will later show that this is in fact the case.

### 2.1.2 Boundary conditions

As the linearized Usadel equation (2.1.6) is a second-order differential equation we need two boundary conditions to fully solve it. The first boundary condition is in the middle of the vortex at $r = 0$. We assume that the superconductivity is completely destroyed at $r = 0$ and $f(\mathbf{r}, \epsilon)$ should be single-valued so it must disappear at $r = 0$ due to the freedom to choose the angle $\phi$, and thus we set

$$f(r = 0, \epsilon) = 0, \tag{2.1.13}$$

which is obviously a solution to equation (2.1.6). The second boundary condition is found using Kuprianov-Lukichev boundary condition [61] for the normal metal-superconductor

interface at $r = R$. According to F. S. Bergeret et al. [56], for the linearized Usadel equation in the absence of spin-flipping processes at the interface, the Kuprianov-Lukichev boundary condition reduces to

$$\gamma \partial_r f(R, \epsilon) = -f_{\text{BCS}} = -\sinh\left[\operatorname{artanh}\left(\frac{\Delta}{\epsilon}\right)\right]. \tag{2.1.14}$$

Here $f_{BCS}$ is the value of $f$ inside the superconductor, $\Delta$ is the superconducting gap and $\gamma = R_b \sigma_F$ is a measure of the interface resistance where $R_b$ is the boundary resistance per unit area and $\sigma_N$ is the conductivity of the normal metal region. To get this expression we have neglected inverse proximity effects, i.e., the weakening of the superconductivity inside the superconductor since we have a resistive interface. As we assumed that the superconducting order parameter has a phase in Eq. (2.1.5), this also means that there should be a matching of the phases of $f$ and $f_{\text{BCS}}$ at the interface, but we have already done this by the addition of the phase in Eq. (2.1.5).

### 2.1.3 Without magnetic field

The simplest instance to solve the linearized Usadel equation in our system (2.1.6) is when $\mathbf{A} = 0$. This is equivalent to having no magnetic field, $\mathbf{B} = 0$. When we have a superconducting vortex without a magnetic field they are usually referred to as Josephson vortices. The Josephson vortices can be made by for instance passing a current through a superconductor on two sides of a normal metal as shown by D. Roditchev et al. [23] or by passing a current through a superconductor surrounding a normal metal as shown by M. Amundsen et al. [26]. When we apply the currents, we create a phase winding of $2\pi n$ inside the superconductor which gives rise to the vortex inside the normal metal. This vortex appears due to the circulation of current there needs to be one point where there is no current flowing and thus no superconductivity, which is the center of the vortex. This is different from an Abrikosov vortex where the vortices are made to allow magnetic flux to penetrate the superconductor in a small area where the superconductivity is destroyed and currents flow around this area to shield the rest of the superconductor from the magnetic field. In the case we are studying here, the linearized Usadel equation with $\mathbf{A} = 0$ becomes:

$$\frac{1}{r}\partial_r(r\partial_r f(r, \epsilon)) = \left(\frac{n^2}{r^2} - 2i\frac{\epsilon}{D}\right) f(r, \epsilon), \tag{2.1.15}$$

which has solution

$$f(r, \epsilon) = c_1 J_n\left(\sqrt{2i\frac{\epsilon}{D}}r\right) + c_2 Y_n\left(\sqrt{2i\frac{\epsilon}{D}}r\right). \tag{2.1.16}$$

Here $J_n$ are Bessel's functions of the first kind given by [60]

$$J_n(x) = \sum_{k=0}^{\infty} \frac{(-1)^k}{k!\Gamma(k+n+1)}\left(\frac{x}{2}\right)^{2k+n}, \tag{2.1.17}$$

and $Y_n$ are Bessel's functions of the second kind given by [60]

$$Y_\alpha(x) = \frac{J_\alpha(x)\cos(\alpha\pi) - J_{-\alpha}(x)}{\sin(\alpha\pi)}, \tag{2.1.18}$$

and the limit $\alpha \to n$ should be taken for integer values of $\alpha$.

Most superconducting vortices have a winding number $n = 1$ as the energy of a vortex increases as $n^2$. This means it is energetically favourable to split vortices, but we can still get higher winding numbers due to discrete symmetries [26]. Thus, we will consider the $n = 1$ case. In this case, $Y_1(r)$ diverges as $r \to 0$. However, we know that $f(r, \epsilon)$ is related to both the pair correlation function and supercurrent, and neither of them diverge as $r \to 0$. Instead, we use the boundary condition in Eq. (2.1.13) to set $c_2 = 0$. This gives the solution

$$f(r,\epsilon) = c_1 J_1\left(\sqrt{2i\frac{\epsilon}{D}}r\right) = c_1 \sum_{k=0}^{\infty} \frac{(-1)^k}{k!(k+1)!}\left(\sqrt{\frac{i}{2}\frac{\epsilon}{D}}r\right)^{2k+1}. \tag{2.1.19}$$

To determine $c_1$ we use Kuprianov-Lukichev boundary conditions (2.1.14):

$$c_1 = -\sqrt{2\frac{D}{i\epsilon}}\frac{\sinh\left[\operatorname{artanh}(\Delta/\epsilon)\right]}{\left[J_0(\sqrt{2i\epsilon/D}R) - J_2(\sqrt{2i\epsilon/D}R)\right]}. \tag{2.1.20}$$

Here the terms $J_0$ and $J_2$ come from the identity $2\partial_x J_n(x) = J_{n-1}(x) - J_{n+1}(x)$. Inserting this back into (2.1.19) gives us the solution

$$f(r,\epsilon) = -\sqrt{\frac{D}{i\epsilon}}\sinh\left[\operatorname{artanh}\left(\frac{\Delta}{\epsilon}\right)\right]\frac{J_1(\sqrt{2i\epsilon/D}r)}{\left[J_0(\sqrt{2i\epsilon/D}R) - J_2(\sqrt{2i\epsilon D}R)\right]}. \tag{2.1.21}$$

Letting $\epsilon \to -\epsilon$ and taking the complex conjugate we can find an expression for $\tilde{f}$. We also notice from Eq. (2.1.17) that taking the complex conjugate of a Bessel function is the same as taking the complex conjugate of the argument:

$$\tilde{f}(r,\epsilon) = -\sqrt{\frac{D}{i\epsilon}}\left\{-\sinh\left[\operatorname{artanh}\left(\frac{\Delta}{\epsilon}\right)\right]\right\}^* \frac{J_1(\sqrt{2i\epsilon D}r)}{\left[J_0(\sqrt{2i\epsilon/D}R) - J_2(\sqrt{2i\epsilon/D}R)\right]}. \tag{2.1.22}$$

As $\sinh\left[\operatorname{artanh}(\Delta/\epsilon)\right]$ is real for $\epsilon > \Delta$ we then have $\tilde{f} = -f$ while it is imaginary for $\epsilon < \Delta$ which then gives $\tilde{f} = f$ due to the complex conjugation. Let us now consider the product $f(r,\epsilon)f^*(r,-\epsilon)$:

$$f(r,\epsilon)f^*(r,-\epsilon) = i\frac{D}{\epsilon}\left|\sinh\left[\operatorname{artanh}\left(\frac{\Delta}{\epsilon}\right)\right]\right|^2\left\{\frac{J_1(\sqrt{2i\epsilon D}r)}{\left[J_0(\sqrt{2i\epsilon/D}R) - J_2(\sqrt{2i\epsilon/D}R)\right]}\right\}^2. \tag{2.1.23}$$

Since the Bessel functions are complex with the given arguments we see that this is complex, and this will thus contribute to the supercurrent density when multiplying with $i$ and taking the real part in Eq. (2.1.12). Next consider the term $f(r,\epsilon)\partial_r f^*(r,-\epsilon) - f(r,-\epsilon)\partial_r f^*(r,\epsilon)$. We use that $\tilde{f}(r,\epsilon) = f^*(r,-\epsilon) = \pm f(r,\epsilon)$ where the sign is positive for $|\epsilon| < \Delta$ and negative for $|\epsilon| > \Delta$ as seen from comparing Eqs. (2.1.21) and (2.1.22):

$$\begin{aligned} f(r,\epsilon)\partial_r f^*(r,-\epsilon) - f(r,-\epsilon)\partial_r f^*(r,\epsilon) &= f(r,\epsilon)\partial_r f^*(r,-\epsilon) - \left[f^*(r,-\epsilon)\partial_r f(r,\epsilon)\right]^* \\ &= \pm\left\{f(r,\epsilon)\partial_r f(r,\epsilon) - \left[f(r,\epsilon)\partial_r f(r,\epsilon)\right]^*\right\}. \end{aligned} \tag{2.1.24}$$

We recognize the second line as being on the form $\pm(a-a^*)$ so this is purely imaginary. Thus, when we calculate the radial current and take the real part, this term drops out and we get no radial current. This is as expected since we have no sources or drains and thus a radial current would lead to a buildup or deficit of charge which is not possible since we have assumed a time-independent solution.

Finally, we will consider the supercurrent density very near the vortex core, $r \ll \xi$. Here we only keep the term in $J_1$ linear in $r$ in Eq. (2.1.23) to get:

$$f(r,\epsilon)f^*(r,-\epsilon) \approx i\frac{D}{\epsilon}\left|\sinh\left[\operatorname{artanh}(\frac{\Delta}{\epsilon})\right]\right|^2 \frac{(2i\epsilon/Dr^2)}{\left[J_0(\sqrt{2i\epsilon/D}R) - J_2(\sqrt{2i\epsilon/D}R)\right]^2}. \quad (2.1.25)$$

Inserting this into the expression for the supercurrent (2.1.12) and setting $\mathbf{A} = 0$ and $n = 1$ gives:

$$\mathbf{J}_e \approx 2eN_f Dr \int_{eV}^{w_c} d\epsilon\, Re\left\{ i\left|\sinh\left[\operatorname{artanh}(\frac{\Delta}{\epsilon})\right]\right|^2 \frac{1}{\left[J_0(\sqrt{2i\epsilon/D}R) - J_2(\sqrt{2i\epsilon/D}R)\right]^2}\right\}\hat{\boldsymbol{\phi}}. \quad (2.1.26)$$

Thus we have found an analytic expression for the current close to the vortex core for a Josephson vortex in a proximitized normal metal that is applicable both in and out of equilibrium. We note that this is linear in $r$, thus the current will go to 0 as $r \to 0$ in a linear manner. This expression can be used in the setup described by M. Amundsen et al. [26] where the vortices are created while $\mathbf{A} = 0$ due to circulating currents. Since they considered thin films the currents are so weak that they create a negligible magnetic field.

### 2.1.4 With magnetic field

Let us again look at the linearized Usadel equation (2.1.6) but this time include a magnetic field $\mathbf{B}$, which implies that $\mathbf{A} \neq 0$. Instead, we now consider a vortex created by a magnetic field. Consider a geometry where we have a cylindrical normal metal of radius $R$ surrounded by a superconductor as shown in Fig. 2.1. This will be similar to an Abrikosov vortex in a type II superconductor, but not exactly the same as we are considering a proximitized normal metal. We approximate the magnetic field as

$$\mathbf{B}(\mathbf{r}) = \frac{\Phi}{\pi R^2}\hat{\mathbf{z}} \quad r < R, \quad (2.1.27)$$

$$\mathbf{B}(\mathbf{r}) = 0 \quad r > R. \quad (2.1.28)$$

Thus, all of the magnetic field is inside the vortex and is approximately constant within it. This is due to the fact that we assume weak proximity-induced superconductivity because of the resistive barrier between the normal metal and superconductor. As a result, the screening currents are weak and this is all consistent with using the linearized Usadel equation inside the normal metal. Inside the superconductor, the magnetic field is zero since we assume that the superconductor has perfect screening for simplicity, i.e., only an infinitely thin layer around the superconductor has circulating currents. Outside of this layer the phase winding of the superconductor and the choice of vector potential will

cancel out so there are no circulating currents. To find a suitable vector potential $\mathbf{A}$ we use

$$\mathbf{B}(\mathbf{r}) = \nabla \times \mathbf{A} = (\frac{1}{r}\partial_\phi A_z - \partial_z A_\phi)\hat{\mathbf{r}} + (\partial_z A_r - \partial_r A_z)\hat{\boldsymbol{\phi}} + \frac{1}{r}(\partial_r(rA_\phi) - \partial_\phi A_z)\hat{\mathbf{z}}. \quad (2.1.29)$$

Using this equation we see that a possible choice of $\mathbf{A}$ is

$$\mathbf{A}(\mathbf{r}) = \frac{\Phi r}{2\pi R^2}\hat{\boldsymbol{\phi}} \quad r < R, \quad (2.1.30)$$

$$\mathbf{A}(\mathbf{r}) = \frac{\Phi}{2\pi r}\hat{\boldsymbol{\phi}} \quad r > R. \quad (2.1.31)$$

The choice for $r > R$ is natural as the line integral of $\mathbf{A}$ around a closed curve $l$ is the same as the magnetic flux through that surface $\Sigma$ enclosed by $l$. Using Faraday's law and Stoke's theorem we have

$$\Phi_B = \iint_\Sigma \mathbf{B}\cdot\hat{\mathbf{n}}\,\mathrm{d}\Sigma = \oint_l \mathbf{A}\cdot\mathrm{d}l. \quad (2.1.32)$$

For a circle at radius $r$ we get

$$\Phi_B = \int_0^{2\pi} \frac{\Phi}{2\pi r} r\mathrm{d}\phi = \Phi. \quad (2.1.33)$$

No matter how large we make $r$, as long as we have $r > R$ we enclose the same flux which fits correctly with our choice of $\mathbf{B}(\mathbf{r})$.

In the case $r < R$ the linearized Usadel equation (2.1.6) becomes

$$\frac{1}{r}\partial_r(r\partial_r f(r,\epsilon)) - \frac{n^2}{r^2}f(r,\epsilon) + 2en\frac{\Phi}{\pi R^2}f(r,\epsilon) - e^2\left(\frac{\Phi r}{\pi R^2}\right)^2 f(r,\epsilon) = -2i\frac{\epsilon}{D}f(r,\epsilon). \quad (2.1.34)$$

To simplify this equation we can make use of the fact that flux quantization leads to

$$\Phi = \frac{n\hbar\pi}{e} = \frac{n\pi}{e}, \quad (2.1.35)$$

where $n$ is an integer, such that we can write Eq. (2.1.34) as

$$\frac{1}{r}\partial_r(r\partial_r f(r,\epsilon)) - \frac{n^2}{r^2}f(r,\epsilon) + \frac{2n^2}{R^2}f(r,\epsilon) - \frac{n^2r^2}{R^4}f(r,\epsilon) = -2i\frac{\epsilon}{D}f(r,\epsilon). \quad (2.1.36)$$

This has solution

$$\begin{aligned} f(r,\epsilon) = e^{-\frac{n}{2}\frac{r^2}{R^2}} r^n \Bigg[ & c_1 U\left(\frac{1}{2} - i\frac{\epsilon R^2}{2nD}, 1+n, n\frac{r^2}{R^2}\right) \\ & + c_2 L\left(-\frac{1}{2} + i\frac{\epsilon R^2}{2nD}, n, n\frac{r^2}{R^2}\right)\Bigg], \end{aligned} \quad (2.1.37)$$

where $U(a,b,z)$ is the confluent hypergeometric function and $L(a,b,z)$ is the Laguerre function [60]. As $U(a,b,z)$ has a branch cut in the complex $z$-plane for $\mathrm{Re}(z) \in (-\infty, 0]$ we use Eq. (2.1.13) to set $c_1 = 0$ and we get

$$f(r,\epsilon) = ce^{-\frac{n}{2}\frac{r^2}{R^2}} r^n L\left(-\frac{1}{2} + i\frac{\epsilon R^2}{2nD}, n, n\frac{r^2}{R^2}\right). \quad (2.1.38)$$

We now use the boundary condition at $r = R$, given in Eq. (2.1.14), to find $c$:

$$c = \frac{\sinh\left[\operatorname{artanh}\left(\frac{\Delta}{\epsilon}\right)\right]}{2\gamma R^{n-1} e^{-\frac{n}{2}} L\left(-\frac{3}{2} + i\frac{\epsilon R^2}{2nD}, n+1, n\right)}. \tag{2.1.39}$$

This finally lets us give the solution for $f$ as

$$f(r,\epsilon) = \frac{\sinh\left[\operatorname{artanh}\left(\frac{\Delta}{\epsilon}\right)\right]}{2\gamma} e^{\frac{n}{2}\left(1-\frac{r^2}{R^2}\right)} \frac{r^n}{R^{n-1}} \frac{L\left(-\frac{1}{2} + i\frac{\epsilon R^2}{2nD}, n, n\frac{r^2}{R^2}\right)}{L\left(-\frac{3}{2} + i\frac{\epsilon R^2}{2nD}, n+1, n\right)}. \tag{2.1.40}$$

Just as for the case $\mathbf{A} = 0$ we have $\tilde{f} = f$ for $|\epsilon| < \Delta$ and $\tilde{f} = -f$ for $|\epsilon| > \Delta$. Thus, according to Eq. (2.1.24) we have zero radial currents which is what we expect from the symmetries of the geometry.

## 2.2 Results for cylindrical geometry

From the solution $f(r, \epsilon)$ in Eq. (2.1.40) we can calculate the current density in the normal metal using Eq. (2.1.7). However, due to the highly non-trivial dependence on $\epsilon$ in $f(r, \epsilon)$, all integrals have been performed numerically. We will also consider the $T = 0$ limit and both equilibrium and non-equilibrium situations with an applied voltage $eV$ applied in such a way as to lead to a two-step distribution function as described in section 1.2.6. This means that the current density is found using Eq. (2.1.12). As we have shown for both cases we studied in chapter 2.1 there is no radial current. Thus we will in this chapter only consider the azimuthal current. In addition, we will from here on focus on the conventional case of vortices created by applying a magnetic field, as derived in section 2.1.4.

When doing the numerical integrals it was assumed that we had a vortex with winding number $n = 1$. Values for $\epsilon$ and $r$ were normalized with regard to the superconductor. Thus, we let $\epsilon \to \epsilon/\Delta$ and $r \to r/\xi$ to make the Usadel equation dimensionless and numerically set $\Delta = 1$ and $\xi = 1$. From the definition of the coherence length $\xi = \sqrt{D/\Delta}$ we then get $D = \Delta\xi^2 = 1$. For $\gamma$ we chose a moderate interface transparency $\gamma = 3\xi$. We also need a cutoff frequency for the integral and it was chosen as $w_c = 30\Delta$, but a lower $w_c$ should also be sufficient as almost all of the contributions are from $\epsilon \in [0, 2\Delta]$, as can be seen from Fig. 2.2. In addition, a small imaginary part was added to the energy in $f(\epsilon)$, i.e., we let $\epsilon \to \epsilon + 0.01i$. This was not done for $h(\epsilon)$, but it should be noted that for the zero temperature case, adding an imaginary part to the energy does not affect $h(\epsilon)$, it still remains a two-step function. Adding this imaginary part had two reasons behind it. Firstly, this matches closely to what is measured in experiments by R. C. Dynes et al. [62]. Secondly, it improves the stability in the numerical integration and circumvents the divergence at $\epsilon = \Delta$ for purely real energies.

First, we look at the spectral current density, i.e., the integrand of Eq. (2.1.12). It should be noted that in all plots we divide by the electron charge. As this is negative the actual currents get a sign change compared to what is shown in the plots. Figure 2.2 shows how the spectral current density depends on both $r$ and $\epsilon$. We see that for small radii $R$ of the normal metal, for example, $R = 0.5\xi$ and $R = \xi$, it is negative for all values of $\epsilon$ and $r$. Thus, no matter what non-equilibrium distribution function we enforce through a voltage the current will still be screening the magnetic field. If we instead look at larger radii, $R = 2\xi$ and $R = 3\xi$, we observe that it is still negative for $\epsilon$ close to 0. However, for $\epsilon$ close to $\Delta$ we see that the current in the material depends on the radius. The positive contributing area is larger than the negative one, and this difference increases for larger radii. As we have shown in section 2.1.1, when we apply a voltage $eV$ we block modes with energy $\epsilon < eV$. This means that if we apply a voltage, we should for some value of $eV$ between 0 and $\Delta$ observe a reversal of the screening current for some regions of the normal metal for $R = 2\xi$ and $R = 3\xi$. Reversing parts of the screening currents means that these parts increase the magnetic field instead of screening it. Thus, more of the magnetic field will have to be shielded by the superconductor. In the calculations we have for simplicity assumed that we have perfect screening at the interface. In practice, some magnetic flux will leak into the superconductor and thus the screening currents in the superconductor will be distributed in a finite region close to the interface. As we get an increase in the amount of magnetic field leaking into the superconductor, we also

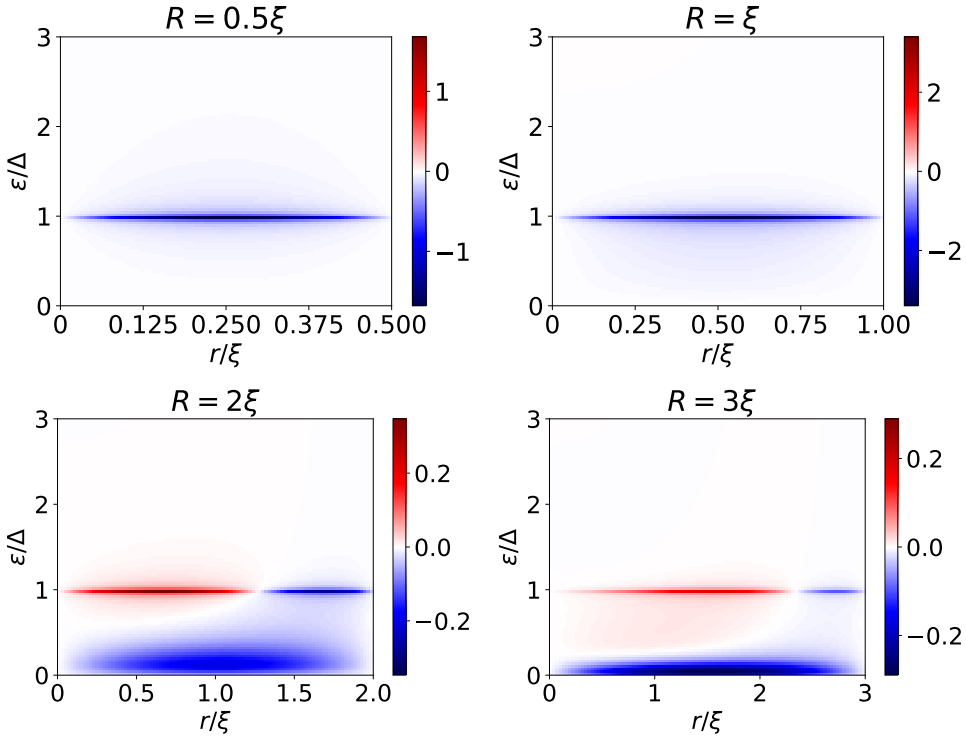


Figure 2.2: Colorplots of azimuthal component of the spectral current density $J_{e,\phi}(r,\epsilon)/(eN_f\, D\Delta/\xi)$ as a function of $r$ and $\epsilon$ for various radii $R$ of the normal metal. The blue regions denote conventional diamagnetic screening currents while the red regions denote paramagnetic contributions. By applying a voltage to create a two-step non-equilibrium distribution function, modes can be blocked with increasing energy $\epsilon$. For $R = 2\xi$ and $R = 3\xi$ one can thus tune the normal metal from a net diamagnetic response to a net paramagnetic response.

need a larger area with screening currents, thus the size of the vortex should increase. In addition, the amount of magnetic field that passes through the normal metal and superconductor combined is quantized, so the increase in the size of the vortex should decrease the magnetic field density of the vortex.

This view becomes clearer if we look at Figs. 2.3 and 2.4 which show the current density for $R = 3\xi$ for different applied voltages $eV$. We see that for no applied voltage, the current is negative for the entire cylinder thus screening the magnetic field a bit. If we focus on the case for $eV = 0.18\Delta$ we have zero total current if we also integrate over $r$. This might not be clear from Fig. 2.3 since it does not include the fact that when integrating over $r$ we should also multiply by the factor $2\pi r$ since we are working in cylindrical coordinates. If we instead focus on $eV = 0.18\Delta$ in Fig. 2.4 we clearly see that the negative and positive contributions cancel out. If we compare this to the case for $eV = 0.5\Delta$ we see that in this case the area that gives positive current is increased while the area that gives negative current is decreased. Thus the total current will be circulating in the opposite direction as compared to the case for $eV = 0$. One should also note that the magnitude of the current is much smaller in the case when $eV = 0.5\Delta$ as compared to $eV = 0$. The magnitude of the maximum current density is much smaller for $eV = 0.5\Delta$ and the negative contributions for $r$ close to $R$ will partly cancel the positive

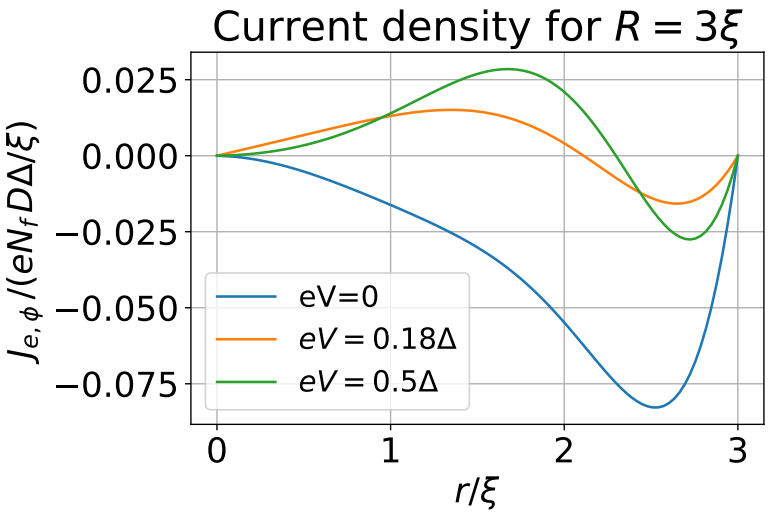


Figure 2.3: Azimuthal current density $J_{e,\phi}(r)/(eN_f\, D\Delta/\xi)$ for radius $R = 3\xi$ and different values of the applied voltage. $eV = 0.18\Delta$ is chosen as it gives zero total current. We see that for $r$ closer to the center of the cylinder we switch from a diamagnetic to a paramagnetic response when applying a voltage, while for $r$ close to the interface at $R$ the response stays diamagnetic.

contributions for smaller $r$. Thus the change of the magnetic field due to the screening currents in the normal metal will be much smaller when applying a voltage as compared to no applied voltage.

We can also see the smaller magnitude of the reversed currents due to an applied voltage in Fig. 2.5. It shows the total current $I_{e,\phi} = 2\pi \int \mathrm{d}r\, r J_{e,\phi}(r)$ for different applied voltages. If we apply no voltage we have the largest screening current but as we increase the voltage the current changes differently depending on $R$. For $R < \xi$ we see basically no change, which is what is expected from Fig. 2.2 as the spectral current density peaks quite sharply at an energy $\epsilon \approx \Delta$ and thus blocking the modes with energy $\epsilon < 0.5\Delta$ has little effect. However, for larger $R$ we see a clear difference when applying a voltage and for large enough radii we reverse the current, thus changing from a net diamagnetic to a net paramagnetic response. The larger the radius is, the smaller the voltage needed for this reversal. For $R > 4\xi$ we also see that increasing the voltage from $eV = 0.2\Delta$ to $eV = 0.5\Delta$ actually decreases the current. This can be understood by the fact that for such large radii only the modes with energy very close to zero contribute to the screening current, whereas the rest contribute to the reversing. By increasing the voltage further than needed, many of the modes that would contribute to the reversing are blocked from contributing to the current so the total current becomes smaller.

Figure 2.6 shows the applied voltage needed to have zero total current $I$, where voltages larger than $eV = 2\Delta$ have not been included. One should note that the superconducting phase becomes unstable for applied voltages $eV > \Delta$ and bistable for $eV > 0.5\Delta$ [63]. Values between $eV = \Delta$ and $eV = 2\Delta$ have still been included to show that there is still a mathematical solution. Because of this bistability the region where $eV < 0.5\Delta$ is the most relevant for experiments. For a given $R$, any voltage above the line in the plot will lead to the total current being reversed while it will not for any lower voltage, thus we

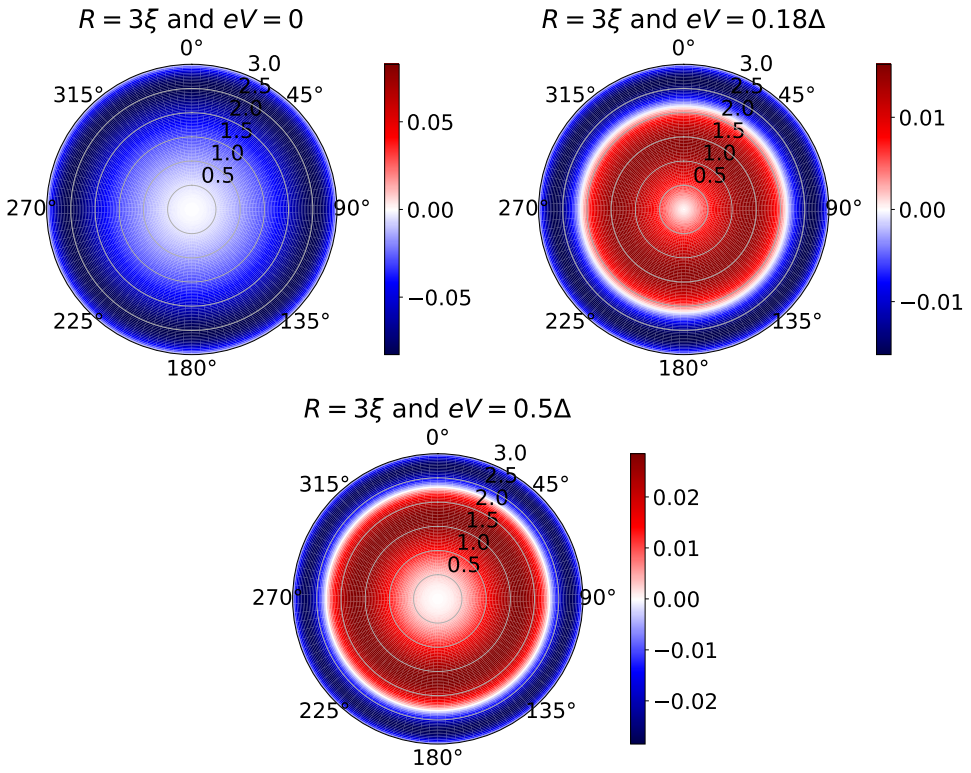


Figure 2.4: Polar plots of azimuthal current densities $J_{e,\phi}(r)/(eN_f\, D\Delta/\xi)$ for radius $R = 3\xi$, showing how the current is distributed within the cylinder for different applied voltages $eV$. We see that an increase in the applied voltage switches from a diamagnetic to a paramagnetic response near the core of the cylinder while near the edge of the cylinder the response is always diamagnetic.

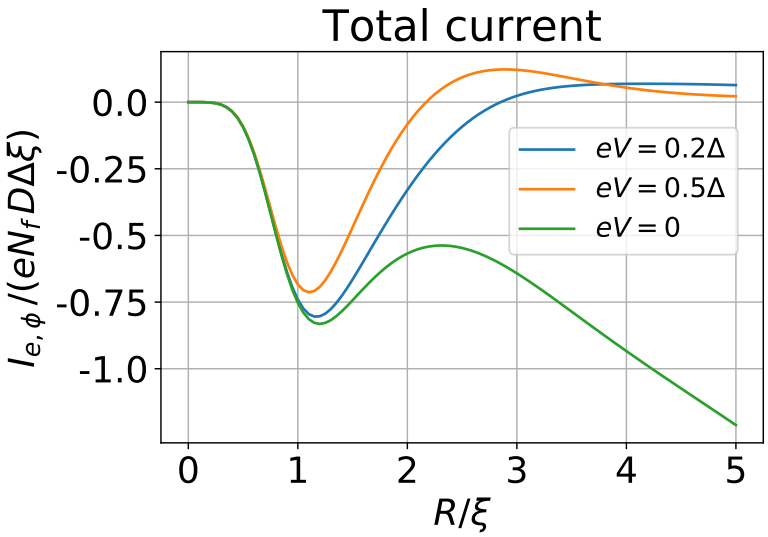


Figure 2.5: Total current $I_\phi//(eN_f\, D\Delta\xi)$ as a function of the radius $R$ of the normal metal cylinder for different applied voltages $eV$. The total response of the normal metal can be tuned from diamagnetic to paramagnetic by applying a voltage for $R > 2\xi$. The effect of applying a voltage is negligible for $R < 1$ due to the sharp peak of the spectral current at $\epsilon \approx \Delta$ at these radii. When increasing the radii past $R = \xi$ we start getting paramagnetic modes at $\epsilon \approx \Delta$ and diamagnetic modes at $\epsilon \approx 0$. Thus the total current decreases for a range $\xi \lesssim R \lesssim 2.5\xi$ and this is the same range where we start seeing an effect when applying a voltage.

call it the switching voltage $eV_s$. This again shows the clear trend that larger radii need a lower voltage to flip the current. We see that for values of $R$ just above $2\xi$ the switching voltage drops quite quickly and afterwards drops more slowly. This is because for $R \approx 2\xi$ we change from having a switching voltage $eV_s > \Delta$ to a switching voltage $eV_s < \Delta$. Thus, we start to include the relatively large contributions at $\epsilon \approx \Delta$ as seen in Fig. 2.2. We also see that we always need a finite switching voltage, which is due to the contributions with $\epsilon \approx 0$ which always dominate for no applied voltage.

To test the results found in this chapter experimentally, we propose a setup where one has a thin cylinder of normal metal surrounded by a large superconductor. An external magnetic field is applied and mainly penetrates the normal metal due to the Meissner effect. To drive the system out of equilibrium, we apply a voltage through an injector connected to the normal metal as explained by J. A. Ouassou et al. [39] which leads to a distribution function as described in section 1.2.6. The system is shown in Fig. 2.7. To measure the expected increase in the size of the vortex, one can use either scanning-tunnelling microscopy to measure the change in the density of states caused by the reduction of superconductivity, or magneto-optical imaging to measure the increase in the area where the magnetic field penetrates. Using magneto-optical imaging one could also measure the change in the magnetic field density one expects from the change in the distribution of the screening currents.

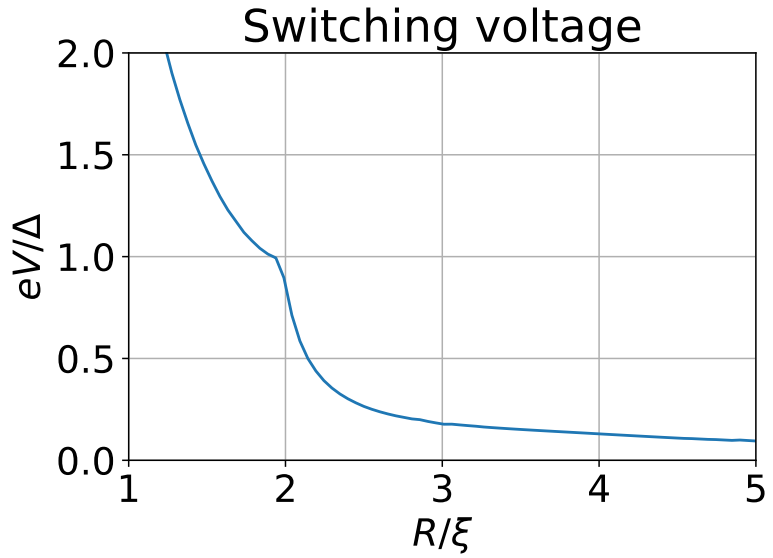


Figure 2.6: Switching voltage $eV_s/\Delta$ as a function of the radius $R$ of the normal metal. We define the switching voltage as the voltage when the net screening current changes from being diamagnetic to paramagnetic. This voltage decreases as we increase the radius of the normal metal.

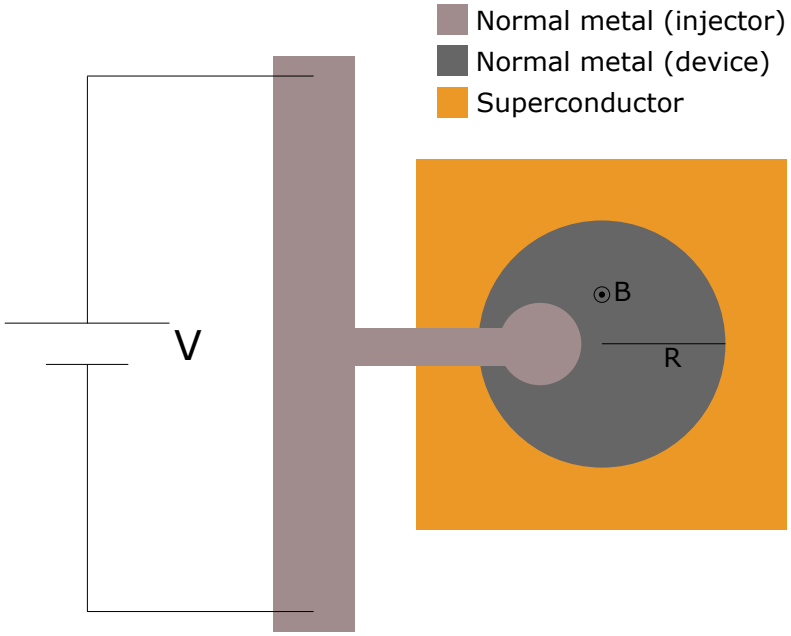


Figure 2.7: Suggested experimental setup. An external magnetic field is applied and the normal metal is subject to a voltage bias. In practice the superconductor should be much larger than shown here.

# Chapter 3

# Numerical solution

The cylindrical geometry studied in Ch. 2 is interesting because we could analytically solve the linearized Usadel equation, however, it is not the easiest setup to realize experimentally. We will from now on study square geometries due to their more realizable nature. However, as there is less symmetry in these cases it is harder to find an analytical solution so we will study them numerically. In addition, this allows us to use fewer approximations, such as more realistic magnetic field distributions which are not necessarily constant. We begin by explaining some general numerical tools used for these numerical simulations in Sec. 3.1. The full numerical implementation of solving the linearized Usadel equation in Python can be found on GitHub[1]. Then we continue with studying a square normal metal surrounded by a superconductor in Secs. 3.2 and 3.3 and finally we study a thin film of normal metal deposited on a bulk type-II superconductor in Secs. 3.4 and 3.5.

## 3.1 Numerical techniques

### 3.1.1 Finite difference method

One of the most intuitive ways to solve differential equations is by the finite difference approach. Here one discretizes the space one is considering and approximates the derivative by a difference of function values at neighbouring points. Let us assume that the continuous variable $x$ is discretized into a set of $N$ points, $x \in \{x_1, x_2, \dots x_N\}$, and that we have an equal spacing $h$ between points, i.e. $x_n = x_1 + (n-1)h$ and $x_{n+1} - x_n = h$. To derive a finite difference version of the derivative we first write out the Taylor expansion for two function values $f(x_{n+1})$ and $f(x_{n-1})$ around the point $x_n$:

$$\begin{aligned} f(x_{n+1}) &= f(x_n) + hf'(x_n) + \frac{h^2}{2}f''(x_n) + \frac{h^3}{3!}f'''(x_n) + \mathcal{O}(h^4), \\ f(x_{n-1}) &= f(x_n) - hf'(x_n) + \frac{h^2}{2}f''(x_n) - \frac{h^3}{3!}f'''(x_n) + \mathcal{O}(h^4). \end{aligned} \tag{3.1.1}$$

By truncating the expression above at order $h$, i.e. only including terms up to the first derivative and dividing by $h$ we can get the so-called forward and backward difference

[1] https://github.com/Havardfalch/MASTERTHESIS

approximations [64]

$$\begin{aligned} f'(x_n) &= \frac{f(x_{n+1}) - f(x_n)}{h} + \mathcal{O}(h), \\ f'(x_n) &= \frac{f(x_n) - f(x_{n-1})}{h} + \mathcal{O}(h). \end{aligned} \tag{3.1.2}$$

While these expressions are very simple, the error scales as $\mathcal{O}(h)$, which means we require a very short step length $h$ for the error to be small. This is, however, quite simple to improve. By subtracting the second line from the first line and dividing by $2h$, we get an expression for the derivative known as the central difference approximation [64]

$$f'(x_n) = \frac{f(x_{n+1}) - f(x_{n-1})}{2h} + \mathcal{O}(h^2). \tag{3.1.3}$$

Here we see that the error scales as $\mathcal{O}(h^2)$ as the terms containing the second derivative cancel. This means that the error decreases much faster as $h$ decreases compared to the forwards or backwards difference approximations in Eq. (3.1.2). We will therefore use the central difference approximation to calculate derivatives numerically.

To obtain a central finite difference approximation for the second derivative $f''(x_n)$ we sum the two lines in Eq. (3.1.1). The first- and third-order derivative terms then disappear, and dividing by $h^2$ we get

$$f''(x_n) = \frac{f(x_{n+1}) - 2f(x_n) + f(x_{n-1})}{h^2} + \mathcal{O}(h^2). \tag{3.1.4}$$

Using Eqs. (3.1.3) and (3.1.4) we can write the linearized Usadel equation (1.5.12) on finite difference form as

$$\begin{aligned} &f_{i+1,j}\left(\frac{1}{h_x^2} - 2ieA_{x,i,j}\frac{1}{h_x}\right) + f_{i-1,j}\left(\frac{1}{h_x^2} + 2ieA_{x,i,j}\frac{1}{h_x}\right) + f_{i,j+1}\left(\frac{1}{h_y^2} - 2ieA_{y,i,j}\frac{1}{h_y}\right) \\ &+ f_{i,j-1}\left(\frac{1}{h_y^2} + 2ieA_{y,i,j}\frac{1}{h_y}\right) = f_{i,j}\left(\frac{2}{h_x^2} + \frac{2}{h_y^2} + 4e^2\mathbf{A}_{i,j}^2 - 2i\frac{\epsilon}{D}\right), \end{aligned} \tag{3.1.5}$$

where $f_{i,j} = f(x_i, y_j)$ is the value of the Green's function at $(x_i, y_j)$, $A_{p,i,j} = A_p(x_i, y_j)$ is the $p$'th component of the magnetic vector potential at $(x_i, y_j)$, $\mathbf{A}_{i,j}^2 = |\mathbf{A}(x_i, y_j)|^2$ is the square of the magnetic vector potential at $(x_i, y_j)$, $h_x$ is the step length in the $x$-direction and $h_y$ is the step length in the $y$ direction. When the linearized Usadel equation is written in this form it is straightforward to implement numerically, as explained in Sec. 3.1.3.

### 3.1.2 Ghost points

When solving differential equations, we need boundary conditions to model what happens in areas where our differential equation is no longer valid. The Usadel equation does not model the interfaces between the normal metal and the superconductor and we thus need boundary conditions for this area. The most commonly used linear boundary conditions are classified into one of two types. First, we have Dirichlet boundary conditions where the function values at the boundary are specified. Second, are the Neumann boundary

conditions where the value of the derivative is what is specified at the boundary [65]. When combining these with the finite difference approach, the Dirichlet boundary conditions are straightforward to implement. However, implementing the Neumann boundary conditions, while still keeping the second-order accuracy, is not as straightforward. One simple way to use the same second-order finite difference scheme is to introduce so-called ghost points. These are an extra set of points lying outside of the boundary that can be used to calculate the derivative on the boundary using eq. (3.1.3). Say we have a set of points $\{x_1, \ldots, x_N\}$ separated by step length $h$, we then introduce two new points $x_0 = x_1 - h$ and $x_{N+1} = x_N + h$ which are the ghost points. If we then have Neumann boundary conditions

$$\begin{aligned} \partial_x f(x_1) &= c, \\ \partial_x f(x_N) &= d, \end{aligned} \tag{3.1.6}$$

we can use Eq. (3.1.3) to write them as

$$\begin{aligned} \frac{f(x_2) - f(x_0)}{2h} &= c, \\ \frac{f(x_{N+1}) - f(x_{N-1})}{2h} &= d. \end{aligned} \tag{3.1.7}$$

As the linearized Kuprianov-Lukichev boundary condition is a Neumann-type boundary condition this is a simple way of including them. In addition, we can include Dirichlet boundary conditions in this form by just setting the ghost points to the values given by the boundary conditions instead of using them in a derivative.

### 3.1.3 Solving the linearized Usadel equation

To solve the finite difference version of the linearized Usadel (3.1.5) equation numerically we need a way to solve for each grid point while also including the boundary conditions on the form (3.1.7). Let us assume that we work on a square grid of size $N \times N$ for simplicity, but this can easily be generalized to an $N \times M$ grid. A straightforward way is to convert the grid including ghost points, of size $(N+2) \times (N+2)$, to a vector of size $(N+2)^2$ and write all the coefficients in the linearized Usadel equation and the boundary conditions in a matrix. This allows us to write the equations to be solved as a matrix equation

$$\mathbf{M}\mathbf{x} = \mathbf{b}, \tag{3.1.8}$$

where $\mathbf{M}$ is a coefficient matrix and $\mathbf{b}$ are the constants that are not multiplied with any Green's function like the right-hand side of Eq. (3.1.7). Solving this equation for $\mathbf{x}$ then gives the value of the anomalous Green's function $f(x, y)$ at all points on the grid. Afterwards, we can easily eliminate the ghost points we introduced for the boundary conditions. As the coefficient matrix has shape $(N+2)^2 \times (N+2)^2$, the amount of entries scales as $\mathcal{O}(N^4)$, and becomes very large for large systems. However, if we consider the finite difference version of the linearized Usadel equation (3.1.5), we see that each row will have only 5 non-zero entries in $\mathbf{M}$. The rows accounting for the boundary conditions will contain only 2 non-zero entries, as we see from Eq. (3.1.7). Thus, this matrix is incredibly

sparse and the amount of non-zero elements scales as $\mathcal{O}(N^2)$, which is the same scaling as the number of grid points. This means that storing $\mathbf{M}$ as a sparse matrix makes it possible to work with larger systems than a dense storing would allow. As $\mathbf{M}$ is so sparse we can use sparse solvers to solve the system of equations more quickly than the dense equivalents would be able to.

To do this numerically, we first create the matrix $\mathbf{M}$ as a sparse matrix and the vector $\mathbf{b}$. This is then straightforward to solve with several methods, for example using LU factorization, to find $\mathbf{x}$. From the solution $\mathbf{x}$, it is then simple to calculate observables such as the supercurrent density using Eq. (1.5.21). Numerically we created the matrix $\mathbf{M}$ as a Compressed Sparse Column (CSC) matrix. Then, to solve the system we used the function `spsolve` from the `sparse.linalg` library in SciPy which uses the C library `SuperLU` to solve sparse systems of equations using LU factorization [66, 67].

## 3.2 Square geometry

First, we begin with a square of normal metal surrounded by a superconductor on the sides and vacuum at the top and bottom. This is rather similar to the cylindrical geometry studied in Ch. 2. However, the square has lower symmetry than a cylinder. In this section, we give an explanation of the system that is studied and discuss some theoretical background needed to treat this geometry.

### 3.2.1 Physical setup

The square geometry we now study consists of a normal metal square of side length $L$ and thickness $L_z$. A superconductor surrounds this normal metal on all four sides, and the system has vacuum interfaces at the top and bottom. This is shown in figure 3.1. The voltage applied to drive the system out of equilibrium uses the same quasiparticle injector as shown in Fig. 2.7. Just as we did for the cylindrical normal metal in Ch. 2, we will make some further assumptions. First, we assume zero temperature such that the distribution function is given by Eq. (1.2.56). We also assume that the thickness is much smaller than the inelastic scattering length such that the distribution function $h(\epsilon)$ does not depend on the $z$-coordinate even though we apply quasiparticle injector to drive it out of equilibrium on the top only. To be in the valid regime of quasiclassical theory we assume that $L$ is much larger than the Fermi wavelength. Moreover, we assume that $L$ is much larger than the elastic scattering length so that the Usadel equation is valid. In addition, we assume that the thickness of the superconductor is larger than the magnetic penetration depth and that it is larger than the coherence length in all dimensions. When we apply a magnetic field we will assume that it points in the $z$-direction, is constant in the normal metal and perfectly screened by the superconductor. This is accurate

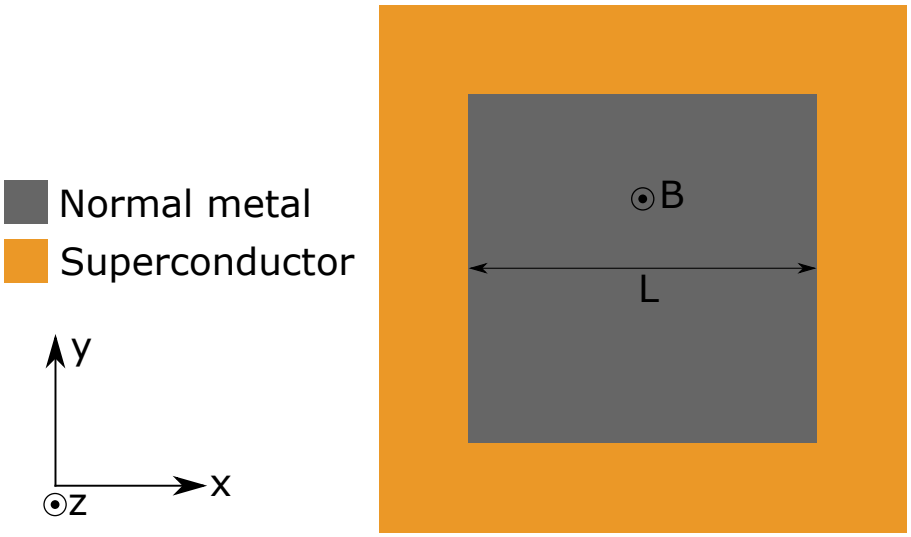


Figure 3.1: The square geometry studied in this section. It consists of a square normal metal with side length $L$ and thickness $L_z$ surrounded by a superconductor. A magnetic field is applied in the $z$-direction. The superconductor is much larger than shown in this figure.

when the proximity-induced superconductivity in the normal metal causes only weak screening currents whereas the superconductor has very strong screening currents. Given the strength of the magnetic field in the normal metal $\mathbf{B}_\mathrm{N}$, pointing in the $z$-direction, we can find the magnetic vector potential $\mathbf{A}$ in the normal metal using $\nabla \times \mathbf{A} = \mathbf{B}_\mathrm{N}$, the Coulomb gauge $\nabla \cdot \mathbf{A} = 0$ as well as boundary conditions from requiring zero current at the normal-metal/superconductor interface in Eq. (1.5.21).

### 3.2.2 Boundary conditions

For the interface between the superconductor and the normal metal, we need a boundary condition. Just as for the cylindrical case, we here use Kuprianov-Lukichev boundary conditions. They can be written as [68]

$$\frac{2L}{D}\check{\mathbf{I}} \cdot \mathbf{n} = -\frac{G_T}{G_N}\left[\check{\mathbf{g}}', \check{\mathbf{g}}\right]_- , \tag{3.2.1}$$

where $\check{\mathbf{I}}$ is the matrix current, $\check{\mathbf{g}}$ is the Green's function on the same side of the interface as the matrix current is computed, $\check{\mathbf{g}}'$ is the matrix current on the opposite side of the interface, $\mathbf{n}$ is the normal vector of the interface, $L$ is the length of the material in the direction normal to the interface, $G_T$ is the tunnelling conductance and $G_N$ is the conductance of the material on the same side as $\check{\mathbf{I}}$ is calculated. Let us first assume that we study an interface parallel to the $y$-axis where the normal metal is to the right of the superconductor. This means that we have a superconductor for $x < 0$ and a normal metal for $x > 0$ and $\mathbf{n} = \mathbf{e}_x$. Using Eq. (1.5.3) for the matrix current, we then get

$$\check{\mathbf{g}}\tilde{\nabla}_x\check{\mathbf{g}} = \frac{G_T}{2LG_N}\left[\check{\mathbf{g}}_\mathrm{BCS}, \check{\mathbf{g}}\right], \tag{3.2.2}$$

where the subscript BCS denotes the Green's function of the superconductor. Just as we did when we linearized the Usadel equation in Sec. 1.5.1, we consider the retarded component and use Eqs. (1.5.8) and (1.5.9) for the Green's function in the superconductor and normal metal to calculate that

$$(\hat{\boldsymbol{\rho}}_3 + \hat{\boldsymbol{f}})\tilde{\nabla}_x(\hat{\boldsymbol{\rho}}_3 + \hat{\boldsymbol{f}}) = \frac{G_T}{2LG_N}\left[g_\mathrm{BCS}\hat{\boldsymbol{\rho}}_3 + \begin{bmatrix} 0 & f_\mathrm{BCS}i\sigma^2 \\ -\tilde{f}_\mathrm{BCS}i\sigma^2 & 0 \end{bmatrix}, \hat{\boldsymbol{\rho}}_3 + \hat{\boldsymbol{f}}\right]_- . \tag{3.2.3}$$

As $\hat{\boldsymbol{\rho}}_3$ does not depend on the coordinates and it commutes with itself we have that $\tilde{\nabla}\hat{\boldsymbol{\rho}}_3 = 0$. Ignoring terms that are second order in $\hat{\mathbf{f}}$, we find that the left-hand side becomes

$$\hat{\boldsymbol{\rho}}_3\tilde{\nabla}\hat{\mathbf{f}}. \tag{3.2.4}$$

For the right-hand side, one needs to compute the commutator. As $g_\mathrm{BCS}$ is a scalar and the $f_\mathrm{BCS}$ term has the same structure as $\hat{\mathbf{f}}$, both of those terms end up having the same structure as the right-hand side in the linearized Usadel equation (1.5.12). In addition, $(i\sigma^2)^2 = -\sigma^0$, so the commutator between the $f_\mathrm{BCS}$ term and $\hat{\mathbf{f}}$ is a simple $2 \times 2$ commutator. Calculating this commutator explicitly, we find that the right-hand side of Eq. (3.2.3) becomes

$$\frac{G_T}{2LG_N}\begin{bmatrix} \left(f_\mathrm{BCS}\tilde{f} - f\tilde{f}_\mathrm{BCS}\right)\sigma^0 & 2(g_\mathrm{BCS}f - f_\mathrm{BCS})i\sigma^2 \\ 2(g_\mathrm{BCS}\tilde{f} - \tilde{f}_\mathrm{BCS})i\sigma^2 & -\left(f_\mathrm{BCS}\tilde{f} - f\tilde{f}_\mathrm{BCS}\right)\sigma^0 \end{bmatrix}. \tag{3.2.5}$$

Putting this together with Eq. (3.2.4), we see that

$$\hat{\boldsymbol{\rho}}_3\tilde{\nabla}_x\hat{\mathbf{f}} = \frac{G_T}{2LG_N}\begin{bmatrix}\left(f_{\mathrm{BCS}}\tilde{f} - f\tilde{f}_{\mathrm{BCS}}\right)\sigma^0 & 2(g_{\mathrm{BCS}}f - f_{\mathrm{BCS}})i\sigma^2 \\ 2(g_{\mathrm{BCS}}\tilde{f} - \tilde{f}_{\mathrm{BCS}})i\sigma^2 & -\left(f_{\mathrm{BCS}}\tilde{f} - f\tilde{f}_{\mathrm{BCS}}\right)\sigma^0\end{bmatrix}. \tag{3.2.6}$$

As $\hat{\mathbf{f}}$ is antidiagonal and the action of $\tilde{\nabla}$ does not change the matrix structure, we see that we get that $f_{\mathrm{BCS}}\tilde{f} - f\tilde{f}_{\mathrm{BCS}} = 0$. This is to be expected as $f$ and $\tilde{f}$ are perturbations caused by $f_{\mathrm{BCS}}$ and $\tilde{f}_{\mathrm{BCS}}$, and thus $f$ and $f_{\mathrm{BCS}}$ should have the same symmetry under tilde conjugation. Thus, taking the tilde conjugate of two of them should not change the result, i.e. $f\tilde{f}_{\mathrm{BCS}} = \tilde{f}f_{\mathrm{BCS}}$. This means that both diagonal terms cancel and the boundary conditions become

$$\hat{\boldsymbol{\rho}}_3\tilde{\nabla}_x\hat{\mathbf{f}} = \frac{G_T}{LG_N}\begin{bmatrix}0 & (g_{\mathrm{BCS}}f - f_{\mathrm{BCS}})i\sigma^2 \\ (g_{\mathrm{BCS}}\tilde{f} - \tilde{f}_{\mathrm{BCS}})i\sigma^2 & 0\end{bmatrix}. \tag{3.2.7}$$

Finally, if we assume that the vector potential is parallel to the interface, which in this case means $\mathbf{A} \sim \mathbf{e}_y$, the covariant derivative is equivalent to a normal derivative. Doing the matrix multiplication we get

$$\begin{bmatrix}0 & \partial_x f i\sigma^2 \\ \partial_x\tilde{f}i\sigma^2 & 0\end{bmatrix} = \frac{G_T}{LG_N}\begin{bmatrix}0 & (g_{\mathrm{BCS}}f - f_{\mathrm{BCS}})i\sigma^2 \\ (g_{\mathrm{BCS}}\tilde{f} - \tilde{f}_{\mathrm{BCS}})i\sigma^2 & 0\end{bmatrix}. \tag{3.2.8}$$

These are just two scalar equations for $f$ and $\tilde{f}$. Defining $\gamma = \frac{G_T}{LG_N}$ as the measure of the interface resistance, the scalar equation for $f$ becomes

$$\partial_x f = \gamma(g_{\mathrm{BCS}}f - f_{\mathrm{BCS}}). \tag{3.2.9}$$

Except for the factor $g_{\mathrm{BCS}}f$, this exactly matches the expression given by F. S. Bergeret et al. [56], and is exactly the same as the expression found in their appendix. As this factor contains $f$, which is small in the limit of weak proximity effect, where $|f| \ll |f_{\mathrm{BCS}}|$, it will always be dominated by the $f_{\mathrm{BCS}}$ term and we can safely neglect $g_{\mathrm{BCS}}f$.[2]

### 3.2.3 Magnetic field correction

When applying a magnetic field to a superconducting system, this induces screening currents in the material. From these currents, one can then calculate an induced magnetic field. The change in the magnetic flux distribution then leads to a corresponding change in the screening currents, so in general, one has to do self-consistent calculations. However, we assume that the normal metal is relatively thin and that the induced superconductivity is weak, which leads to weak supercurrents in the normal metal. This means that we do not require full self-consistent calculations, but only calculate a first correction to the magnetic field. To find the magnetic field redistribution produced by the screening currents in the normal metal, we start with Ampere's law [69]

$$\nabla \times \mathbf{B} = \mu_0\mathbf{J}, \tag{3.2.10}$$

[2]This has also been confirmed numerically by including the term in simulations of the systems we will consider in this thesis.

where $\mathbf{B}$ is the magnetic field and $\mathbf{J}$ is the current in the system. Using that the magnetic vector potential is defined as $\mathbf{B} = \nabla \times \mathbf{A}$ we can we can write

$$\nabla^2 \mathbf{A} = -\mu_0 \mathbf{J}. \tag{3.2.11}$$

Here we have used the identity $\nabla \times \nabla \times \mathbf{A} = \nabla(\nabla \cdot \mathbf{A}) - \nabla^2 \mathbf{A}$ as well as the Coulomb gauge $\nabla \cdot \mathbf{A} = 0$. We see that eq. (3.2.11) is a Poisson equation for $\mathbf{A}$, which has the general solution [60]

$$\mathbf{A}(\mathbf{r}) = \frac{\mu_0}{4\pi} \int \frac{\mathbf{J}(\mathbf{r}')}{|\mathbf{r} - \mathbf{r}'|} \mathrm{d}^3 x'. \tag{3.2.12}$$

Using this equation with the currents calculated from the Green's function using Eq.(1.5.21) then allows us to calculate a correction to the magnetic vector potential and thus the magnetic field from $\mathbf{B} = \nabla \times \mathbf{A}$.

One could easily imagine systems where this first-order approximation would not hold, such as a superconductor or a very thick normal metal. Then one would have to calculate the change in the magnetic field $\delta\mathbf{B}(\mathbf{r})$ from $\delta\mathbf{A}(\mathbf{r})$ and solve the linearized Usadel equation with this magnetic field redistribution added to the external field again and again until there is no change in $\delta\mathbf{B}(\mathbf{r})$, so-called self-consistent calculations. However, this is not the case for the systems we will consider. First, we see from Eq.(1.5.21) that the supercurrents in the normal metal are proportional to $f^2$. From Eq. (3.2.12) we also see that $\delta\mathbf{B}(\mathbf{r})$ is proportional to the thickness of the system $L_z$. Thus we see that $\delta\mathbf{B}(\mathbf{r})$ is proportional to $f^2 L_z$. In the systems we will consider we assume that there is a weak proximity effect inducing superconductivity in the normal metal such that $|f| \ll |f_{\mathrm{BCS}}|$ and we also assume that the system is relatively thin such that $L_z$ is small. This means that if we were to solve the linearized Usadel equation again with $\mathbf{B}(\mathbf{r}) + \delta\mathbf{B}(\mathbf{r})$, we would get extra corrections to the supercurrents of order $f^4 L_z$ and an extra magnetic field correction $\delta\mathbf{B}_2(\mathbf{r})$ of order $f^4 L_z^2$. This means that we would get $|\delta\mathbf{B}_2(\mathbf{r})| \ll |\delta\mathbf{B}(\mathbf{r})|$, showing that it is sufficient to only calculate the first order correction $\delta\mathbf{B}(\mathbf{r})$.

### 3.2.4 Pair correlation

When investigating superconducting materials, one interesting property is how strong the superconductivity is in different parts of the material. One measure of this is the pair correlation $\Psi$, which is a measure of the density of the superconducting condensate, i.e. the Cooper pairs, in a superconducting material. In a superconductor, it can be written as [50]

$$\Psi = n_s^{1/2} e^{i\phi}, \tag{3.2.13}$$

where $n_s$ is the density of Cooper pairs. As this is directly proportional to the density of the Cooper pairs it is zero above the critical temperature $T_\mathrm{c}$ and increases below $T_\mathrm{c}$. This means that $\Psi$ can be an order parameter for the superconducting condensate. While $\Psi$ is usually zero in a normal metal, it can be finite if there is proximity-induced superconductivity. In these cases, $\Psi$ can also be used to calculate the magnitude and distribution of the superconducting condensate.

When studying superconducting vortices the pair correlation is useful to quantify the vortices. In the middle of the vortex, the superconductivity is destroyed $\Psi \to 0$. In addition, the phase of $\Psi$ winds an integer multiple of $2\pi$ around the vortex. This means

we can use $\Psi$ to pinpoint the location of the center of the vortex and find how much the phase winds around one vortex. Using the Green's function formalism we can calculate it as [26]

$$\Psi \sim \int_0^{\omega_c} h(\epsilon)(f(\mathbf{r},\epsilon) - f(\mathbf{r},-\epsilon))\mathrm{d}\epsilon. \tag{3.2.14}$$

This is a complex function and can thus be written as

$$\Psi = |\Psi|\exp(i\phi). \tag{3.2.15}$$

The phase of the superconducting condensate can be extracted as $\phi = \arctan(\mathrm{Im}(\Psi)/\mathrm{Re}(\Psi))$. As $\Psi$ has to be singly defined this phase will only change in multiples of $2\pi$ when doing a line integral around the vortex

$$\Delta\phi = \oint_{\mathcal{C}} \phi \ \mathrm{d}l. \tag{3.2.16}$$

Here $\Delta\phi$ is the phase change when integrating around the vortex, where $\mathcal{C}$ is a closed loop containing the center of the vortex. Thus, to quantify the vortices we define the winding number

$$n = \frac{\Delta\phi}{2\pi}. \tag{3.2.17}$$

We also define the total vorticity $N$ as the sum of the winding numbers of all the vortices in a sample

$$N = \sum_i n_i. \tag{3.2.18}$$

When considering superconducting vortices the winding number counts the number of magnetic flux quanta $\Phi = \hbar\pi/e$ penetrating the superconductor in a single vortex while the total vorticity counts the total amount of magnetic flux quanta penetrating the superconductor. Most superconducting vortices will have a winding number of 1. This is due to the fact that the kinetic energy of a vortex is proportional to $n^2$ [70], and thus two vortices with $n = 1$ have lower energy than a single giant vortex with $n = 2$. However, Amundsen et al. [26] showed that symmetry constraints can lead to creation of giant vortices with winding numbers $n > 1$.

## 3.3 Square geometry results

We now study numerically the normal metal surrounded by a superconductor as discussed in Sec. 3.2. This was studied both in the case with an applied magnetic field and without an applied magnetic field. In the case without an applied magnetic field, there is a supercurrent flowing in the surrounding superconductor, which leads to a phase winding in the superconductor. When doing the simulations we normalized all lengths with respect to the coherence length and all energies with respect to the gap. For example $L \to L/\xi$, $\epsilon \to \epsilon/\Delta$ and $eV \to eV/\Delta$. We also added a small imaginary part to the energy $\epsilon \to \epsilon + i\delta$ with $\delta = 0.01\Delta$ to regularize the Green's function close to the gap and match the experimental measurements by Dynes et al. [62].

### 3.3.1 No magnetic field

The case without an applied magnetic field has already been studied by Amundsen et al [26]. They studied a normal metal surrounded by a current-carrying superconductor. This current was driven externally and would also lead to a magnetic field, however, this was neglected since the system was thin in the z-direction. Their main focus was on square geometries, but they also studied a hexagonal one, which we will not consider here. In the square case, they showed that for an applied vorticity of $N = 2$, a giant vortex is created with winding number $n = 2$. This happens as it has to respect the discrete symmetries of the system. This symmetry also leads to an antivortex forming in the $N = 3$ case. We here show that we reproduce the results with our independently written code.

To form giant vortices and antivortices it has to be both energetically favourable and also respect the discrete symmetries of the system. From three simple rules, we can deduce most vortex patterns. First, the sum of the winding numbers of all the vortices has to equal the total vorticity coming from the surrounding superconductor. For a square system with total phase winding $2\pi$, i.e. total vorticity $N = 1$, from the surrounding superconductor a single vortex is formed in the center. However, for a system with total vorticity $N = 2$ we cannot create two normal vortices since there are no ways for two vortices to distribute themselves that respect the 4-fold symmetries of a square. Thus we end up with an $n = 2$ giant vortex in the middle. If we consider a system with total vorticity $N = 3$ we end up with two possibilities that respect the discrete symmetry. One is a giant vortex with winding number $n = 3$ in the middle of the system and the other is an antivortex with winding number $n = -1$ in the middle and 4 surrounding normal vortices along the diagonals to maximize the distance between them. As the kinetic energy scales with the square of the current, it is proportional to $n^2$ [70]. This means that the energy of the giant vortex configuration gets a prefactor $3^2 = 9$ while the antivortex case gets a prefactor 5. Thus the antivortex configuration has lower energy and will be the one that is realized. For total vorticity $N = 4$ we will have 4 normal vortices forming along the diagonals. With total vorticity $N = 5$, we end up with 4 vortices forming along the diagonals and one in the middle and we are basically back to the $N = 1$ case, just with 4 extra $n = 1$ vortices.

If we instead consider a regular polygon with $k$ sides we still get a single vortex when the surrounding superconductor induces a total vorticity $N = 1$. However, for larger $N$ it depends on the value of $k$. While $N$ is smaller than or equal to $\left\lfloor \frac{k}{2} \right\rfloor$, where $\lfloor i \rfloor$ is the floor

of $i$, we get a giant vortex with winding number $n$. If we were to create an antivortex in the middle instead we would need $k$ surrounding normal vortices. For $N \leq \left\lfloor \frac{k}{2} \right\rfloor$ this would lead to the antivortex having a winding number with the same or larger magnitude than the giant vortex case. With the addition of the extra normal vortices this would lead to higher energy. For $\left\lceil \frac{k}{2} \right\rceil < N < k$, where $\lceil i \rceil$ is the roof of $i$, the lowest energy configuration is $k$ normal vortices along the symmetry lines of the polygon and an antivortex in the middle with winding number $k - N$. If $k$ is odd and we have $N = \frac{k+1}{2}$ both the single giant vortex and the antivortex distributions obtain the same prefactor. Thus, this simple argument does not decide which one of them ends up appearing. In these cases, the interaction between vortices and antivortices will be affecting the resulting configuration. As there is an attraction between vortices with opposite signs of the winding number and a repulsion between vortices with the same sign, the fact that the antivortex is in the middle means that it is closer to each of the normal vortices than they are to each other. Thus, this attraction will lower the total energy more than the repulsion between the normal vortices will raise it and the configuration with an $n = (k-1)/2$ antivortex in the middle with $k$ surrounding normal vortices will be the one preferred. In the case of a triangle, i.e. $k = 3$, this has been studied by Chibotaru et al. [71] who found that in a triangle an antivortex is created in the middle with 3 surrounding normal vortices when a magnetic field of strength $2\Phi_0$, which corresponds to a total vorticity of $N = 2$, is applied.

To study the appearance of giant and antivortices we studied a system with a normal metal surrounded by a current-carrying superconductor by solving the linearized Usadel equation as explained in Sec. 3.1.3. The amplitude and phase of the pair correlation as well as the supercurrents in the normal metal are shown in Fig 3.2. When considering the phase we see that each discontinuity changes the phase by $\pi$. Since a vortex has a total phase change of $2\pi n$ when integrating around a closed loop enclosing the vortex center, we need to cross two discontinuities for a normal $n = 1$ vortex for the correct phase change. If we consider the $N = 1$ case, we see that we have two discontinuities originating from the center which means this is a normal $n = 1$ vortex centered in the middle of the normal metal. The currents also show that this is a single vortex as they all flow around the middle of the normal metal. In the $N = 2$ case, we see that we have 4 discontinuities originating from the center which means that this is a single $n = 2$ giant vortex. Again the supercurrents flow around the center showing just a single vortex. For the $N = 3$ case, we see that we now have 5 vortices. The one in the middle winds the other way and counting the discontinuities we see that this is an $n = -1$ antivortex. The surrounding vortices are $n = 1$ normal vortices. This is also supported by the supercurrents as the current flows the opposite way around the middle vortex when compared to the other 4 normal vortices. All five vortices are quite close, which is likely due to the antivortex attracting the normal vortices as they wind in the opposite direction [50]. Due to their relative closeness, they also suppress the pair correlation over a greater area compared to the $N = 1$ and $N = 2$ cases. Finally, in the $N = 4$ case, we see that we have 4 normal vortices that are quite spread out. As they all have the same vorticity, they repel each other and if we compare to the $N = 3$ case there is no antivortex that attracts them towards the middle. We also see that the pair correlation is suppressed the most at the cores of the vortices, and quite a large area in the middle has a partly suppressed pair correlation. This means that unlike the other cases where the pair correlation goes to 0 in the center of the sample, that is not the case here.

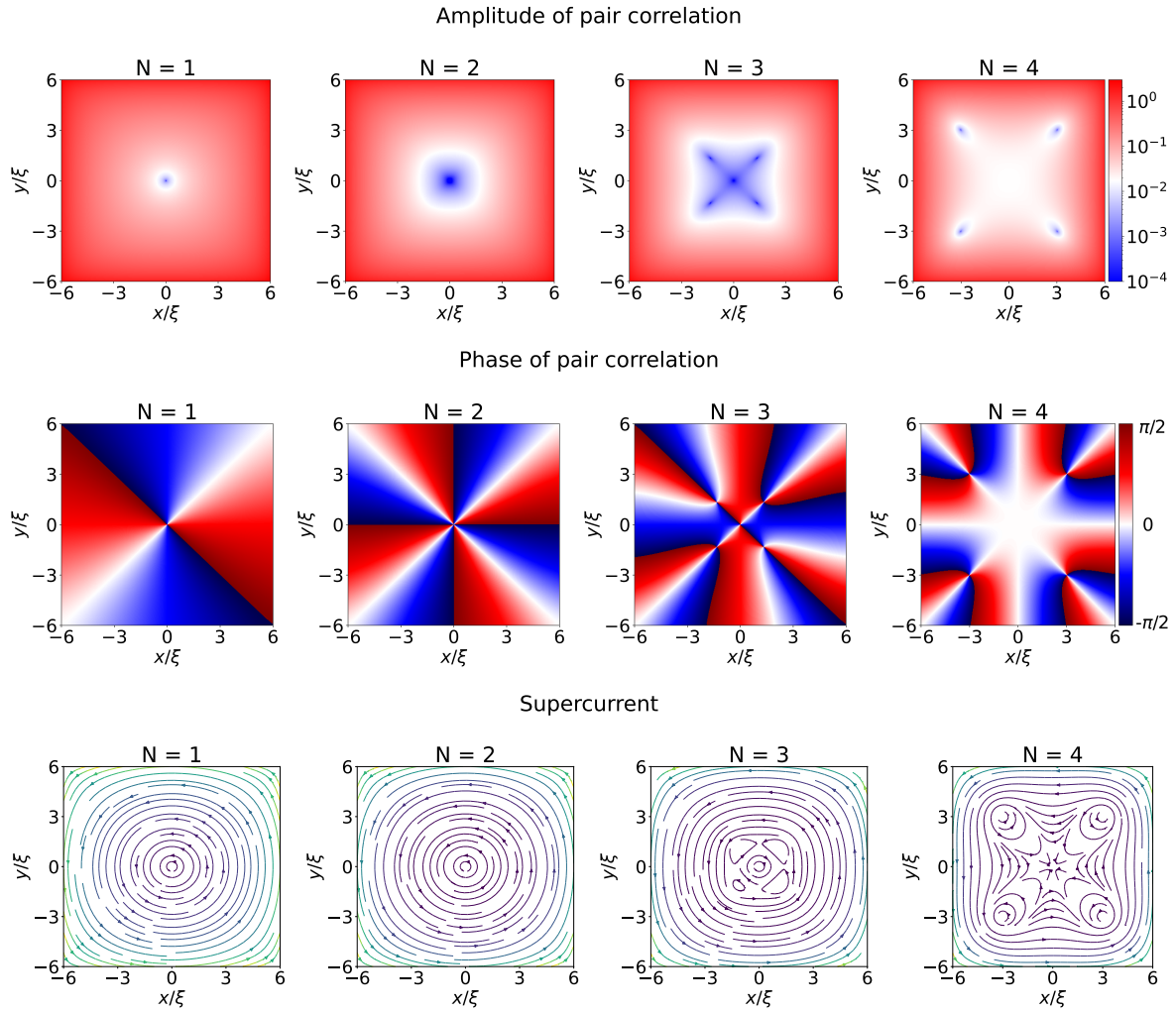


Figure 3.2: The amplitude and phase of the pair correlation and the supercurrents in the normal metal. We see the formation of a giant vortex in the $N = 2$ case and an antivortex in the $N = 3$ case.

The distribution of vortices and antivortices in Fig. 3.2 are all in agreement with the ones derived by the simple arguments based on symmetry and energy presented above. This shows that these two factors are the dominating ones in deciding the distribution of the vortices in the proximitized normal metal.

### 3.3.2 With magnetic field

We now consider the same geometry, but instead of an externally applied electric current to generate the vortices, we now apply an out-of-plane magnetic field which induces screening currents in the proximitized normal metal. Just as for the cylindrical case, we assume that the magnetic field $\mathbf{B}_N$ is constant within the normal metal and that there is perfect screening in the superconductor. The two contributions to the screening currents are the magnetic vector potential and the gradient, that is the phase change, as seen in Eq. (1.5.21). This means that the assumption of perfect screening in the superconductor implies that the magnetic vector potential and the phase change cancel perfectly in the superconductor. These conditions, in addition to the Coulomb gauge $\nabla \cdot \mathbf{A} = 0$, allow us to completely determine the magnetic vector potential $\mathbf{A}$.

Fig 3.3 and Fig 3.4 show the supercurrent density in the normal metal for two different lengths of the normal metal $L = 4\xi$ and $L = 8\xi$ and three different applied voltages $eV = 0$, $eV = 0.15\Delta$ and $eV = 0.5\Delta$. When there is no applied voltage, we see that the currents try to contain the magnetic field within the center of the vortex and thus try to screen the magnetic field in the same way as a type-II superconductor. We also see that the currents are mostly circular, which leads to the currents in the corners not being able to circulate. When applying a voltage of $eV = 0.15\Delta$ we see a big difference between $L = 4\xi$ and $L = 8\xi$. For $L = 4\xi$ there is almost no change from the case without any applied voltage, only a slight reduction in the currents closest to the center of the normal metal. This shows that the screening currents are not carried by modes close to the Fermi level. However, for $L = 8\xi$ we see that most of the central currents are reversed by applying $eV = 0.15\Delta$ and only in the corners is there a current that is not reversed. This current in the corners is due to edge effects, the screening currents are circular and thus they are not in the corner of the normal metal. One could view these corner currents as the screening currents from the superconductor leaking into the normal metal so that they do not have to travel in a square path around it. However, for this to be the case they should clearly visible also before reversing the current, which they are not. The fact that we have a reversal in most of the normal metal at this low of a voltage shows that here most of the diamagnetic response is carried by modes with energy close to the Fermi level. This mirrors what we saw in the cylindrical case in Sec. 2.2. When the normal metal becomes larger, more of the diamagnetic screening is carried by modes very close to the Fermi level, whereas this is not as pronounced for smaller normal metals. Finally, increasing the voltage to $eV = 0.5\Delta$ we see that we have a reversal of the currents in both cases, except for in the corners where the edge effects play a major role. We also observe that for $L = 8\xi$ there is an area in the middle of the normal metal where almost no currents flow. This is the area furthest from the superconductor that induces the superconductivity and by applying such a large voltage we can view this as closing the minigap, thus destroying the superconductivity in this area. Finally, we note that for all three voltages, the current in the $L = 8\xi$ normal metal is significantly weaker than the

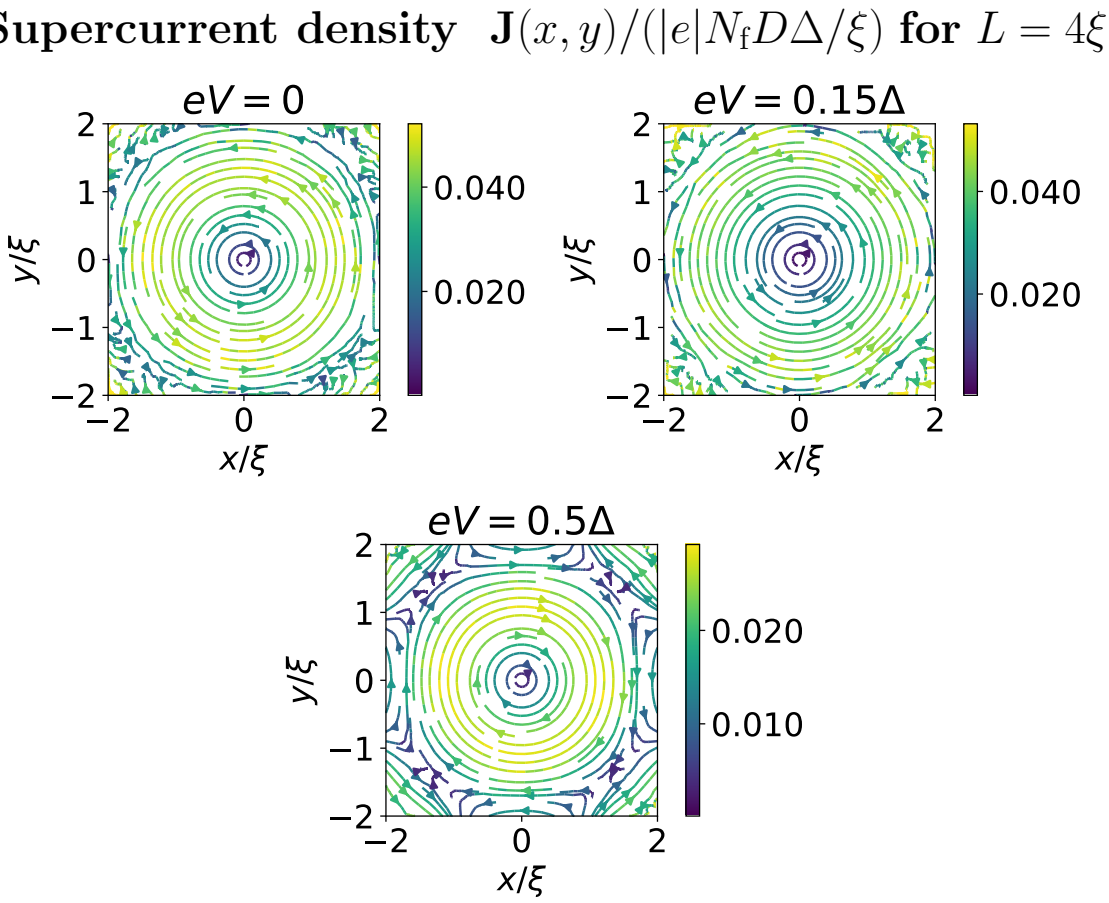


Figure 3.3: Streamplots of the current density $\mathbf{J}(x,y)/(|e|N_\mathrm{f}D\Delta/\xi)$ for a normal metal with side lengths $L = 4\xi$ surrounded by a superconductor for three different values of the applied voltage $eV$. We observe that the screening currents are fully reversed at an applied voltage of $eV = 0.5\Delta$.

$L = 4\xi$ normal metal, especially when we apply a voltage. As there is always a single magnetic flux quantum penetrating the normal metal, this means that the magnetic field density is 4 times as large for $L = 4\xi$ compared to $L = 8\xi$. This means that the screening currents need to be larger in this case. When we apply a voltage, the size also matters as more of the normal metal is further from the superconductor in the $L = 8\xi$ case, meaning that it has weaker induced superconductivity. When we then apply a voltage, it is easier to suppress this superconductivity, leading to a lower supercurrent density.

We can also consider the magnetic field induced by the supercurrent density, which is shown in Fig 3.5 for a normal metal with side lengths $L = 8\xi$. Without any applied field, we see that the induced magnetic field looks like that in a type-II superconductor. The magnetic field is enhanced in the middle, while on the sides it is suppressed, thus it tries to create a superconducting vortex. When we then apply a voltage of $eV = 0.15\Delta$ we see that we partly reverse this. Now the area closest to the middle tries to reduce the magnetic field while a large area around has an increased magnetic flux. Finally, when we increase the applied voltage to $eV = 0.5\Delta$, we see that we have fully reversed the induced magnetic field. The area closest to the middle has almost no change in the magnetic field

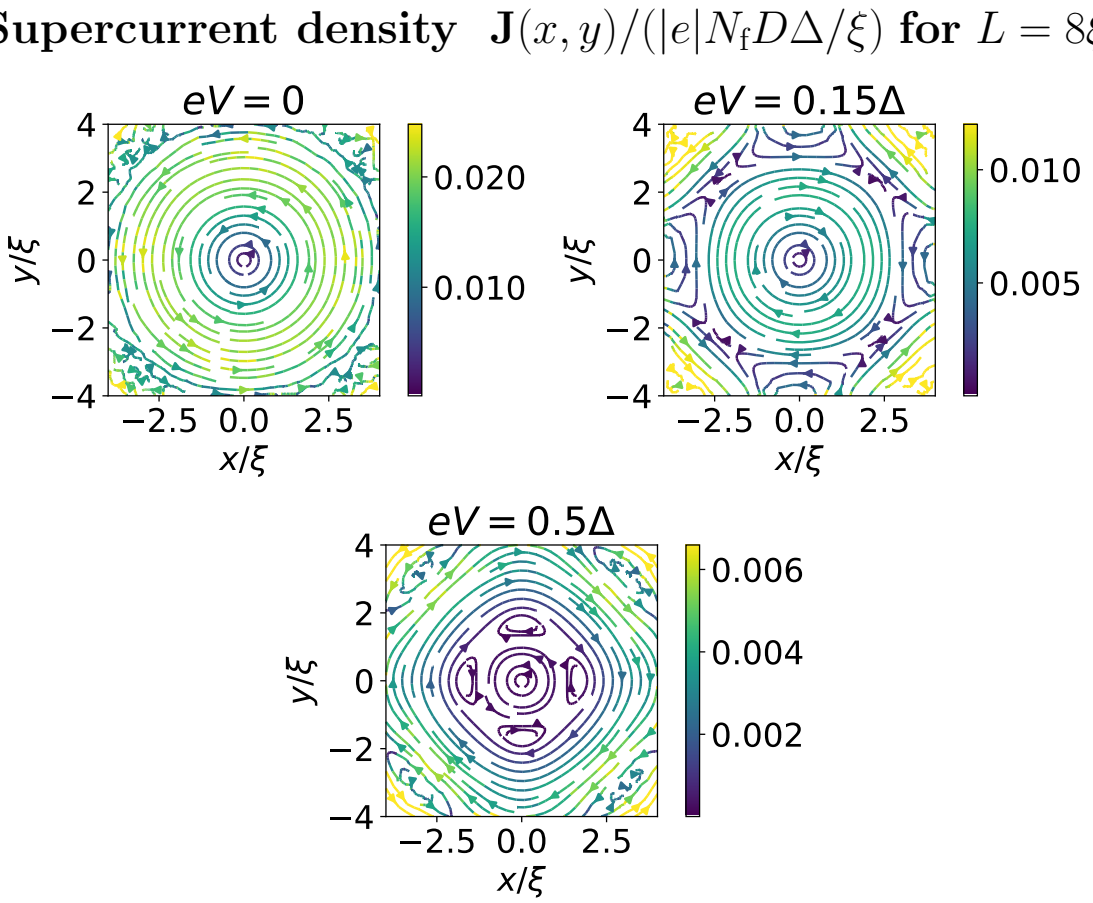


Figure 3.4: Streamplots of the current density $\mathbf{J}(x,y)/(|e|N_\mathrm{f}D\Delta/\xi)$ for a normal metal with side lengths $L = 8\xi$ surrounded by a superconductor for three different values of the applied voltage $eV$. We observe that parts of the screening currents are reversed at an applied voltage of $eV = 0.15\Delta$ and they are fully reversed for $eV = 0.5\Delta$.

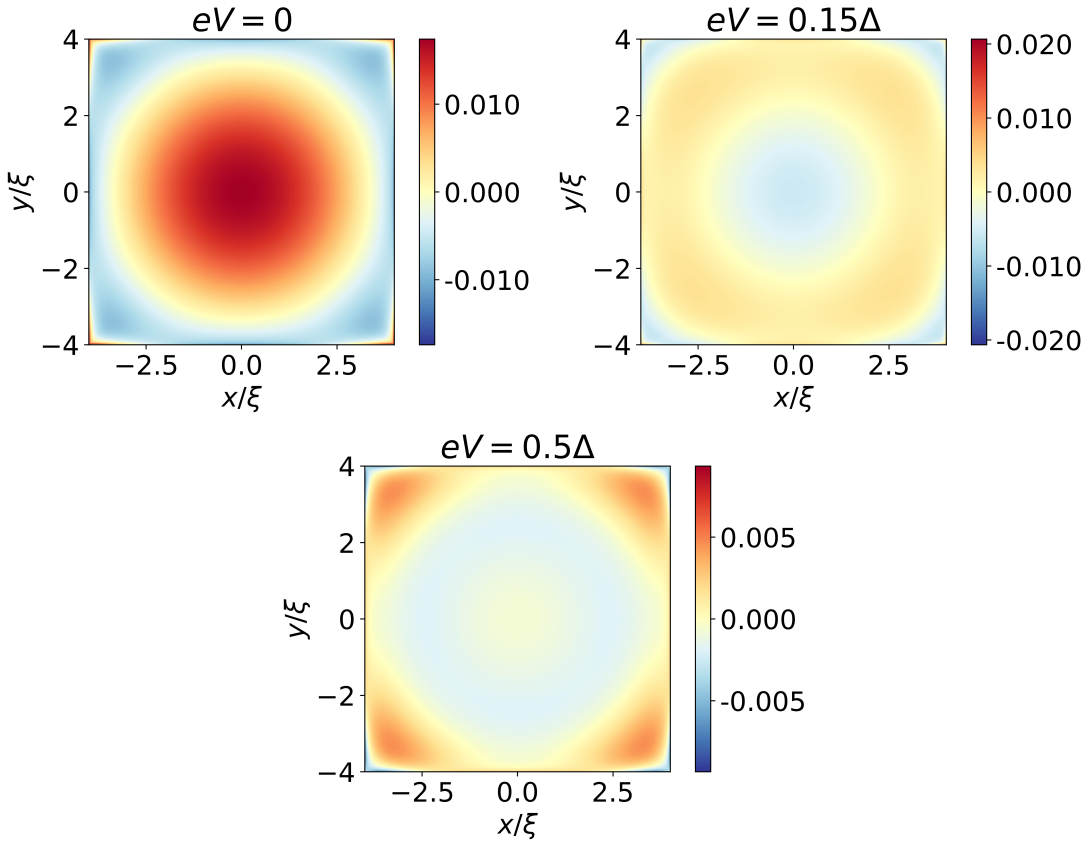


Figure 3.5: Magnetic field induced by the supercurrents $\mathbf{B}_{\text{ind}}(x, y)/(|e|\mu_0 N_{\text{f}} D\xi L_z)$ in a normal metal with side lengths $L = 8\xi$ surrounded by a superconductor for three different values of the applied voltage $eV$. We observe that the magnetic field is concentrated into the middle for $eV = 0$, mirroring a vortex in a bulk type-II superconductor. For $eV = 0.15\Delta$ and $eV = 0.5\Delta$ the magnetic field is forced away from the middle of the normal metal, giving the opposite response of a vortex in a bulk type-II superconductor.

as there are no supercurrents flowing. Around that, the induced magnetic field points in the opposite direction of the applied field, reducing the magnetic flux density. Only in the corners of the normal metal is there an increase in the magnetic field density, which is caused by the strong currents in these areas, originating from edge effects.

It is also interesting to know how big of a voltage one should use in the quasiparticle injector to reverse the response of the normal metal. We thus define the switching voltage $eV_s$ as the amount of voltage needed to have the sum of the current circulating the vortex be 0. The circulating current only includes the current normal to the straight line from a grid point to the center with positive circulation being defined by the right-hand rule, thus it is effectively a cross product between the current and the normalized vector from the origin to the grid point. This is similar to the definition in Sec. 2.2, however, there all current was azimuthal and thus all current was part of the circulating current. For the quadratic normal metal the switching voltage is shown in Fig. 3.6 as a function of the side length of the normal metal. We see that for a small normal metal, the switching voltage is very large, such that one would destroy the superconductivity before reaching this applied voltage physically. This is due to the strong induced superconductivity in

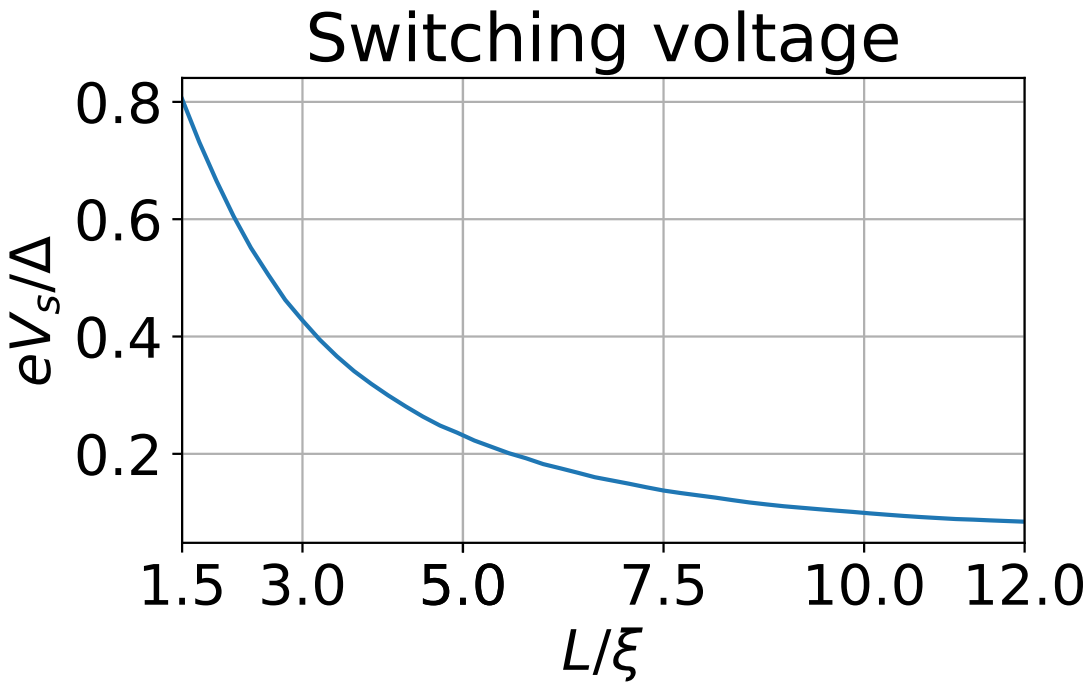


Figure 3.6: Switching voltage $eV_s/\Delta$ for a normal metal surrounded by a superconductor. The switching voltage is large for small radii where the magnetic field density is high and the induced superconductivity is relatively strong. When increasing the size of the normal metal we see that the switching voltage is reduced because of a larger area with weaker superconductivity and a lower magnetic field density.

such a small normal metal. When the side length of the normal metal is increased, the switching voltage decreases quite rapidly. This is because an increasing portion of the area has a weaker induced superconductivity that is easier to reverse. In addition, the spectral current density depends on the size in much the same way as we saw for a cylinder of normal metal in Fig. 2.2 and we have thus not included it explicitly. We have that for a small square of normal metal, the screening currents are dominated by diamagnetic modes with energy close to the gap. When one increases the size the diamagnetic response is mostly coming from modes with energy close to the Fermi energy, while close to the gap there are mostly paramagnetic states. In the area between the Fermi energy and the gap, an increasing amount of states become paramagnetic when the size increases. For larger sizes of the normal metal, there is still a decline, but it changes less. There is always an area with relatively strong superconductivity at the edge and there is always a diamagnetic contribution close to the Fermi energy leading to there leading to less change in the applied voltage needed to reverse the screening currents.

## 3.4 Thin film

The cylindrical and square normal metals surrounded by a superconductor are interesting to study for their behaviours and symmetries. However, they are not the easiest geometries to realize experimentally. Thus, in this chapter, we will investigate a thin film of normal metal placed on top of a bulk type II superconductor. This allows induced superconductivity, and depending on the applied field, we can have one or more vortices in the superconductor. This then leads to these vortices also being contained in the normal metal due to the induced superconductivity, letting us study both isolated vortices and vortices in a lattice.

### 3.4.1 Physical setup

The thin film geometry we now study is shown in Fig. 3.7. It consists of a square thin film of normal metal of thickness $L_z$ and with side lengths $L$ placed on top of a type-II superconductor. We apply a magnetic field from below the superconductor that points in the $z$-direction and assume that this leads to the formation of vortices in the superconductor. Due to the proximity-induced superconductivity, this also leads to superconducting vortices in the normal layer as has been observed both for very thin normal metal layers [72] and for a rather thick normal metal layer [73]. As the normal metal layer is thin, we assume that the magnetic field structure of the vortices in the superconductor is the same in the normal metal, thus we view this as an applied field for the normal metal. A voltage is applied using the setup of a quasiparticle injector shown in Fig. 2.7 and we assume zero temperature, which leads to a distribution function given in Eq. (1.2.56). Just as we did for the earlier geometries, we further assume that the thickness of the normal metal is much smaller than the inelastic scattering length, such that $h(\epsilon)$ is constant in the entire normal metal. We also assume that $L$ is much larger than the Fermi wavelength, so the quasiclassical approximation is valid. For the Usadel equation to be valid we also assume that $L$ is much greater than the elastic scattering length.

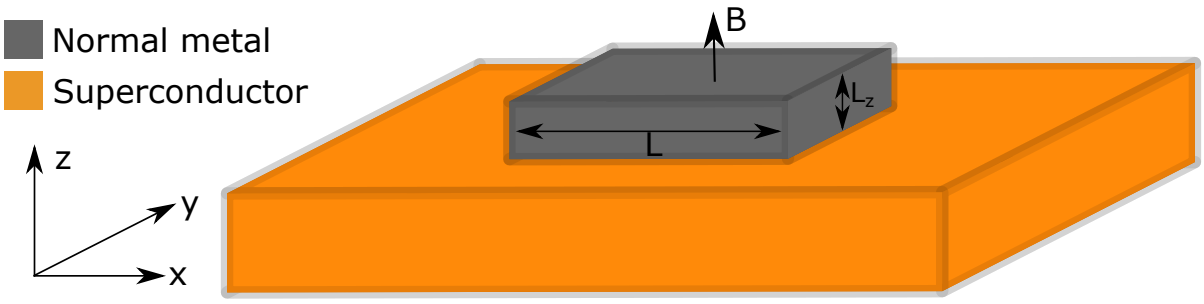


Figure 3.7: The geometry of a thin film of normal metal placed on top of a type II superconductor. The normal metal is a square with in-plane dimensions $L \times L$ and out-of-plane thickness $L_z$. A magnetic field is applied in the $z$-direction to create Abrikosov vortices in the superconductor and thus also the normal metal.

### 3.4.2 Integrated Usadel equation

In systems with a thin normal metal layer on top of a superconductor, one can integrate out the boundary conditions between the superconductor and normal metal. The boundary conditions then appear as an extra term in the Usadel equation. We have Kuprianov-Lukichev boundary conditions at the normal metal-superconductor interface at $z = 0$, which can be written as [68]

$$\frac{2L_z}{D}\check{\mathbf{I}} \cdot \hat{\mathbf{n}} = -\frac{G_T}{G_N}\left[\check{\mathbf{g}}', \check{\mathbf{g}}\right]_-, \tag{3.4.1}$$

where $\check{\mathbf{g}}$ is the Green's function on the same side of the interface as the matrix current is computed, $\check{\mathbf{g}}'$ is the matrix current on the opposite side of the interface, $\check{\mathbf{I}}$ is the matrix current, $\hat{\mathbf{n}}$ is the normal vector of the interface, $L$ is the length of the material normal to the interface, $G_T$ is the tunnelling conductance, and $G_N$ is the conductance in the normal state. At the top of the normal metal $z = L_z$, we have vacuum boundary conditions

$$\check{\mathbf{I}} \cdot \hat{\mathbf{n}} = 0. \tag{3.4.2}$$

The Usadel equation is

$$\tilde{\nabla} \cdot \check{\mathbf{I}} = i[\check{\mathbf{\Sigma}}, \check{\mathbf{g}}]_-, \tag{3.4.3}$$

and we will show that we can incorporate the boundary conditions in the $z$ component of the derivative. As we will work with a vector potential without a $z$ component, we have $\tilde{\nabla}_z = \partial_z$. Since we assume that the normal metal is thin in the $z$-direction, $\check{\mathbf{I}}$ has an approximately linear dependence on $z$

$$\partial_z \check{\mathbf{I}}_z \approx \frac{\check{\mathbf{I}}_z\big|_{z=L_z} - \check{\mathbf{I}}_z\big|_{z=0}}{L_z}. \tag{3.4.4}$$

Using the vacuum and Kuprianov-Lukichev boundary conditions to evaluate $\check{\mathbf{I}}_z$ this can be written as

$$\partial_z \check{\mathbf{I}}_z = -\frac{G_T D}{2G_N L_z^2}\left[\check{\mathbf{g}}_{\mathrm{BCS}}, \check{\mathbf{g}}\right]_-, \tag{3.4.5}$$

where the subscript BCS specifies that this is the Green's function in the superconductor. Returning to the Usadel equation, we can now separate out the $z$-component of the dot product and move it over to the right-hand side to get

$$\tilde{\nabla} \cdot \check{\mathbf{I}} = [i\check{\mathbf{\Sigma}} + \frac{G_T D}{2G_N L_z^2}\check{\mathbf{g}}_{\mathrm{BCS}}, \check{\mathbf{g}}]_-. \tag{3.4.6}$$

When we now linearize Eq. (3.4.6), we get the same terms as in chapter 1.5 but we also have the Kuprianov-Lukichev term. This commutator has already been calculated in Sec. 3.2.2. Thus, except for some constants, we get the same form as the right-hand side of Eq. (3.2.8)

$$[\frac{G_T D}{2T_N L_z^2}\check{\mathbf{g}}_{\mathrm{BCS}}, \check{\mathbf{g}}]_- = \frac{\gamma D}{2L_z}\begin{bmatrix} 0 & 2\left(g_{\mathrm{BCS}} f - f_{\mathrm{BCS}}\right) i\sigma^2 \\ 2\left(g_{\mathrm{BCS}}\tilde{f} - \tilde{f}_{\mathrm{BCS}}\right) i\sigma^2 & \end{bmatrix}, \tag{3.4.7}$$

where $\gamma = G_T/(G_N L)$ is a measure of the interface resistance. This has the same matrix structure as Eq. (1.5.11) and we can therefore split it into two equations and only solve for $f$ to get

$$(\nabla - 2ie\mathbf{A})^2 f = -\left(2i\frac{\epsilon}{D} + \frac{\gamma}{L_z} g_{\text{BCS}}\right) f - \frac{\gamma}{L_z} f_{\text{BCS}}. \tag{3.4.8}$$

Just as in Eq. (3.2.9), we can neglect the term $(G_0/L_z)g_{\text{BCS}}f$ as this term is dominated by the term $(G_0/L_z)f_{\text{BCS}}$ to get

$$(\nabla - 2ie\mathbf{A})^2 f = -2i\frac{\epsilon}{D} f - \frac{\gamma}{L_z} f_{\text{BCS}}. \tag{3.4.9}$$

Writing this on finite difference form we get the same terms as in Eq. (3.1.5), as well as the extra term $-\frac{\gamma}{L_z} f_{\text{BCS}}$:

$$\begin{aligned} &f_{i+1,j}\left(\frac{1}{h_x^2} - 2ieA_{x,i,j}\frac{1}{h_x}\right) + f_{i-1,j}\left(\frac{1}{h_x^2} + 2ieA_{x,i,j}\frac{1}{h_x}\right) + f_{i,j+1}\left(\frac{1}{h_y^2} - 2ieA_{y,i,j}\frac{1}{h_y}\right) \\ &+ f_{i,j-1}\left(\frac{1}{h_y^2} + 2ieA_{y,i,j}\frac{1}{h_y}\right) = f_{i,j}\left(\frac{2}{h_x^2} + \frac{2}{h_y^2} + 4e^2\mathbf{A}_{i,j}^2 - 2i\frac{\epsilon}{D}\right) - \frac{\gamma}{L_z} f_{\text{BCS},i,j}, \end{aligned} \tag{3.4.10}$$

where we have added the subscripts $i, j$ to $f_{\text{BCS}}$ to specify that it varies with position $f_{\text{BCS},i,j} = f_{\text{BCS}}(x_i, y_j, \epsilon)$.

### 3.4.3 Vortex structure

When applying a magnetic field to a type II superconductor and creating vortices, this changes both the Green's function of the superconductor and the magnetic field and thus the vector potential. Inside the core of a vortex, which is a region of radius equal to the coherence length $\xi$, the magnetic field is approximately constant, while the superconductor goes to the normal metal state in the center. In the high-$\kappa$ approximation, one can show that the magnetic field as a function of the radius $r$ from the center of the vortex is [70]

$$\begin{aligned} B(r) &= \frac{\Phi_0}{2\pi\lambda^2}\ln(\kappa) \qquad r < \xi, \\ B(r) &= \frac{\Phi_0}{2\pi\lambda^2} K_0\left(\frac{r}{\lambda}\right) \qquad r > \xi, \end{aligned} \tag{3.4.11}$$

where $\Phi_0$ is the magnetic flux quantum, $\lambda$ is the London penetration depth, $\xi$ is the coherence length, $\kappa = \lambda/\xi$ is the Ginzburg-Landau parameter and $K_0$ is the zeroth order modified Bessel function of the second kind. According to Tinkham [70], in the Ginzburg-Landau theory, the superconducting wave function $\psi$ depends on the distance $r$ from the vortex core as

$$\psi \propto \tanh(\nu\frac{r}{\xi}), \tag{3.4.12}$$

where $\nu$ is a constant of order unity. As the wave function $\psi$ is proportional to the gap $\Delta$ we use

$$\Delta \propto \tanh(\nu\frac{r}{\xi}), \tag{3.4.13}$$

when calculating the Green's function in the superconductor.

When solving the linearized Usadel equation for a system with vortices we need the magnetic vector potential $\mathbf{A}$. To calculate this we can use Poincaré's lemma [74, 75]. For a general vector field $\mathbf{F}$ the vector potential $\mathbf{G}$ can be calculated as

$$\begin{aligned} G_x(x,y,z) &= \int_0^1 (tzF_y(tx,ty,tz) - tyF_z(tx,ty,tz))\,\mathrm{d}t, \\ G_y(x,y,z) &= \int_0^1 (txF_z(tx,ty,tz) - tzF_x(tx,ty,tz))\,\mathrm{d}t, \\ G_z(x,y,z) &= \int_0^1 (tyF_x(tx,ty,tz) - txF_y(tx,ty,tz))\,\mathrm{d}t. \end{aligned} \tag{3.4.14}$$

As we consider a magnetic field that points in the $z$-direction, this allows us to simplify the calculation of $\mathbf{A}$ greatly compared to the general form of Poincaré's lemma. This gives us

$$\begin{aligned} A_x(x,y,z) &= \int_0^1 -tyB_z(tx,ty,tz)\mathrm{d}t, \\ A_y(x,y,z) &= \int_0^1 txB_z(tx,ty,tz)\mathrm{d}t, \\ A_z(x,y,z) &= 0. \end{aligned} \tag{3.4.15}$$

Using these equations along with Eq. (3.4.11) for the magnetic field allows us to easily calculate the magnetic vector potential.

We will also consider cases where we have more than one vortex in the normal metal. The vortices then arrange themselves in a hexagonal lattice as shown by Kleiner et. al. [10] and this is the arrangement we will use. As the magnetic field and the vector potential respect the superposition principle, we can simply calculate the vector potential from each vortex independently and add them together.

### 3.4.4 Boundary conditions

As we now have vacuum surrounding the normal metal in the $x$ and $y$ directions we will not use Kuprianov-Lukichev boundary conditions. Instead, we use vacuum boundary conditions

$$\check{\mathbf{I}} \cdot \hat{\mathbf{n}} = 0, \tag{3.4.16}$$

where $\check{\mathbf{I}}$ is the matrix current defined in Eq (1.5.3) and $\hat{\mathbf{n}}$ is the normal vector of the normal metal-vacuum interface. Physically this boundary condition corresponds to no currents flowing out of the normal metal into the vacuum and is natural as vacuum does not conduct electricity, spin or heat. To simplify Eq. (3.4.16) in the linearized case, we start by writing out the matrix current using the linearized Green's function defined in Eq. (1.5.9):

$$\begin{aligned} \check{\mathbf{I}} &= \hat{\mathbf{g}}^R\tilde{\nabla}\hat{\mathbf{g}}^R = \hat{\mathbf{g}}^R(\nabla\hat{\mathbf{g}}^R - ie\mathbf{A}[\hat{\boldsymbol{\rho}}_3, \hat{\mathbf{g}}^R]_-) \\ &= (\hat{\boldsymbol{\rho}}_3 + \hat{\boldsymbol{f}})\left( \begin{bmatrix} 0 & \nabla f i\sigma^2 \\ -\nabla\tilde{f} i\sigma^2 & 0 \end{bmatrix} - 2ie\mathbf{A}\begin{bmatrix} 0 & f i\sigma^2 \\ \tilde{f} i\sigma^2 & 0 \end{bmatrix} \right). \end{aligned} \tag{3.4.17}$$

We now neglect terms that are second order in $f$ and take the dot product with $\hat{\mathbf{n}}$ to get

$$\check{\mathbf{I}} \cdot \hat{\mathbf{n}} \approx \begin{bmatrix} 0 & (\nabla f - 2ie\mathbf{A}f) \cdot \hat{\mathbf{n}} i\sigma^2 \\ (\nabla \tilde{f} + 2ie\mathbf{A}\tilde{f}) \cdot \hat{\mathbf{n}} i\sigma^2 & 0 \end{bmatrix}. \tag{3.4.18}$$

Just as in the case when we derived the linearized Usadel equation in section 1.5.1, we get two scalar equations and we can obtain one from the other by tilde conjugation. Thus, the vacuum boundary condition in the linearized case is

$$(\hat{\mathbf{n}} \cdot \nabla) f - 2ie(\mathbf{A} \cdot \hat{\mathbf{n}}) f = 0. \tag{3.4.19}$$

To use this numerically we want to write it on finite difference form. Therefore, we first assume that $\hat{\mathbf{n}} = \hat{\mathbf{x}}$, as the system we study will only have normal vector parallel or antiparallel to the $x$ or $y$ axis. This means that the boundary condition becomes

$$\partial_x f - 2ieA_x f = 0. \tag{3.4.20}$$

Using the finite difference form of the derivative (3.1.3), we then get a form of the boundary conditions that is easy to implement numerically

$$\frac{f_{i+1,j}}{2h_x} - \frac{f_{i-1,j}}{2h_x} - 2ieA_{x,i,j} f_{i,j} = 0. \tag{3.4.21}$$

### 3.4.5 Choice of material parameters

In Eqs. (3.4.9), (3.4.11) and (3.4.13) there are several free parameters that need to be determined. Just as we have done earlier we will measure all lengths relative to the coherence length $\xi$ and all energies relative to the energy gap in the superconductor $\Delta$. Thus we let $\epsilon \to \epsilon/\Delta$, $r \to r/\xi$, $L_z \to L_z/\xi$ and $\lambda \to \lambda/\xi$. This means that $\kappa = \lambda/\xi$ will be the same as $\lambda$. As this varies between materials, we will study a couple of different values of $\kappa$. We will first consider an isolated vortex using $\kappa = 2.71$ and $\kappa = 75$ to study two extremes. Then, we will study 7 vortices in a hexagonal lattice using $\kappa = 2.71$ and $\kappa = 10$. These values are not exact fits for any specific material but are rather representative of different types of type-II superconductors. For example, pure niobium has $\kappa \approx 1.4$ [76, 77], 50%Nb-50%Ta has $\kappa \approx 3.9$ [78], $MgB_2$ has $\kappa \approx 38$ [77, 79] and $YBa_2Cu_3O_7$ has $\kappa \approx$ 60-100 [79, 50]. In addition, the values of $\kappa$ for alloys depend on both the fabrication and the concentration of each element. The reason for $\kappa = 10$ was that a larger $\kappa$ requires a larger lattice size for adequate spacing between vortices. This was numerically infeasible for $\kappa > 10$. As the coherence length is defined as $\xi = \sqrt{D/\Delta}$ we now have that $D = \xi^2\Delta = 1$. We choose a moderate interface transparency of $\gamma = 0.3\xi$ and a thickness of the thin film of $L_z = \xi$. Because these two parameters enter the equation as $\gamma/L_z$ and they only appear in the one term not containing $f$, the value of them does not affect the form of the solution, only the magnitude. Specifically, as we have a linear equation for $f$ changing the only term not containing $f$ by some multiplicative constant means we can multiply $f$ by the same constant and still satisfy the equation.

To calculate the superconducting gap in Eq. (3.4.13) we need to decide the value of $\nu$. We use that according to Tinkham [70] $f_{\text{BCS}}$ fulfills the equation

$$f_{\text{BCS}} - f_{\text{BCS}}^3 - \xi^2 \left[ \left( \frac{1}{r} - \frac{2\pi\mathbf{A}}{\Phi_0} \right) f - \frac{1}{r} \frac{\mathrm{d}}{\mathrm{d}r} \left( r \frac{\mathrm{d}f}{\mathrm{d}r} \right) \right] = 0. \tag{3.4.22}$$

This equation was then solved numerically which gave $\nu \approx 0.8$ independent of the choice of $\kappa$ and this value was used for the numerical simulations. In the integral for the current density (1.5.21) we also need a cutoff frequency $\omega_c$ which was chosen to be $\omega_c = 30\Delta$. Finally, an imaginary part was added to the energy $\epsilon \to \epsilon + i\delta$, where $\delta$ was chosen to be $\delta = 0.01\Delta$. This takes into account the inelastic scattering measured by Dynes et al. [62] and regularizes the Green's function at energies $\epsilon$ close to the gap $\Delta$.

## 3.5 Thin film results

To solve the system with a thin film of normal metal on top of a superconductor numerically we implement Eq. (3.4.10) and Eq. (3.4.21) using the method described in Sec. 3.1.3. We study both an isolated vortex and 7 vortices in a hexagonal distribution to study the effect of a vortex lattice. The values of the material parameters chosen are explained in Sec. 3.4.5. In addition, all simulations were done at $T = 0$. We apply a voltage that leads to a two-step distribution function as explained in 1.2.6.

### 3.5.1 Isolated vortex

We start by studying an isolated vortex, i.e. there is only one vortex centered in the middle of the normal metal. This is the simplest case and would correspond to the limit of vortices that are separated by a long distance. In Fig. 3.8 the supercurrents in the normal metal are plotted for $\kappa = 2.71$, two different lengths $L = 10\xi$ and $L = 20\xi$ and for three different applied voltages $eV = 0$, $eV = 0.25\Delta$ and $eV = 0.5\Delta$. When there is no voltage applied, we see that the currents in the normal metal act in the same way as for a type-II superconductor, that is they increase the magnetic field in the middle of the vortex and reduce it further away, thus concentrating the magnetic field in a smaller area. When comparing $L = 10\xi$ and $L = 20\xi$, we see that there is not that big of a difference; the $L = 20\xi$ plot looks mostly like a zoomed-out version of the $L = 10\xi$ one. This is because most of the magnetic field is concentrated near the middle of the material. At $(x = 5\xi, y = 0)$ the magnetic field strength is already reduced to 23% of what it is in the middle and the pair correlation of the underlying superconductor has fully recovered. Thus, when we increase the size of the normal metal we only get a slight change in the supercurrents as there is only a small change in the magnetic field that affects the normal metal. It should be noted that the maximum value of the current densities is a bit higher for $L = 20\xi$ which is due to the fact that at $L = 10\xi$ the vacuum surrounding the normal metal cannot conduct currents. This means that currents close to the boundary get suppressed but this does not happen for $L = 20\xi$ as here the currents go to zero before getting close to the vacuum interface. When applying a voltage of $eV = 0.25\Delta$ we see that the current has been reversed in most of the normal metal, except for near the center of the vortex. This is due to the fact that the magnetic field decreases when moving away from the center, while the proximity-induced superconductivity increases. To explain this, we consider the spectral current density shown in Fig. 3.9. This is similar for $L = 20\xi$, only more stretched out, and therefore only $L = 10\xi$ has been included. To calculate the spectral current density we consider the $y$-component of the current at $y = 0$ and $x > 0$. As we see in Fig. 3.8 the current at $y = 0$ and $x > 0$ is representative of the entire normal metal, one more or less just has to rotate it. For the entire normal metal, the contribution to the paramagnetic response has an energy quite close to the superconducting gap, and while they become smaller further away from the vortex, they are qualitatively quite similar. However, the diamagnetic contributions have a larger variation with respect to position. There is always a strong diamagnetic contribution close to the Fermi level, however, contributions from higher energies are much more dependent on position. Near the center of the vortex, the area with diamagnetic contributions rapidly increases as the magnetic field is still quite large and the superconductivity recovers from being zero in

the middle. However, at about $x = 1.5\xi$ the region with a diamagnetic response reaches a maximum and starts to decrease. This coincides with when the superconductivity has recovered sufficiently to start setting up proper screening currents and the magnetic field has started to be shielded. After this, the diamagnetic contributions become more and more focused close to the Fermi level and we can more easily reverse them. Thus, when a small voltage is applied only the currents furthest away from the center will be reversed. As the voltage is increased more currents closer to the center will be reversed, allowing us to tune the extent of the paramagnetic response. With a sufficiently large voltage, such as $eV = 0.5\Delta$, Fig. 3.8 shows that all the supercurrents are reversed, both for $L = 10\xi$ and $L = 20\xi$. Thus, the normal metal now has a fully paramagnetic response to the magnetic field. We also see that for higher applied voltages the magnitude of the supercurrents is more than an order of magnitude smaller than without an applied voltage, which shows us that most of the response to the magnetic field is due to current contributions with energies very close to the Fermi level as we see from the spectral current density in Fig. 3.9. In addition, the size of the currents is larger for $eV = 0.5\Delta$ than for $eV = 0.25\Delta$. This is because at $eV = 0.25\Delta$ the diamagnetic and paramagnetic response compete, whereas increasing the applied voltage to $eV = 0.5\Delta$ suppresses the diamagnetic response.

To see the magnetic fields produced from the currents in the normal metal in the case where $L = 10\xi$ we consider Fig. 3.10. At the top left panel is the magnetic field emanating from the Abrikosov vortex in the underlying superconductor. We call this the applied field as it is the field that enters the normal metal region from outside the normal metal. The other three panels show the magnetic fields produced from the supercurrents in the normal metal for three different applied voltages $eV = 0$, $eV = 0.25\Delta$ and $eV = 0.5\Delta$. When we do not apply any voltage we see that the normal metal response mirrors that of the underlying superconductor, that is we have a diamagnetic response. When we then apply a voltage of $eV = 0.25\Delta$ we get the mixed response we also saw from the currents. Here it is clear that only a small area in the center remains diamagnetic while the rest becomes paramagnetic. We also see that there is a larger area where there is a change in the magnetic field that is of the same order as at the center when compared to no applied voltage. This is, however, due to the fact that the induced magnetic field in the center is very weak. When we compare to the case when we apply a voltage of $eV = 0.5\Delta$, we see that we now have flipped the entire magnetic field response to be paramagnetic and thus it is the opposite of the case without applied voltage. We also see that the strength of the induced field is about an order of magnitude lower than the case without an applied voltage, showing that the paramagnetic response is much weaker.

So far we have considered $\kappa = 2.71$, but to show that we have the same reversal of the supercurrents for larger $\kappa$, Fig. 3.11 shows the supercurrents for $\kappa = 75$, $L = 20\xi$ and three different applied voltages $eV = 0$, $eV = 0.25\Delta$ and $eV = 0.5\Delta$. Without any applied voltage the currents look quite similar to the $L = 10\xi$, $\kappa = 2.71$ case without any applied voltage, just more spread out. This is because with such a large value of $\kappa$ as 75, the magnetic field takes a very long distance to decrease to small values, and at the edge, the value of the applied magnetic field is still more than 80% of what it is in the center. Even with this almost constant magnetic field we still start to get a reversal when applying a voltage as we see with $eV = 0.25\Delta$, which looks very much like the same voltage for $L = 10\xi$ and $\kappa = 2.71$. Only a small area near the center still remains diamagnetic while the rest has switched to a paramagnetic response. The similarity with

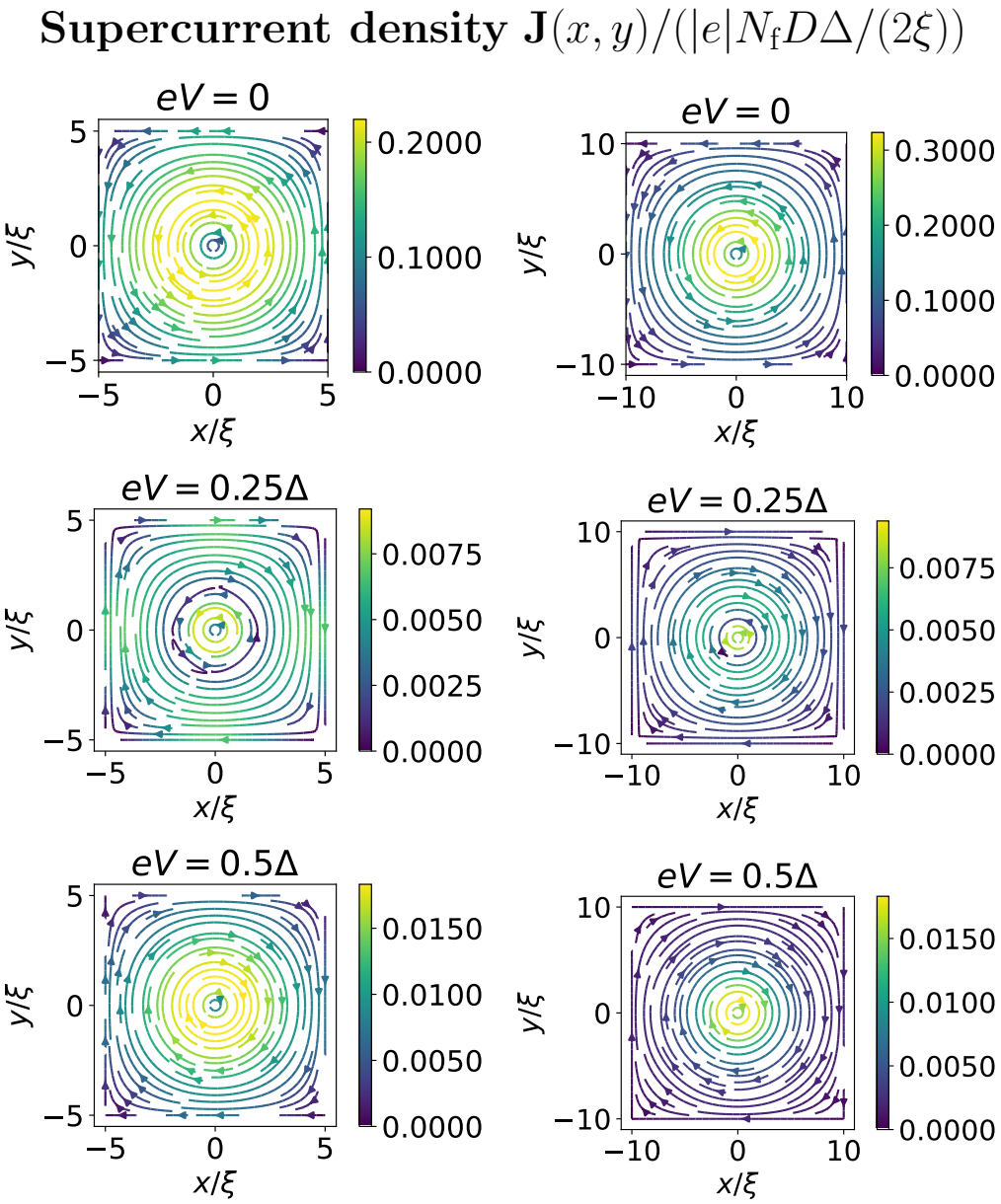


Figure 3.8: Streamplots of the current density $\mathbf{J}(x,y)/(|e|N_\mathrm{f}D\Delta/(2\xi))$ for 1 vortex with $\kappa = 2.71$. The left column shows $L = 10\xi$ and the right column $L = 20\xi$. As most of the magnetic field and all of the pair correlation damping is contained within a radius $r = 5\xi$, there is not that big of a difference between the two cases and $L = 20\xi$ is almost like a zoomed-out version of $L = 10\xi$. In the case without applied voltage, the edges of the normal metal reduce the size of the currents in the $L = 10\xi$ case compared to $L = 20\xi$. When applying a voltage of $eV = 0.25\Delta$, most of the current is reversed, but not in the region closest to the center of the vortex. For $eV = 0.5\Delta$ we see that all currents are reversed and we have a fully paramagnetic response for the normal metal.

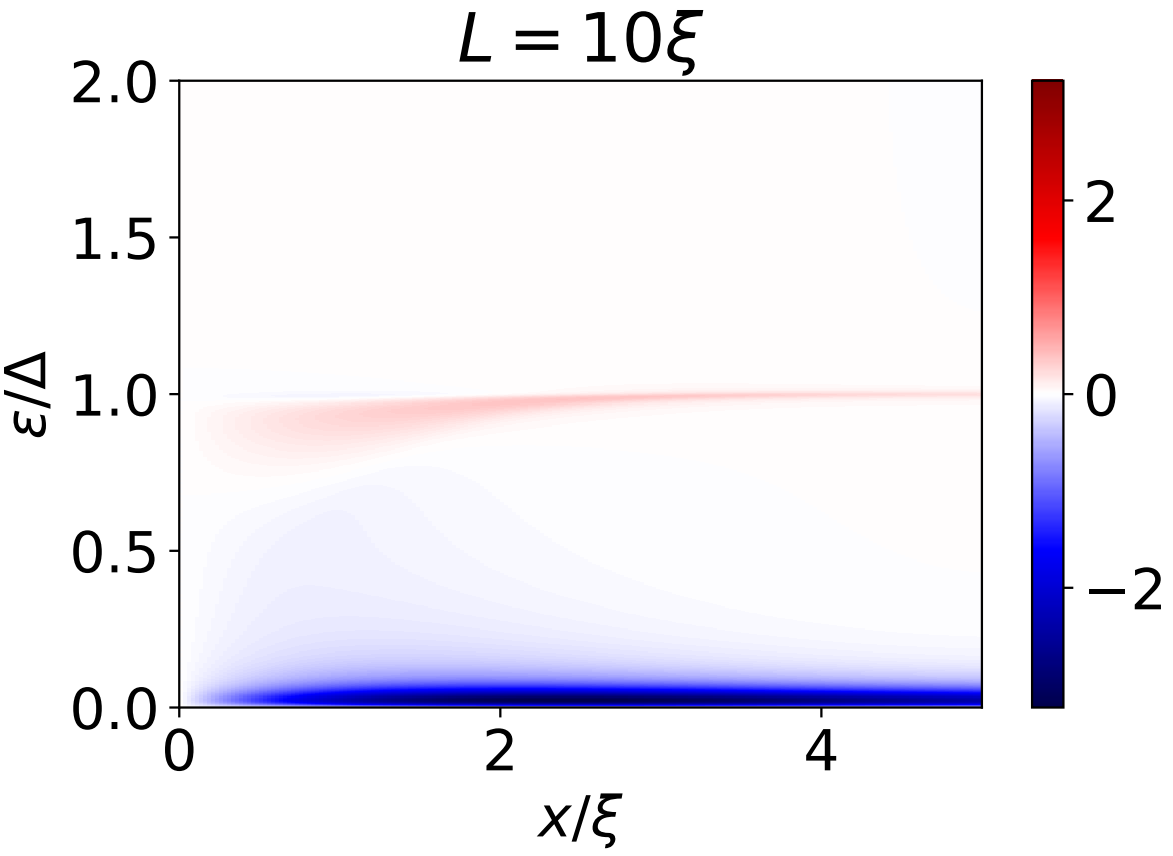


Figure 3.9: Spectral current density $J_y(x, y = 0, \epsilon)/(|e|N_f D\Delta/\xi)$. The diamagnetic contributions to the response, in blue, are large close to the Fermi energy. There is also a considerable paramagnetic contribution close to the superconducting gap. In addition, a slight diamagnetic contribution is more dependent on position, it is quite large near the center of the vortex and decreases with the distance from the center. This contribution leads to a different voltage needing to be applied to reverse the current at different distances from the center of the vortex.

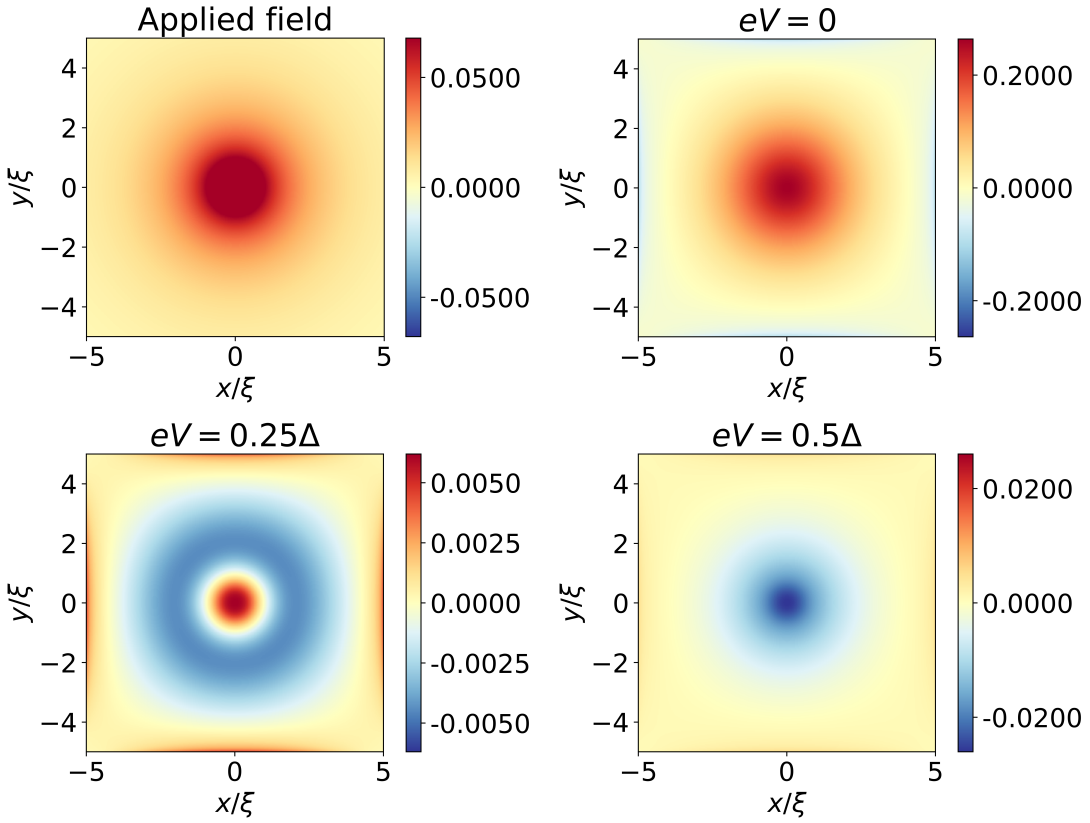


Figure 3.10: Applied magnetic field, $B(x, y)/(1/(|e|\xi))$, at the top left and induced magnetic field, $B_{\text{ind}}(x, y)/(|e|\mu_0 N_{\text{f}} D\xi L_z/2)$, at 3 different applied voltages for an isolated vortex with $L = 10\xi$ and $\kappa = 2.71$. Both the applied magnetic field and the induced magnetic field point in the $z$-direction. We see that without any applied voltage, the currents in the normal metal induce a magnetic field mirroring that of the vortex in the superconductor below. Thus, we still have a normal diamagnetic Meissner effect. When applying a voltage of $eV = 0.25\Delta$ we see that more of the magnetic field points in the opposite direction due to the supercurrents having been reversed in these areas. However, close to the center of the vortex we still have a diamagnetic Meissner effect showing that it is harder to flip the magnetic field response close to the center of the vortex. Finally, for $eV = 0.5\Delta$ we see that all the magnetic field points in the opposite direction of the one coming from the superconductor, i.e. we have a fully paramagnetic Meissner effect.

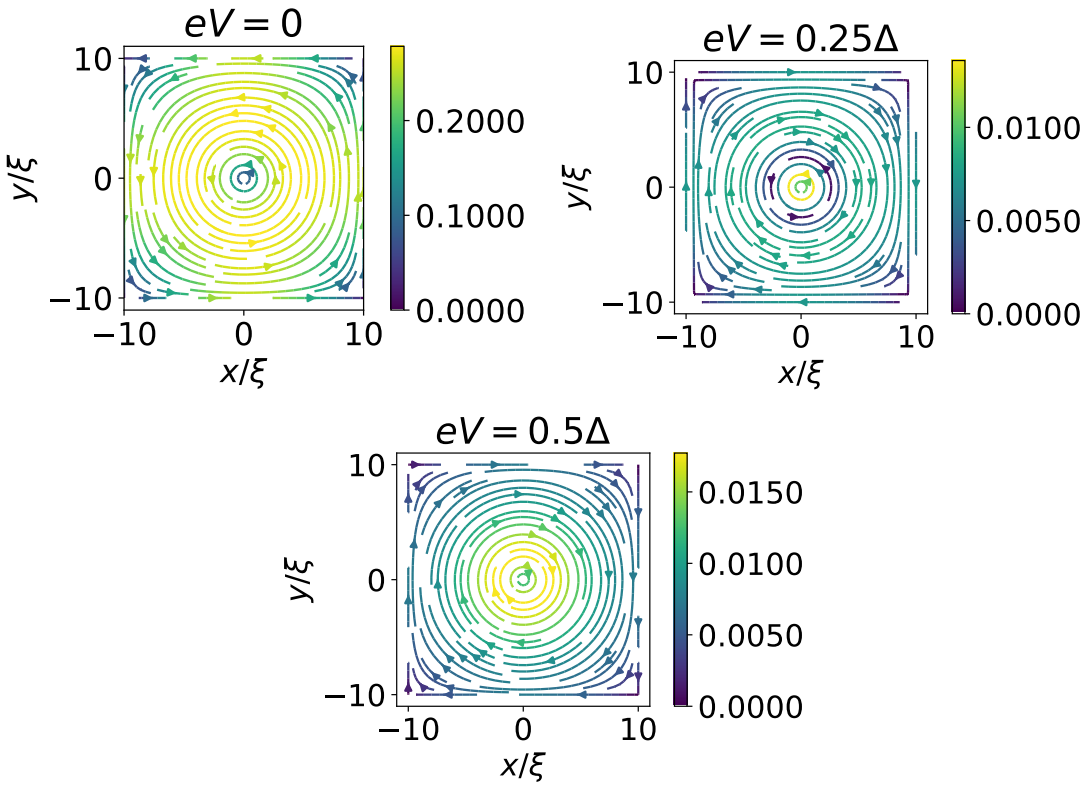


Figure 3.11: Streamplots of the current density $\mathbf{J}(x,y)/(|e|N_f D\Delta/(2\xi))$ for an isolated vortex with $L = 20\xi$ and $\kappa = 75$. We see that the current density without an applied field mirrors that of a normal vortex, however, the finite size of the normal metal restricts the currents from flowing further out. This restriction is also clear when we apply a voltage, however, we do get a partial reversal of the current for $eV = 0.25\Delta$ and a full reversal of the current for $eV = 0.5\Delta$.

$L = 10\xi$ and $\kappa = 2.71$ also continues for $eV = 0.5\Delta$, where the entire normal metal has switched to a paramagnetic response. Thus, we see that even with two values of $\kappa$ that are this different, we still get a very similar response both with and without an applied voltage. The only difference being that the size of the normal metal has to increase to observe the same currents when $\kappa$ increases. Based on this, most type-II superconductors should allow one to experimentally observe a paramagnetic Meissner response as there is only a weak dependence on the value of $\kappa$.

To study how easily one can switch from a diamagnetic to a paramagnetic response in the normal metal we define a switching voltage $eV_s$. Just as for the cases where we had the superconductor surrounding the normal metal, we define it as the voltage at which the total current circulating around the vortex crosses 0. Fig. 3.12 shows the switching voltage $eV_s$ as a function of the length of the normal $L$ for $\kappa = 2.71$. We see that the switching voltage is relatively large for $L$ close to $4\xi$ but decreases quite rapidly as $L$ increases. This is because the region closest to the center of the normal metal is the region that needs the largest voltage to reverse the currents as we saw in Figs 3.8 and 3.11. When the size is increased, there is a larger area that is easier to reverse and thus the necessary voltage

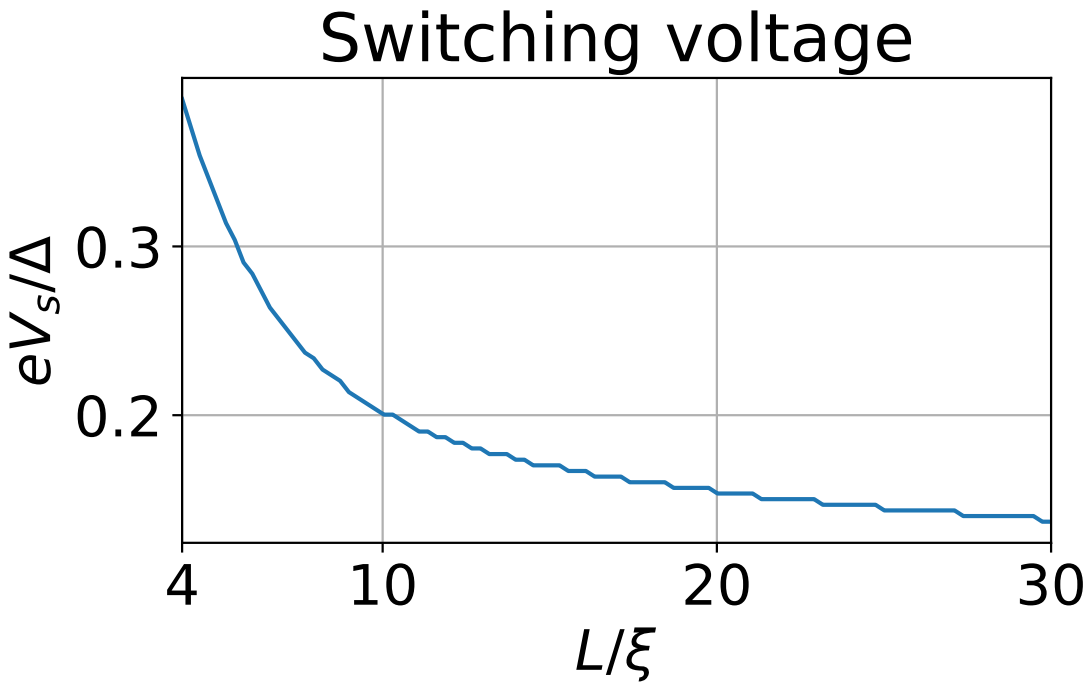


Figure 3.12: Switching voltage $eV_s/\Delta$ as a function of the length of the normal metal $L/\xi$ for an isolated vortex with $\kappa = 2.71$. We see that the switching voltage is relatively large for small systems as here the currents close to the center also have to be reversed. When the system size increases the switching voltage drops as it is easier to reverse currents further from the center of the vortex. We also see a flattening out for larger $L/\xi$ due to there being very little current that flows so far from the vortex.

is reduced. However, when the size is increased even further, especially past $L = 10\xi$, the switching voltage starts to flatten out. This is because at these sizes there is less and less magnetic field to screen close to the edge and thus the currents out there are very small as we saw for $L = 20\xi$, $\kappa = 2.71$. Increasing the size of the normal metal thus only adds very small currents. Even though these are easy to reverse one still has to reverse more or less the same amount of current close to the center, thus leading to a small change in the switching voltage.

While the screening currents in a thin film of normal metal on top of a superconductor is our main focus here, there are also other interesting properties to study for this geometry. Stolyarov et al. [73] studied how the size of a vortex changed in a thin film of normal metal on top of a superconductor when compared to the bulk superconductor. They found that the size of the vortex cores was about 4 times larger in the normal metal than the superconductor. While we do not make exact comparisons here, we show in Fig 3.13 how the pair correlation recovers when moving away from the vortex core for $\kappa = 2.71$ and $\kappa = 75$. In both cases, the pair correlation recovers proportional to a $\tanh(\nu r/\xi)$ which is also what was assumed in the superconductor with $\nu = 0.8$. In the normal metal, we see that this recovery is quite a bit slower, and a value of $\nu = 0.35$ fits quite well in both cases.

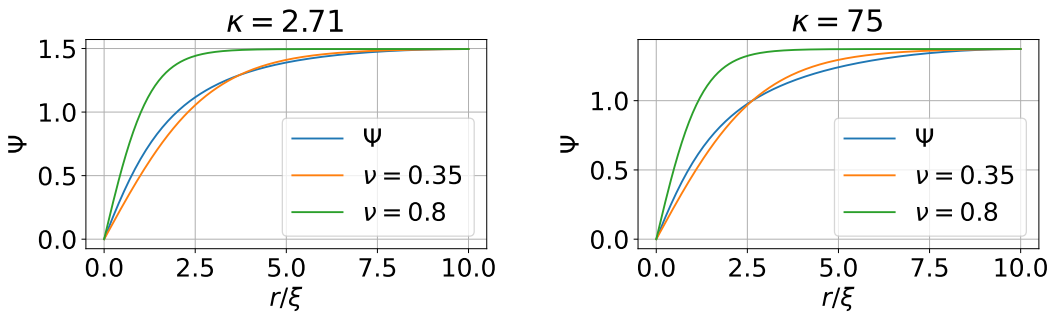


Figure 3.13: The value of the pair correlation as a function of the distance to the core for an $L = 20\xi$ normal metal with $\kappa = 2.71$ in the left plot and $\kappa = 75$ in the right plot. We see that in both cases the value of the pair correlation in the normal metal in blue matches well with a recovery rate corresponding to $\nu = 0.35$ in the normal metal. This is about half the value of the superconductor where $\nu = 0.8$

Thus we also have an expansion of the vortex core in the normal metal when compared to the superconductor. While our expansion is not as drastic, being only 2 times instead of 4, this is due to the fact that we consider a thin film of normal metal, while Stolyarov et al. considered a relatively thick normal metal. The induced superconductivity is still rather large in our case, while for a thicker normal metal, it would be weaker and larger areas will have their superconductivity destroyed by the magnetic field.

### 3.5.2 Vortex lattice

While a weak magnetic field applied to a superconductor will lead to approximately isolated vortices as has been discussed until now in this section, we will now study 7 vortices in a hexagonal layout to see the effect of a vortex lattice on reversing the screening currents. To make it closer to a realistic large-scale vortex lattice, the magnetic field $\mathbf{B}(x, y)$ and the reduction of the superconducting gap $\Delta(x, y)$ were calculated from 105 vortices, i.e. all vortices within a square of side length 70, where the 7 in the figures are located in the middle of this lattice. In the calculations of the switching voltage, these extra vortices were not included due to longer computation time. The results still match up well, and in the limit of isolated vortices, they match exactly.

In Fig. 3.14 we have plotted the current density in a normal metal with side lengths $L = 20\xi$ for $\kappa = 2.71$ and $\kappa = 10$ for three different applied voltages $eV = 0$, $eV = 0.25\Delta$ and $eV = 0.5\Delta$. The distance between each vortex is $7.5\xi$, which means that the vortices are almost isolated for $\kappa = 2.71$, while there is a big overlap in the magnetic field for $\kappa = 10$. The magnetic field from the superconductor below the normal metal has been calculated for a grid of size $70\xi \times 70\xi$ to include the entire magnetic field coming from the vortices penetrating the superconductor, including the field leaking from vortices further away. Without any applied voltage we see that the currents in the normal metal mirror the ones in a type-II superconductor. They try to contain the magnetic field within a small cylindrical area and screen the rest of the normal metal from the magnetic field. Even with a sizeable difference in the magnetic field, the current distribution for $\kappa = 10$ is very similar to $\kappa = 2.71$ due to the similarities of the vortex lattice of the underlying

superconductor. When we increase the voltage we see that the currents in the middle of the central vortex still are diamagnetic, while the currents a bit further out are reversed. This is consistent with what we saw in the isolated vortex case, where the reversal of the current started far away from the center and then gradually moved closer to the center when the voltage was increased. For the 6 surrounding vortices, we see that there is still a small paramagnetic screening current, but here the edges and the other surrounding vortices restrict them from reversing the currents a bit further away from the center of each of the vortices. On the inner side the currents have to compete with the ones from the central vortex and are in this way suppressed, while there are still currents flowing on the outside as there are no other vortices creating currents they have to compete with here. Thus, we see the importance of edge effects, had we increased the size of the normal metal to remove these effects the surrounding vortices should look more like the middle vortex, which is only affected by the other vortices and not the edges. If we finally increase the voltage to $eV = 0.5\Delta$ we see a full reversing of the screening currents, both for $\kappa = 2.71$ and $\kappa = 10$. This happens for all vortices and we also see that now the surrounding vortices are much more pronounced than for $eV = 0.25\Delta$. This shows that now there is not as big of a competition between paramagnetic and diamagnetic response as there was in the $eV = 0.25\Delta$ case and that the vortices are thus less affected by edge effects. Thus even in a relatively tightly packed lattice of vortices, we can still have a reversal of the screening currents in the normal metal.

In addition to the supercurrents, we can also directly study the magnetic field induced by these currents. Fig. 3.15 shows the magnetic field coming from the superconductor calculated from a grid of size $70\xi \times 70\xi$ which contains 105 vortices, what we have called the applied field $B(x, y)/(1/(|e|\xi))$, and the magnetic field induced by the supercurrents in the normal metal $B_{\text{ind}}(x, y)/(|e|\mu_0 N_{\text{f}} D\xi L_z/2)$ for 5 different applied voltages, $eV = 0$, $eV = 0.15\Delta$, $eV = 0.25\Delta$, $eV = 0.35\Delta$ and $eV = 0.5\Delta$. The underlying superconductor has Ginzburg-Landau parameter $\kappa = 2.71$, while the normal metal has side lengths $L = 20\xi$. We see that the magnetic field from the superconductor is concentrated in 7 vortices laid out hexagonally, but there is still a lot of field leaking out into the entire superconductor. If we consider the induced field without any applied voltage, we see that the normal metal has the same response as a type-II superconductor, i.e. it tries to contain the magnetic field inside the vortices and screen the rest of the material from the magnetic field. When we apply a voltage of $eV = 0.15\Delta$ we still see the same type of response, but the induced magnetic field is now much weaker, showing that most of the screening is done by modes with energy close to the Fermi energy. Increasing the applied voltage to $eV = 0.25\Delta$, we start to see a competition between diamagnetic and paramagnetic response. Just as we saw for the supercurrents in Fig. 3.15, the magnetic field close to the middle of the vortices still shows a response mirroring the superconductor, however, a bit away from the center this is no longer the case. For the central vortex, we see that here the induced field is reversed, showing a change towards a paramagnetic response. The surrounding vortices show a bit of a different behaviour at this voltage. Here, only the outer area close to the edge shows a reversing of the induced magnetic field, while the inner side closer to the middle vortex does not. This is due to currents on the inner side having to compete with the central vortex, while the outer ones do not, so there is little induced magnetic field on the inner side. If we increase the applied voltage further to $eV = 0.35\Delta$, we see that we have now fully switched the structure of the induced field. It

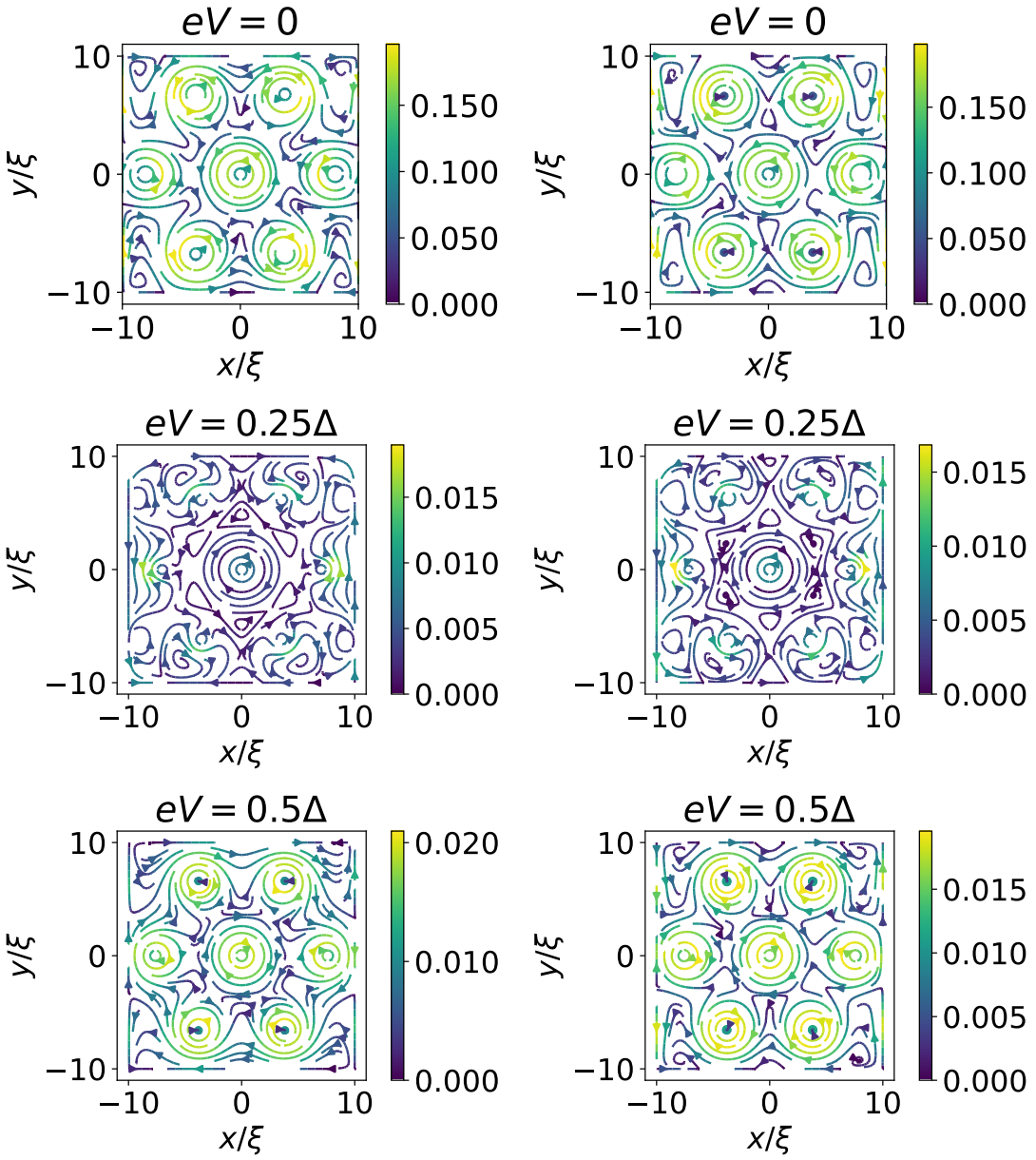


Figure 3.14: Streamplots of supercurrent density for 7 vortices with $L = 20\xi$ for three different applied voltages $eV$. The left column is with $\kappa = 2.71$ while the right column has $\kappa = 10$. We observe that without any applied voltage, both values of $\kappa$ show a very similar current distribution with them mirroring the vortex from the underlying superconductor and each vortex being more or less isolated from the others. For $eV = 0.25\Delta$ we see that the current in the central vortex flows in the same direction as without any voltage, however, further out the direction is reversed. For the outer vortices, we see that almost the entire vortex structure is lost, only a small part very close to the center of each vortex has a loop of current. This is due to the applied voltage being very close to the voltage needed to switch the current and due to them being close to the edges. For $eV = 0.5\Delta$ all vortices are reversed and show a paramagnetic response.

now tries to expel the magnetic field from the vortices and spread it more equally in the entire normal metal. However, the induced field is now extra weak due to the competition between the paramagnetic and diamagnetic responses. To increase the strength of this response a bit, we can increase the applied voltage to $eV = 0.5\Delta$. This more than doubles the strength of the induced magnetic field, but it is still about five times weaker than the case without an applied voltage. We also see that the reversed vortices are more closely localized at the vortices from the superconductor, which reduces the edge effects.

Finally, we want to consider what voltages need to be applied for the magnetic field response to be reversed. To do this we define the switching voltage $eV_s$ as the voltage needed to flip the sign of the induced magnetic field in the middle of the normal metal. It should be noted that this is a bit different than the definition used earlier, however, it is harder to consider how much current circulates around each vortex in a lattice and easier to consider the magnetic field. To be able to compare the 7 vortices with an isolated vortex, we also found the switching voltage for an isolated vortex with this definition. Finally, it should be noted that we now only include the magnetic field and superconducting gap reduction from the 7 vortices, and not the 105 vortices used in earlier calculations due to computation time. However, the results are still in good agreement with each other.

Fig 3.16 shows the switching voltage for 1 isolated vortex and 7 vortices in a hexagonal arrangement as functions of the length of the normal metal $L$ for a Ginzburg-Landau parameter $\kappa = 2.71$. For the isolated vortex, we see that the switching voltage is reduced when increasing the size from $L = 4\xi$ until about $L = 8\xi$ and quickly flattens out after this. This is because there is only one vortex and the only change when increasing the size is the reduction of edge effects. As we saw for the isolated vortex, the edges had little effect even at $L = 10\xi$. When increasing the size further, the small currents that appear far away have almost no effect on the sign of the magnetic field in the middle of the vortex. The curve for the switching voltage is more interesting for the 7 vortices. $eV_s$ is quite small for $L = 4\xi$ and then increases rapidly until about $L = 10\xi$ where it is reduced slowly until it matches the single isolated vortex at about $L = 20\xi$. In the 7 vortex lattice, the distance between the vortices is $(3/8)(L/\xi)$. As the vortices have a core of radius $\xi$ where the magnetic field is constant, we need at least a length of $L = 16/3\xi$ to avoid the vortex cores overlapping. Thus, the reason for the low switching voltage at $L = 4\xi$ is that at this size we basically have only a giant vortex in the entire normal metal. This means that the induced superconductivity is very weak and the magnetic field density is high, so switching from the diamagnetic response of the superconductor to the paramagnetic response requires a relatively low voltage. When the length increases from $L = 4\xi$ the magnetic field density is reduced and the induced superconductivity is increased, thus increasing the switching voltage. With this increase in size, we also move more towards a lattice arrangement of the 7 vortices. At $L = 10\xi$ we see that the switching voltage flattens out and starts to be reduced when increasing $L$ further. This is because at this point we have fully transitioned to a lattice configuration. When we then increase the normal metal length further, we reduce the effects the surrounding vortices have on the middle vortices and thus the required voltage to switch the response is reduced. We can also see that the voltage to switch the response in the lattice layout for $L = 10\xi$ is quite a bit larger than the required voltage for the isolated vortex. As the distance between each vortex for this length is $(15/8)\xi$, and assuming that the central vortex is restricted to about half the area between it and the surrounding vortices it is approximately restricted

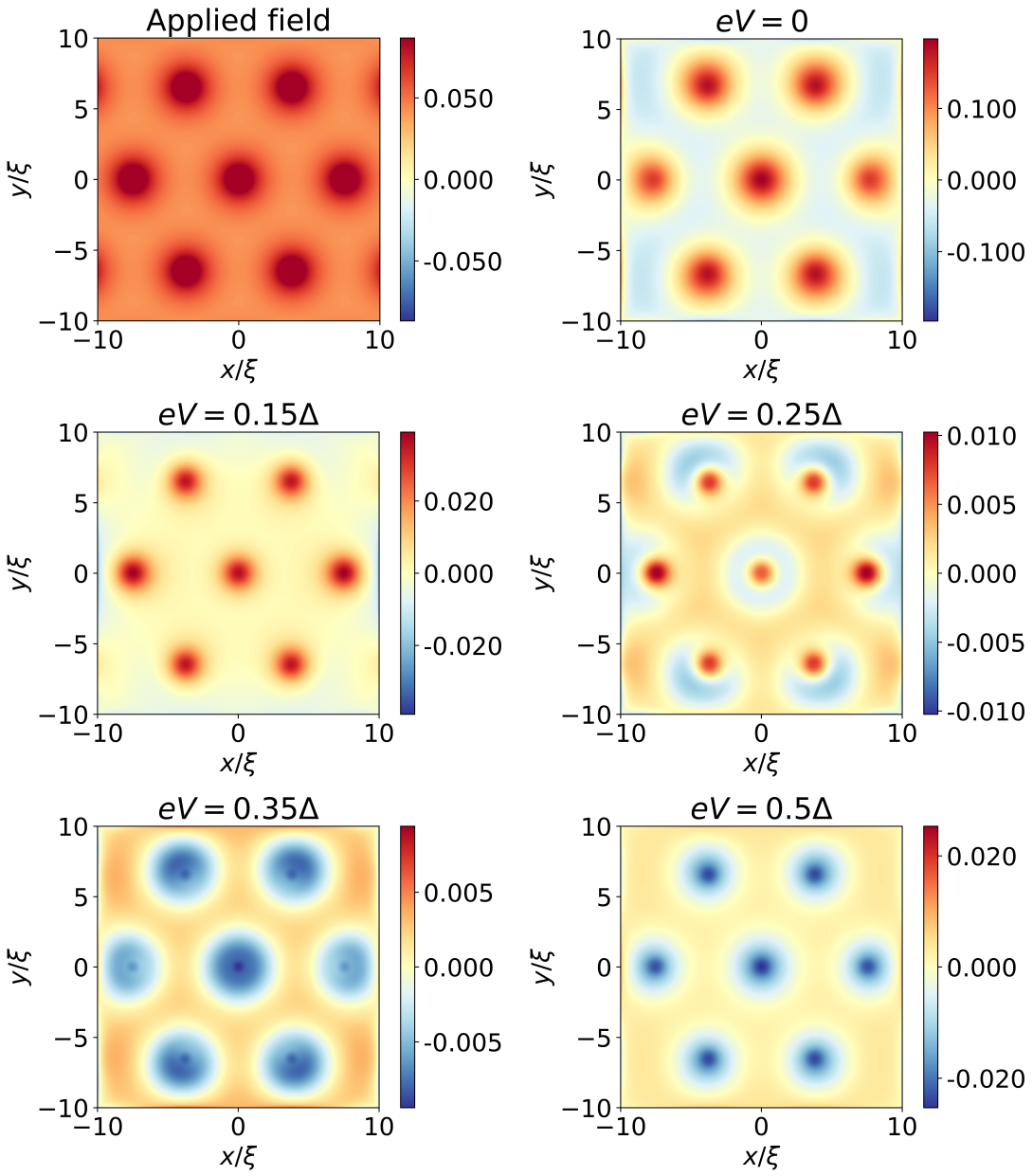


Figure 3.15: Applied magnetic field, $B(x,y)/(1/(|e|\xi))$, at the top left and induced magnetic field, $B_{\text{ind}}(x,y)/(|e|\mu_0 N_{\text{f}} D\xi L_z/2)$, for 5 different values of the applied voltage $eV$ for 7 vortices with $L = 20\xi$ and $\kappa = 2.71$. The applied field is the magnetic field coming from the underlying superconductor and a grid of size $70\xi \times 70\xi$ has been used to include magnetic field leaking. We see that the applied field is concentrated in 7 vortices, however, a lot still leaks into the rest of the material. Without any applied voltage, we see that the induced magnetic field mirrors the applied field, it concentrates the magnetic field into vortices. Increasing the voltage to $eV = 0.15\Delta$ we still have this same diamagnetic response, however, it is much weaker. For $eV = 0.25\Delta$ we have a clear competition between the paramagnetic and diamagnetic response, with only the middle of each vortex being diamagnetic. At $eV = 0.35\Delta$ we have switched to a fully diamagnetic response. However, there is still competition between the diamagnetic and paramagnetic response as increasing the voltage to $eV = 0.5\Delta$ increases the magnitude of the induced field.

to a hexagon with side length $15/8\xi$. This means that it is restricted to an area quite similar to the square of side length $L = 4\xi$, and it should have a switching voltage which is also quite similar to the isolated vortex in that square. From the plot we see that the switching voltage for the $L = 4\xi$ isolated vortex and the $L = 10\xi$ 7 vortex layout are very similar, supporting this argument. The side length of the hexagon the middle vortex is restricted to grows at half the rate of the side length $L$ and thus the drop-off in switching voltage should also be about half that of the isolated vortex case and this can also be seen from the plot. While the isolated vortex uses about $4\xi$-$5\xi$ from $L = 4\xi$ to flatten out at about $L \approx 8\xi$-$9\xi$, the 7 vortex configuration flattens out at about $L = 20\xi$, which means the size increase was $10\xi$ and is about double that of the isolated vortex. This flattening out is where the vortices start to be isolated and their switching voltage is not affected by the edges or the distance to other vortices. Thus, at a spacing of about $8\xi$ between the center of the vortices in the normal metal, we can start to treat the vortices as independent when the underlying superconductor has $\kappa = 2.71$. For larger values of $\kappa$, this spacing needs to be larger for them to be treated as independent, as the magnetic field from each vortex is spread out over a larger region. However, this only considers the qualitative magnetic field response of the center of the vortex, so the actual distance at which they can be treated as isolated should be larger as the screening currents furthest away from the core could still affect other vortices for larger spacings. If we consider the screening currents of a single $\kappa = 2.71$ vortex in Fig. 3.8, we see that the currents start to be negligible at a distance of about $9\xi$ from the core, which means that a distance of $18\xi$ should be sufficient. This is only a factor of 2 larger than what was derived from the switching voltage, which is a small difference.

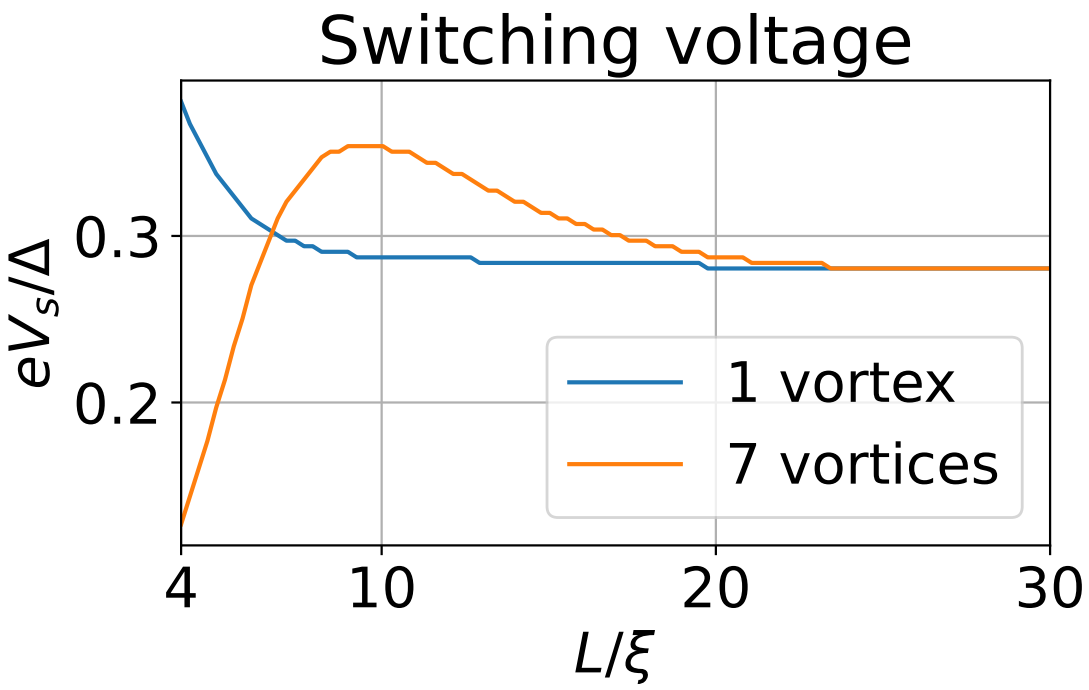


Figure 3.16: Switching voltage $eV_s/\Delta$ for an isolated vortex and for 7 vortices in a hexagonal arrangement, for varying lengths $L$ of the normal metal. We see that for the isolated vortex, the switching voltage is largest for a small normal metal where the edge effects play a role and stabilize when the size of the normal metal gets large enough to not affect the vortex. For a small normal metal with 7 very tightly packed vortices the switching voltage is quite small and much smaller than the isolated vortex in a normal metal of the same size. This is because at this tight packing of vortices, it is almost like a single giant vortex where the superconductivity is suppressed a lot and thus it is much easier to reverse the currents to a paramagnetic response. When the size increases, the switching voltage increases until about $L = 10\xi$. This increase is due to the vortices being more separated and it looks less like a giant vortex. We also see that the switching voltage is larger than for the isolated vortex. This is due to the surrounding vortices making the area the vortex is confined in smaller than for an isolated vortex for the same size of the normal metal. When the size gets very large the vortices get completely isolated. Thus, the surrounding vortices and the edges do not contribute and the switching voltage becomes constant.

# Chapter 4

# Summary and outlook

In this thesis, we have studied the Meissner response of a proximitized normal metal with superconducting vortices when driven out of equilibrium through injection of quasiparticles which are controlled by an external voltage. This has been done by solving the linearized Usadel equation and we considered three different geometries. First, we considered a cylinder of normal metal with a superconductor surrounding it in Chapter 2, then a square surrounded by a superconductor in Secs. 3.2-3.3 and finally a thin film of normal metal placed on top of a type-II superconductor in Secs. 3.4-3.5.

For the cylindrical geometry, we started by finding an analytical solution for the Green's function in the normal metal. Here we studied both a case without an applied magnetic field, where a current in the surrounding superconductor gives a phase to the system and a case with an applied magnetic field that was constant within the normal metal. We then continued by studying how the screening of the magnetic field was in the normal metal and how this was changed by driving the system out of equilibrium. We found that in equilibrium, we had a normal diamagnetic Meissner response, trying to concentrate the magnetic field in the center like in a type-II superconductor, but when driven out of equilibrium, we saw that the areas closer to the middle of the cylinder changed their response. This middle area tried to expel the magnetic field from the center and distribute it in the rest of the material, i.e. a paramagnetic Meissner effect. We showed that this was dependent on the size of the normal metal cylinder and that this was due to a lot of the diamagnetic screening currents being conducted by electrons very close to the Fermi level when the system was larger than the coherence length of the Cooper pairs.

Afterwards, we solved the linearized Usadel equation numerically for a square of normal metal surrounded by a superconductor. We first considered the case without any applied magnetic field, however, a supercurrent flowing in the surrounding superconductor induces a phase in the Green's function. Depending on the phase, we saw that in this case we can create giant vortices and antivortices recreating the results of Amundsen et al. [26]. When applying a magnetic field, we showed that driving the system out of equilibrium could reverse the magnetic response from a standard diamagnetic Meissner vortex response, where the currents contain the magnetic field in a small area, to an opposite paramagnetic Meissner response where they try to expel the magnetic field from the middle of the vortex.

Finally, for the thin film of normal metal placed on top of a type-II superconductor,

we considered both a single isolated vortex and 7 vortices in a hexagonal lattice. For the isolated vortex, we showed that driving the system out of equilibrium reverses the screening current in the vortex and that this has a very weak dependence on the Ginzburg-Landau parameter $\kappa$. The screening currents further from the center required a smaller voltage to reverse than those in the middle, which allows one to tune the extent of the paramagnetic response. In addition, we showed that the pair correlation recovers slower in the normal metal, leading to an increase in the size of the vortices, recreating qualitatively the results of Stolyarov et al [73]. For the 7 vortices, we showed that we can reverse the screening currents of each vortex, even when quite a bit of the magnetic field leaks into the area of the surrounding vortices. In addition, we showed that the surrounding vortices reduce the available space for each vortex making it harder, but still possible, to reverse them if they are tightly packed. When the distance between them is increased they effectively become isolated vortices with the same response to a magnetic field as was found in the isolated case.

Thus, we see that reversing the magnetic field response of a normal metal by driving the system out of equilibrium is possible for all three geometries we have studied. As this is present in all three geometries, we expect it to be a general response of the normal metal and not limited to the few cases we studied here. To observe this effect experimentally, all of the systems studied here can be considered. However, the thin film of normal metal is likely the easiest to realize experimentally, and one can in addition study the effect of varying the vortex density easily by varying the applied magnetic field. To drive the system out of equilibrium we recommend a quasiparticle injector using the design explained by Ouassou et al. [39], based on the design from Pothier et al. [48]. To measure the effect one can for example use magneto-optical imaging to directly measure the change in the magnetic field and consider how this changes when the voltage of the quasiparticle injector is changed.

Further studies can consider studying the systems with fewer assumptions. For example, one can include the inverse proximity effect, especially in the cylindrical case where one still gets an effective one-dimensional problem. For the thin film, this would lead to a three-dimensional problem, however, it would be interesting to see how the reversal of the vortices in the normal metal would affect the vortices in the superconductor. Systems with spin-active interfaces or magnetic components would also be of interest, as one could study how the odd-frequency components present in those systems would respond to being driven out of equilibrium, and if this can favour either the singlet or triplet component. Finally, testing the results from this thesis experimentally would be of interest to verify non-magnetic ways of reversing the Meissner effect.

# Bibliography


[1] H. K. Onnes, Leiden Comm. **120b, 122b, 124c** (1911).

[2] W. Meissner and R. Ochsenfeld, Die Naturwissenschaften **21**, 787 (1933).

[3] F. London and H. London, Proceedings of the Royal Society of London. Series A - Mathematical and Physical Sciences **149**, 71 (1935).

[4] L. D. Landau and V. L. Ginzburg, Soviet Physics JETP **20**, 1064 (1950).

[5] E. Maxwell, Physical Review **78**, 477 (1950).

[6] C. A. Reynolds, B. Serin, W. H. Wright, and L. B. Nesbitt, Physical Review **78**, 487 (1950).

[7] A. Abrikosov, Journal of Physics and Chemistry of Solids **2**, 199 (1957).

[8] J. Bardeen, L. N. Cooper, and J. R. Schrieffer, Physical Review **108**, 1175 (1957).

[9] J. G. Bednorz and K. A. Müller, Zeitschrift für Physik B Condensed Matter **64**, 189 (1986).

[10] W. H. Kleiner, L. M. Roth, and S. H. Autler, Physical Review **133**, A1226 (1964).

[11] D. Cribier, B. Jacrot, L. Madhav Rao, and B. Farnoux, Physics Letters **9**, 106 (1964).

[12] W. Fite and A. G. Redfield, Physical Review Letters **17**, 381 (1966).

[13] L. F. Chibotaru, A. Ceulemans, V. Bruyndoncx, and V. V. Moshchalkov, Nature **408**, 833 (2000).

[14] I. V. Grigorieva, W. Escoffier, V. R. Misko, B. J. Baelus, F. M. Peeters, L. Y. Vinnikov, and S. V. Dubonos, Physical Review Letters **99**, 147003 (2007).

[15] R. Holm and W. Meissner, Zeitschrift für Physik **74**, 715 (1932).

[16] A. F. Andreev, Soviet Physics JETP **19**, 1228 (1964).

[17] A. Zaikin, Solid State Communications **41**, 533 (1982).

[18] W. Belzig, C. Bruder, and Yu. V. Nazarov, Journal of Low Temperature Physics **147**, 441 (2007).

[19] W. Belzig, C. Bruder, and G. Schön, Physical Review B **53**, 5727 (1996).

[20] A. C. Mota, P. Visani, and A. Pollini, Journal of Low Temperature Physics **76**, 465 (1989).

[21] Th. Bergmann, K. H. Kuhl, B. Schröder, M. Jutzler, and F. Pobell, Journal of Low Temperature Physics **66**, 209 (1987).

[22] J. C. Cuevas and F. S. Bergeret, Physical Review Letters **99**, 217002 (2007).

[23] D. Roditchev, C. Brun, L. Serrier-Garcia, J. C. Cuevas, V. H. L. Bessa, M. V. Milošević, F. Debontridder, V. Stolyarov, and T. Cren, Nature Physics **11**, 332 (2015).

[24] H. Suderow, I. Guillamón, J. G. Rodrigo, and S. Vieira, Superconductor Science and Technology **27**, 063001 (2014).

[25] P. E. Goa, H. Hauglin, Å. A. F. Olsen, M. Baziljevich, and T. H. Johansen, Review of Scientific Instruments **74**, 141 (2003).

[26] M. Amundsen, J. A. Ouassou, and J. Linder, Physical Review Letters **120**, 207001 (2018).

[27] J. Wang, S. Wang, Y. Zeng, H. Huang, F. Luo, Z. Xu, Q. Tang, G. Lin, C. Zhang, Z. Ren, G. Zhao, D. Zhu, S. Wang, H. Jiang, M. Zhu, C. Deng, P. Hu, C. Li, F. Liu, J. Lian, X. Wang, L. Wang, X. Shen, and X. Dong, Physica C: Superconductivity **378–381**, 809 (2002).

[28] A. Aronov, Soviet Physics JETP **18**, 228 (1973).

[29] A. Aronov and B. Spivak, Soviet Phyics. Solid State **17**, 1874 (1975).

[30] V. Berezinskii, JETP Letters **20**, 287 (1974).

[31] J. Linder and A. V. Balatsky, Reviews of Modern Physics **91**, 045005 (2019).

[32] F. S. Bergeret, A. F. Volkov, and K. B. Efetov, Physical Review B **64**, 134506 (2001).

[33] J. Linder, T. Yokoyama, A. Sudbø, and M. Eschrig, Physical Review Letters **102**, 107008 (2009).

[34] J. Linder, A. Sudbø, T. Yokoyama, R. Grein, and M. Eschrig, Physical Review B **81**, 214504 (2010).

[35] T. Yokoyama, Y. Tanaka, and N. Nagaosa, Physical Review Letters **106**, 246601 (2011).

[36] M. Alidoust, K. Halterman, and J. Linder, Physical Review B **89**, 054508 (2014).

[37] A. Di Bernardo, Z. Salman, X. L. Wang, M. Amado, M. Egilmez, M. G. Flokstra, A. Suter, S. L. Lee, J. H. Zhao, T. Prokscha, E. Morenzoni, M. G. Blamire, J. Linder, and J. W. A. Robinson, Physical Review X **5**, 041021 (2015).

[38] A. A. Golubov, M. Yu. Kupriyanov, and M. M. Khapaev, JETP Letters **104**, 847 (2016).

[39] J. A. Ouassou, W. Belzig, and J. Linder, Physical Review Letters **124**, 047001 (2020).

[40] H. Falch, *Non-Equilibrium Vortices in Superconductor-Normal Metal Structures*, Project thesis, Norwegian University of Science and Technology, Trondheim (2022), project thesis at NTNU.

[41] L. V. Keldysh, Soviet Physics JETP **20**, 1018 (1965).

[42] J. Rammer and H. Smith, Reviews of Modern Physics **58**, 323 (1986).

[43] J. P. Morten, *Spin and Charge Transport in Dirty Superconductors*, Diploma Thesis, Norwegian University of Science and Technology (2003).

[44] W. Belzig, F. K. Wilhelm, C. Bruder, G. Schön, and A. D. Zaikin, Superlattices and Microstructures **25**, 1251 (1999).

[45] J. E. Moyal, Mathematical Proceedings of the Cambridge Philosophical Society **45**, 99 (1949).

[46] V. Chandrasekhar, in *Superconductivity*, edited by K. H. Bennemann and J. B. Ketterson (Springer Berlin Heidelberg, Berlin, Heidelberg, 2008) p. 286.

[47] K. Nagaev, Physics Letters A **169**, 103 (1992).

[48] H. Pothier, S. Guéron, N. O. Birge, D. Esteve, and M. H. Devoret, Physical Review Letters **79**, 3490 (1997).

[49] H. Goldstein, C. P. Poole, and J. Safko, *Classical Mechanics*, 3rd ed. (Addison–Wesley, 2001).

[50] K. Fossheim and A. Sudbø, *Superconductivity*, 1st ed. (Wiley, 2004).

[51] B. Berche and E. Medina, European Journal of Physics **34**, 161 (2013).

[52] L. P. Gor'Kov, Soviet Physics JETP **7**, 505 (1958).

[53] G. Eilenberger, Zeitschrift für Physik A Hadrons and nuclei **214**, 195 (1968).

[54] U. Eckern and A. Schmid, Journal of Low Temperature Physics **45**, 137 (1981).

[55] K. D. Usadel, Physical Review Letters **25**, 507 (1970).

[56] F. S. Bergeret, A. F. Volkov, and K. B. Efetov, Reviews of Modern Physics **77**, 1321 (2005).

[57] Y. V. Nazarov, Superlattices and Microstructures **25**, 1221 (1999).

[58] F. S. Bergeret and J. C. Cuevas, Journal of Low Temperature Physics **153**, 304 (2008).

[59] J. A. Ouassou, J. W. A. Robinson, and J. Linder, Scientific Reports **9**, 12731 (2019).

[60] G. B. Arfken and H. J. Weber, *Mathematical Methods for Physicists*, 6th ed. (Elsevier, Boston, 2005).

[61] M. Y. Kuprianov and V. F. Lukichev, Soviet Physics JETP **67**, 139 (1988).

[62] R. C. Dynes, V. Narayanamurti, and J. P. Garno, Physical Review Letters **41**, 1509 (1978).

[63] J. A. Ouassou, T. D. Vethaak, and J. Linder, Physical Review B **98**, 144509 (2018).

[64] G. Dahlquist and Å. Björck, *Numerical Methods in Scientific Computing* (Society for Industrial and Applied Mathematics, Philadelphia, 2008).

[65] C. Constanda, *Solution Techniques for Elementary Partial Differential Equations, Second Edition*, 2nd ed. (Chapman and Hall, 2010).

[66] P. Virtanen, R. Gommers, T. E. Oliphant, M. Haberland, T. Reddy, D. Cournapeau, E. Burovski, P. Peterson, W. Weckesser, J. Bright, S. J. Van Der Walt, M. Brett, J. Wilson, K. J. Millman, N. Mayorov, A. R. J. Nelson, E. Jones, R. Kern, E. Larson, C. J. Carey, İ. Polat, Y. Feng, E. W. Moore, J. VanderPlas, D. Laxalde, J. Perktold, R. Cimrman, I. Henriksen, E. A. Quintero, C. R. Harris, A. M. Archibald, A. H. Ribeiro, F. Pedregosa, P. Van Mulbregt, SciPy 1.0 Contributors, A. Vijaykumar, A. P. Bardelli, A. Rothberg, A. Hilboll, A. Kloeckner, A. Scopatz, A. Lee, A. Rokem, C. N. Woods, C. Fulton, C. Masson, C. Häggström, C. Fitzgerald, D. A. Nicholson, D. R. Hagen, D. V. Pasechnik, E. Olivetti, E. Martin, E. Wieser, F. Silva, F. Lenders, F. Wilhelm, G. Young, G. A. Price, G.-L. Ingold, G. E. Allen, G. R. Lee, H. Audren, I. Probst, J. P. Dietrich, J. Silterra, J. T. Webber, J. Slavič, J. Nothman, J. Buchner, J. Kulick, J. L. Schönberger, J. V. De Miranda Cardoso, J. Reimer, J. Harrington, J. L. C. Rodríguez, J. Nunez-Iglesias, J. Kuczynski, K. Tritz, M. Thoma, M. Newville, M. Kümmerer, M. Bolingbroke, M. Tartre, M. Pak, N. J. Smith, N. Nowaczyk, N. Shebanov, O. Pavlyk, P. A. Brodtkorb, P. Lee, R. T. McGibbon, R. Feldbauer, S. Lewis, S. Tygier, S. Sievert, S. Vigna, S. Peterson, S. More, T. Pudlik, T. Oshima, T. J. Pingel, T. P. Robitaille, T. Spura, T. R. Jones, T. Cera, T. Leslie, T. Zito, T. Krauss, U. Upadhyay, Y. O. Halchenko, and Y. Vázquez-Baeza, Nature Methods **17**, 261 (2020).

[67] X. S. Li, ACM Transactions on Mathematical Software **31**, 302 (2005).

[68] J. A. Ouassou, *Manipulating Superconductivity in Magnetic Nanostructures in and out of Equilibrium*, Doctoral thesis, NTNU (2019).

[69] J. Jackson, *Classical Electrodynamics*, 3rd ed. (Wiley, 1999).

[70] M. Tinkham, *Introduction to Superconductivity*, 2nd ed. (McGraw-Hill, 1996).

[71] L. F. Chibotaru, A. Ceulemans, V. Bruyndoncx, and V. V. Moshchalkov, Physical Review Letters **86**, 1323 (2001).

[72] G. J. C. Van Baarle, A. M. Troianovski, T. Nishizaki, P. H. Kes, and J. Aarts, Applied Physics Letters **82**, 1081 (2003).

[73] V. S. Stolyarov, T. Cren, C. Brun, I. A. Golovchanskiy, O. V. Skryabina, D. I. Kasatonov, M. M. Khapaev, M. Y. Kupriyanov, A. A. Golubov, and D. Roditchev, Nature Communications **9**, 2277 (2018).

[74] M. Spivak, *Calculus on Manifolds: A Modern Approach to Classical Theorems of Advanced Calculus*, Mathematics Monograph Series (CRC Press, Taylor & Francis Group, Boca Raton London New York, 2018).

[75] J.-B. Campesato, "Poincaré lemma: Potentials and vector potentials," (2020), lecture notes.

[76] D. K. Finnemore, T. F. Stromberg, and C. A. Swenson, Physical Review **149**, 231 (1966).

[77] D. B. Liarte, S. Posen, M. K. Transtrum, G. Catelani, M. Liepe, and J. P. Sethna, Superconductor Science and Technology **30**, 033002 (2017).

[78] T. McConville and B. Serin, Physical Review **140**, A1169 (1965).

[79] Y. Wang, T. Plackowski, and A. Junod, Physica C: Superconductivity **355**, 179 (2001).

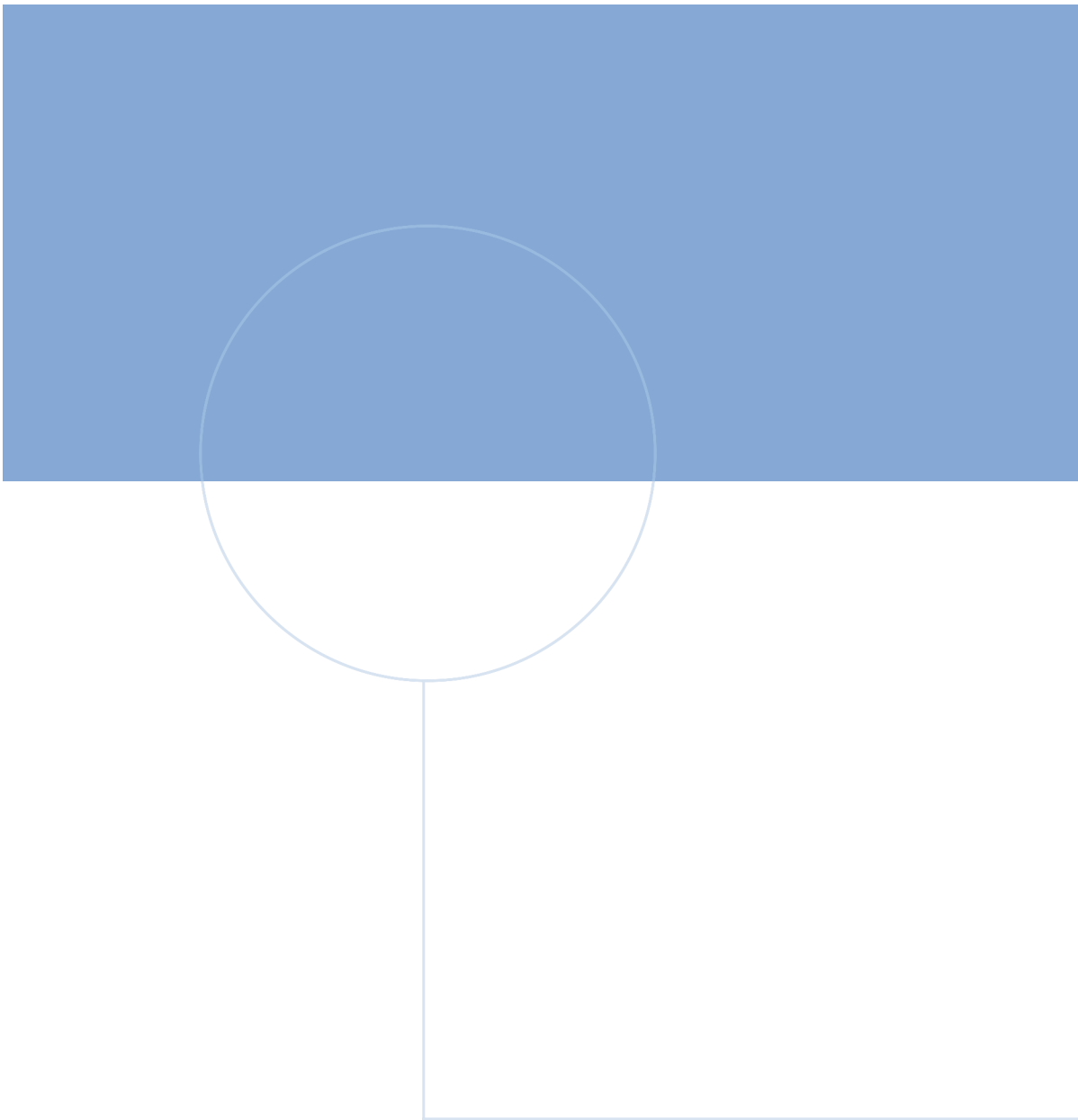

NTNU

Norwegian University of
Science and Technology